

Important Notice

This copy may be used only for the purposes of research and private study, and any use of the copy for a purpose other than research or private study may require the authorization of the copyright owner of the work in question. Responsibility regarding questions of copyright that may arise in the use of this copy is assumed by the recipient.

UNIVERSITY OF CALGARY

Applications of V_p/V_s and AVO modeling
for monitoring heavy oil cold production

by

Duojun (Albert) Zhang

A THESIS

SUBMITTED TO THE FACULTY OF GRADUATE STUDIES
IN PARTIAL FULFILLMENT OF THE REQUIREMENTS FOR
THE DEGREE OF MASTER OF SCIENCE

DEPARTMENT OF GEOLOGY AND GEOPHYSICS

CALGARY, ALBERTA

JULY, 2007

© Duojun (Albert) Zhang 2007

UNIVERSITY OF CALGARY
FACULTY OF GRADUATE STUDIES

The undersigned certify that they have read, and recommended to the Faculty of Graduate Studies for acceptance, a thesis entitled “Applications of V_P/V_S and AVO modeling for monitoring heavy oil cold production” submitted by Duojun (Albert) Zhang in partial fulfillment of the requirements for the degree of Master of Science.

Supervisor, Dr. Larry R. Lines
Department of Geology and Geophysics

Dr. John Bancroft
Department of Geology and Geophysics

Dr. Brij Maini
Department of Chemical and Petroleum Engineering

Date

ABSTRACT

Simultaneous extraction of oil and sand during the heavy oil cold production generates high porosity channels termed “wormholes”. The development of wormholes causes reservoir pressure to fall below the bubble point, resulting in dissolved-gas coming out of solution to form foamy oil. Both foamy oil and wormholes are believed to be two key factors in the enhancement of cold heavy oil production. In enhanced oil recovery, it is important to map cold production reservoir changes due to wormholes and foamy oil. It is the purpose of this thesis to use seismic monitoring methods to map cold production footprints.

The presence of small amounts of gas trapped in the foamy oil can dramatically decrease the fluid bulk modulus, reducing the P-wave velocity of saturated sands, while slightly increasing the S-wave velocity. The V_p/V_s ratio and Poisson’s ratio have a subsequent reduction.

The viscosity of heavy oil is primarily a function of oil gravity and temperature. Increasing the temperature will decrease sample’s viscosity, causing both bulk and shear moduli to decrease approximately linearly with increasing temperature. Moreover, the frequency also plays an important role for seismic waves in heavy oil. For heavy oil in the 10-20 API range at ambient temperature of 20 °C, the shear modulus is negligible and heavy oil still acts like a liquid at seismic frequencies, especially after cold

production. Gassmann's equation can still help us understand the seismic response of heavy oil reservoirs for pre- and post- cold production.

The V_p/V_s ratio is a function of both fluid bulk modulus and porosity. For unconsolidated sands with high porosity, pore fluids have a significant influence on final V_p/V_s ratio. Due to the dramatic reduction of fluid's bulk modulus after heavy oil cold production, the V_p/V_s ratio will have a detectable reduction, even though the increasing porosity from wormholes slightly increases the V_p/V_s ratio. For unconsolidated sands, the lower pore pressure and increasing differential pressure will also tend to decrease the final V_p/V_s ratio.

Interpreting multicomponent seismic data to get V_p/V_s ratio maps from traveltime measurements on vertical and radial component data is straightforward. Error analysis and practical mapping tell us that the calculated V_p/V_s ratio will not be overly sensitive to the choice of picking surrounding formations. Traveltime interval mapping of V_p/V_s ratio provides a robust method for us to monitor the reduction of V_p/V_s ratio due to heavy oil cold production. Although traveltime picking is relatively insensitive to spectral differences between components, bandpass filtering can provide some improvement to the quality of final V_p/V_s ratio map, by enhancing the similarity between PP and PS seismic volumes.

The difference of Poisson's ratio between pre- and post-production will create different AVO responses. The calculated result from fluid substitution reveals that there

is about 10% reduction of P-wave velocity, about 30% reduction of saturated bulk modulus and about 20% reduction of Poisson's ratio due to heavy oil cold production. Further calculations indicate that there is about 20% reduction of the V_p/V_s ratio after heavy oil cold production. Meanwhile, there is no detectable difference between the pre-production and the wet case. Hence, we cannot readily use V_p/V_s ratio and AVO analysis to differentiate heavy oil and brine saturated sands.

Synthetic seismograms from the results of fluid substitution reveal that all the AVO responses for pre- and post-production and the wet case belong to Class IV AVO anomalies, as described by Castagna et al. (1998). The AVO response for post-production is separated from the other two cases. Although using the product of intercept and gradient is difficult to discriminate Class IV AVO responses, the fluid factor is useful to interpret Class IV AVO response. Because V_p/V_s ratios vary with time, a calibrated time varying gain function $g(t)$ will give a better estimate of the fluid factor for the target zone.

For the in-situ well, four methods to do fluid substitution are performed, one of them using available S-wave sonic log data, others not using available S-wave sonic log data. The Greenberg-Castagna calculation gives the closest calculated S-wave log data to the actual S-wave log data with using available original S-wave log data. Assuming Castagna's equation is correct for the wet case, the calculations give a relatively small S-wave velocity, while assuming dry rock Poisson's ratio, the calculations give a relatively high S-wave velocity. But overall, all of the methods give the similar AVO response from

the top of the target zone, which are Class IV AVO responses, and the AVO responses for post-production are separated from other two cases.

ACKNOWLEDGEMENTS

I would like to express my sincere thanks to Dr. Larry Lines, my thesis supervisor, for his guidance and many valuable suggestions. His vast knowledge and keen intuitive understanding of geophysics helped me throughout my graduate studies. Moreover, Larry gave me strong support and encouragement during my study and research, and helped me overcome many difficulties to pursue my MSc. degree at the Department of Geology and Geophysics.

The CREWES environment provided a friendly atmosphere to learn about a wide range of topics in geophysics and present ideas. From this group, I made a number of good friendships and learned a lot from the discussion with them. I would also like to thank a number of professors that I learned so much from: Ed Krebes from whom I learned a great deal about seismology and the derivation of mathematical equations, Gary Margrave from whom I learned much about the vivid understanding of mathematical geophysics and found the fun in this field, and John Bancroft from whom I got a practical understanding of pre- and post-stack migration.

From early of 2006, I started to work for Veritas, and got a better understanding of rock physics through the technical discussion with several colleagues like Dave Gray and Jon Downton. These discussions provided me with valuable ideas to solve the theoretical problems during my research.

In the past three years, I also got much help from my good friends, like Chuck Wardrop, Richard Xu, Jianhua Pon, Lanlan Yan, and Paul Thacker. They helped me get involved in Canadian life and the pursuit of my career in North America.

I give special thanks to Joan Embleton, Kevin Hall, Rolf Maier, Paul Bessette, Brian Mills and Bruce Palmiere for their support and technical discussions. I am also very grateful to the sponsors to the CREWES and CHORUS projects.

TABLE OF CONTENTS

APPROVAL PAGE	ii
ABSTRACT	iii
ACKNOWLEDGEMENTS	vii
TABLE OF CONTENTS	ix
LIST OF FIGURES	xi
LIST OF TABLES	xvi
CHAPTER 1: INTRODUCTION OF HEAVY OIL COLD PRODUCTION.....	1
1.1 Introduction	1
1.2 Reservoir conditions and production rates	2
1.3 Cold production mechanisms	4
1.4 Disturbance of fluid properties	7
CHAPTER 2: REVIEW OF PREVIOUS SEISMIC MONITORING RESEARCH IN HEAVY OIL COLD PRODUCTION	9
2.1 Introduction	9
2.2 Seismic pursuit of wormholes	9
2.3 Time-lapse seismology to determine foamy oil and wormhole footprints	12
2.4 Time-lapse seismic analysis of a heavy oil cold production field	15
CHAPTER 3: SEISMIC ROCK PHYSICS FOR HEAVY OIL	19
3.1 Fluid substitution: the Gassmann's Equation	19
3.2 Rock physics for heavy oil	22
3.3 An in-situ example of heavy oil	26
CHAPTER 4: EFFECTS OF HEAVY OIL COLD PRODUCTION ON RESERVOIR PROPERTIES	33

4.1	Difference of heavy oil physical properties between pre- and post-production	33
4.2	Effects of heavy oil cold production on V_p/V_s ratio	35
4.3	Effect of pressure on V_p/V_s ratio	45
CHAPTER 5: THE ROBUSTNESS OF V_p/V_s MAPPING		48
5.1	Introduction	48
5.2	Interpretation of seismic data	52
5.3	Spectral differences between PP and PS seismic data	55
5.4	Error analysis	63
CHAPTER 6: THE FEASIBILITY OF AVO ANALYSIS FOR MONITORING HEAVY OIL COLD PRODUCTION		70
6.1	Effect of the V_p/V_s ratio on the AVO response	70
6.2	Fluid substitution for heavy oil cold production using S-wave sonic log data.....	73
6.3	Fluid substitution without S-wave sonic log data	80
6.3.1	Castagna's equation for fluid saturated rocks	80
6.3.2	Estimating dry rock Poisson's ratio	82
6.3.3	The Greenberg-Castagna calculation.....	84
6.4	Fluid substitution for a real well	86
CHAPTER 7: CONCLUSIONS AND FUTURE WORK		105
REFERENCES.....		110

LIST OF FIGURES

Figure 1.1 Heavy oil deposits in Alberta and Saskatchewan, with an indication of the cold production belt (Sawatzky et al., 2002)	2
Figure 1.2 A schematic of a cold production oil pump (courtesy of Kudu Oil Well Pumps)	3
Figure 1.3 Foamy oil (D. Greenidge, ESSO, private communication)	4
Figure 1.4 CT scanned longitudinal sections of the sandpack with wormhole growth. Top image: before pressure depletion; middle image: 20 days after start of pressure depletion; bottom image: 47 days after start of pressure depletion (Tremblay et al., 1999a)	5
Figure 1.5 A schematic of a wormhole model as shown by Miller et al. (1999)	6
Figure 1.6 Schematic phase behavior for hydrocarbon mixtures showing the relative position of heavy oils (Batzle et al., 2006)	8
Figure 1.7 Heavy oil bulk modulus (mixture) as a function of pressure (Batzle et al., 2006)	8
Figure 2.1 Synthetic seismogram for the given model with the peak frequency of 185Hz (Lines et al., 2003)	10
Figure 2.2 Synthetic seismogram for the given model with the peak frequency of 3000Hz (Lines et al., 2003)	11
Figure 2.3 Map of seismic amplitude from Mayo (1996)	12
Figure 2.4 P-wave and S-wave velocities versus porosity using Murphy's empirical relations (Chen, 2004)	13
Figure 2.5 Seismic response of pre-production model to research the effect of foamy oil (Chen, 2004)	14
Figure 2.6 Seismic response of post-production model to research the effect of foamy oil (Chen, 2004)	14
Figure 2.7 PP seismic response of post-production model to research the effect of wormholes (Chen, 2004)	15

Figure 2.8 PS seismic response of post-production model to research the effect of wormholes (Chen, 2004)	15
Figure 2.9 Amplitude map for McLaren event from 1987 survey (Zou et al., 2004)	16
Figure 2.10 Amplitude map for McLaren event from 1996 survey (Zou et al., 2004) ...	17
Figure 2.11 Time difference map of the 1996 isochron and the 1987 isochron (Zou et al., 2004). In the grid, each square is 100m x 100m.....	18
Figure 3.1 Ultrasonic shear waveforms in very heavy oil at -12°C and 49°C (Batzle et al., 2006)	22
Figure 3.2 Elastic moduli of the heavy oil from ultrasonic data. The effective shear modulus (triangles) drops toward zero as temperatures approach 80°C (Batzle et al., 2006)	23
Figure 3.3 Measured (triangles) and calculated (lines) shear modulus in Uvalde heavy oil (API=-5) using a viscoelastic liquid (Cole-Cole) model (Batzle et al., 2006)	24
Figure 4.1 The contribution from the fluid is much higher in unconsolidated sands than in consolidated sands (Hilterman, 2001)	37
Figure 4.2 The effect of K_f on V_p/V_s ratio	41
Figure 4.3 The velocity ratio $R=V_p/V_s$, plotted versus porosity as a function of pore fluid saturation for gas, oil, and water in clean quartz sandstones. The marks are laboratory measurements. The lines are the Gassmann predictions (Murphy et al., 1993)	41
Figure 4.4 The effect of porosity on V_p/V_s ratio	42
Figure 4.5 Theoretical V_p/V_s ratio of sand suspended in coal tar pitch at 0°C (Hornby et al., 1987)	43
Figure 4.6 Influence of effective pressure P_e , porosity ϕ , and clay content C on V_p/V_s ratios indicated by the number next to lines (Eberhart-Phillips et al., 1989)	44
Figure 4.7 V_p/V_s ratios for all the Gassmann fluid-substituted glass bead data are plotted against pressure and color-coded by porosity. (a) Linear scale pressure-axis. (b) Log scale pressure-axis (Zimmer et al., 2002)	45

Figure 4.8 Relationship between V_p / V_s ratio and differential pressure for the data collected in Prasad's study (Prasad, 2002)	47
Figure 5.1 Robustness of traveltimes picks for zero-phase wavelets with different spectral content. Traces 1-10 contains Ricker wavelets with peak frequencies of 40 Hz, and traces 11-20 contains Ricker wavelets with peak frequencies of 20 Hz. On both sets of traces, traveltimes picks of the peaks produce isochron values of 50 ms, despite the difference in wavelet spectra (Time scale is in samples, where 1 sample = 1 ms) (Zhang and Lines, 2006)	50
Figure 5.2 The basemap of project	53
Figure 5.3 Synthetic seismogram for PP data	54
Figure 5.4 Synthetic seismogram for PS data	55
Figure 5.5 Selected reference top and bottom horizons	55
Figure 5.6 Amplitude spectra of wavelets extracted from PP (left) and PS (right) seismic data at Plover Lake field	56
Figure 5.7 Comparison between unfiltered PP (left) and filtered PP (right) seismic data (Line on left is plots traces 116-1 and line on the right plots traces 1-116)	57
Figure 5.8 Comparison between unfiltered PP (left) and PS (right) seismic data. The frequency content of the PP section is much higher than the corresponding PS section	57
Figure 5.9 Comparison between filtered PP (left) and PS (right) seismic data shows a better correlation of reflecting events than in Figure 5.8	58
Figure 5.10 Difference of top horizons between unfiltered and filtered PP seismic data	58
Figure 5.11 V_p/V_s between top and bottom horizons from unfiltered PP and PS data ...	59
Figure 5.12 V_p/V_s between top and bottom horizons from filtered PP and PS data	60
Figure 5.13 Isochron map between top and bottom horizons from filtered PP data	62
Figure 5.14 Isochron map between top and bottom horizons from PS data	62
Figure 5.15 Comparing result from Figures 5.13 and 5.14. The lateral variations of P-wave and S-wave traveltimes are denoted	63

Figure 5.16 The sketch of interpreted model	64
Figure 5.17 Calculated velocities ratio (V_p^*/V_s^*) versus real velocities ratio (V_p/V_s)	68
Figure 5.18 The impedance inversion result from PP seismic volume	69
Figure 6.1 The dependence of Poisson's ratio σ on V_p/V_s ratio	71
Figure 6.2 P-wave reflection coefficients before production	72
Figure 6.3 Comparison of P-wave reflection coefficients between pre- and post-production	73
Figure 6.4 Well logs for pre-production (blue) and wet case (red) within analysis zone	88
Figure 6.5 Well logs for wet case (blue) and post-production (red) within analysis zone	89
Figure 6.6 Synthetic seismograms for wet case, pre- and post-production conditions ...	89
Figure 6.7 Created zero phase Ricker wavelet with 70 Hz dominant frequency	90
Figure 6.8 Picked events from the top of the reservoir in three synthetic seismograms..	90
Figure 6.9 AVO intercept (A) versus gradient (B) crossplot showing four possible quadrants (Castagna et al., 1998)	91
Figure 6.10 Plane-wave reflection coefficients at the top of each augmented Rutherford and Williams' classification of sands (Castagna et al., 1998)	92
Figure 6.11 Diagrammatic crossplot of P-wave velocity against S-wave velocity (Castagna et al., 1985)	96
Figure 6.12 Calculated V_p/V_s ratio log from the in-situ well	98
Figure 6.13 Crossplot of V_p against V_s for the whole well depth from the in-situ well...	98
Figure 6.14 Crossplot of V_p against V_s for the target zone from the in-situ well	99
Figure 6.15 Synthetic seismograms for wet condition, pre- and post-production conditions are concatenated into one volume with replicating each of the input volumes 5 times prior to concatenation	100
Figure 6.16 Fluid factors for the three separate conditions with $g(t)=0.75$	101
Figure 6.17 Fluid factors for the three separate conditions with default $g(t)$	101

Figure 6.18 All three V_p/V_s ratios for pre-production, wet and post-production conditions after fluid substitution and the difference of V_p/V_s ratios between post- and pre-production conditions	102
Figure 6.19 Calculated well logs from fluid substitutions for pre-production without using original S-wave log data	103
Figure 6.20 Calculated well logs from fluid substitutions for post-production without using original S-wave log data	104
Figure 6.21 Picked events from the top of the reservoir in synthetic seismograms based on calculated well logs from fluid substitutions without using original S-wave log data	104

LIST OF TABLES

Table 2.1 Rock properties of drainage sands with the presence of foamy oil. As reservoir pressure decreases from 3 MPa to 1.5 MPa, S_o changes from 80% to 70%, and S_g from 0 to 10% (Chen, 2004)	13
Table 3.1 Reservoir parameters for the in-situ well	27
Table 3.2 Estimated average values of production zone for V_p , V_s , and ρ^*	27
Table 3.3 Fluid properties for pre-production condition	28
Table 3.4 Mineral moduli for shaly sands (Han et al., 2004)	29
Table 3.5 Calculated saturated moduli from well log data, Gassmann's equation, and scattering theory	32
Table 4.1 A typical comparison of reservoir parameters between pre- and post- cold production in Plover Lake oil field	34
Table 4.2 Calculated physical properties of reservoir fluids for pre- and post- cold production	34
Table 5.1 The result of error analysis	67
Table 6.1 Estimated physical properties from well log data	72
Table 6.2 Reservoir parameters and fluid properties for pre- and post-production conditions	87
Table 6.3 Top sand reflection coefficient versus offset behavior for the four augmented Rutherford and Williams' Classes I-IV, assuming a typical "background" trend with negative slope (Castagna et al., 1998)	92
Table 6.4 Well log velocities and densities for an East African gas sand and overlying strata (Castagna et al., 1998)	93
Table 6.5 Well log velocities and densities for the in-situ case	94

CHAPTER 1

INTRODUCTION OF HEAVY OIL COLD PRODUCTION

1.1 Introduction

Heavy oils are defined as having high densities and extremely high viscosities. Density is usually described by API, which is defined as: $API = (141.5 / \text{specific gravity}) - 131.5$, where the specific gravity is the ratio of the density of the oil and the density of water. Heavy oils usually refer to oils with API gravities below 20, and with very heavy oils having an API less than 10 (density greater than 1g/cc). Heavy oils are an abundant resource, particularly in Canada, Venezuela, and Alaska. By some estimates, heavy oils represent as much as 6.3 trillion barrels of oil in place. This matches available quantities of conventional oil. More than 50% of Canada's oil production is now from heavy oil (Batzle et al. 2006).

Much of the heavy oil recovery in Western Canada involves steam injection, called 'hot production'. In this process, steam is injected into the reservoir, increasing the temperature of the reservoir and reducing the viscosity of the heavy oil, thus making flow easier and boosting the oil recovery. An alternative to thermal heavy oil production in the field is known as 'cold production', which is a primary non-thermal process in which reservoir temperature is not affected. During the cold production process, sand and oil are produced simultaneously to enhance oil recovery. The cold production process has been economically successful in several unconsolidated heavy oil fields in Alberta and Saskatchewan, Canada (Figure 1.1). This process has been due mainly to the development and widespread use of progressive cavity pumps (Figure 1.2). These pumps

can generate high pressure to lift the unconsolidated sands to the surface. Unlike hot production, cold production has minimal energy requirements and has modest recovery rates. Cold production accounts for the production of 200,000 barrels per day in Western Canada, and has also been applied in Venezuela and China.



Figure 1.1: Heavy oil deposits in Alberta and Saskatchewan, with an indication of the cold production belt (Sawatzky et al., 2002).

1.2 Reservoir conditions and production rates

Most of the cold production reservoirs are thin with thicknesses ranging from 3m to 7m. It is not efficient to exploit these reservoirs using steam injection. To proceed with cold heavy oil production, the oil should have enough dissolved gas with a GOR (Gas Oil Ratio) greater than 5, and sands are poorly consolidated with high porosities and composed mostly of quartz. The average diameter of the sands produced by cold production is between 0.1mm and 0.25mm. Most producing formations in Western

Canada belong to the Lower Cretaceous Mannville Groups, having common depths from 400m to 800m. The reservoir temperature is of the order of 20 degrees Celsius, and the initial reservoir pressure is on the order of 3-5MPa.

With sand production, the cold production process improves oil production rates substantially compared to the primary production rates when sand is not produced. Producing sand improves oil production rate by an order of magnitude compared with the average production rate of non-sand production.



Figure 1.2: A schematic of a cold production oil pump (courtesy of Kudu Oil Well Pumps).

Most of the sand is extracted during the first six or twelve months of production, where the sand cuts can be high, varying from 10% to 40% of the total volume of the fluids and sand slurry. After this initial production, the sand cuts tend to be low and stable, less than 5%, at which time oil production dominates (Tremblay, et al. 1999a). In general,

the initial rate of sand production increases with increasing oil viscosity and permeability. The cumulative sand production is proportional to the cumulative oil production.

1.3 Cold production mechanisms

Significant increases in oil recovery with increasing rates of pressure depletion have been observed in most fields. When the reservoir pressure drops below bubble point, dissolved gas in live heavy oil comes out of solution as bubbles. The gas evolves slowly, but continuous phase coalescence is impeded by capillary effects and high viscosity. Thus, the trapped gas bubbles within the heavy oil form the foamy oil, which is a foamy or emulsive state (Figure 1.3). Unlike normal two-phase flow that requires a fluid phase to become continuous before it becomes mobile, foamy oil flow involves the flow of dispersed gas bubbles. It is believed that such dispersed flow of gas is responsible for unexpectedly high recovery factors often seen in cold production projects (Maini, 2004), the foamy oil contributes significantly to the pressure support in the reservoir. Foamy oil generation resulting from the initial reservoir pressure reduction provides the necessary support mechanism to sustain the observed high oil recovery (Metwally, et al. 1995).



Figure 1.3: Foamy oil (D. Greenidge, ESSO, private communication).

Sand production leads to the creation of a high-porosity disturbed zone supplying a slurry of sand and fluid to the wellbore. Also tracer tests in the field have indicated that there are some open channels with unknown geometry, termed ‘wormholes’, developing in the reservoir. Several physical lab simulations and numerical simulations have been conducted to induce the development of wormholes. Tremblay, et al. (1999b) monitored a wormhole using solution-gas drive in a sand pack with a length of 85cm, a width of 10cm, and 32% porosity. Figure 1.4 shows the wormhole growth with pressure depletion, corresponding to the initial state and, 20 and 47 days after the start of pressure reduction, respectively, from above to bottom. Here, the porosity of wormholes could be greater than 40%, and the zone of highest porosity is close to the wellbores. Tremblay also hypothesized that wormhole diameters could range from the order of 10 cm to one meter as the maximum size in the field.

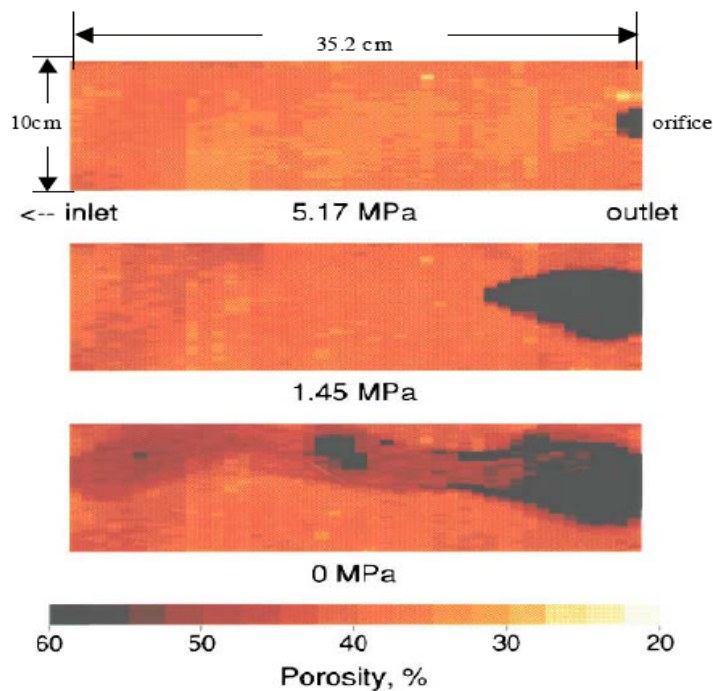


Figure 1.4: CT scanned longitudinal sections of the sandpack with wormhole growth. Top image: before pressure depletion; middle image: 20 days after start of pressure depletion; bottom image: 47 days after start of pressure depletion (Tremblay et al., 1999a).

Both tracer test and lab simulations show that wormholes likely grow within a certain layer in net pay zones. Sawatzky et al. (2002) believe that wormholes grow in unconsolidated, clean sand layers within the net pay zone, along the highest pressure gradient between the borehole and the tip of the wormhole. The radius of wormhole zones can be greater than 100m based on the numerical simulation results in Yuan et al. (1999), who obtained results by matching the production history of the field. Also, the results fit some field observations. Yuan et al. also predicted that wormhole diameter is a function of distance from the wellbore, decreasing in diameter away from the boreholes.

In reality, wormholes could grow anywhere within the pay zone. Yuan extended the probabilistic active walker model, which describes the concept of the random walk model, to simplify the wormhole zone as a thin ‘pancake’ layer, where wormholes grow randomly in a radial pattern. Miller (1999) also illustrated a similar wormhole network pattern, like the root system in Figure 1.5. Therefore, a wormhole network could create an interconnection between wellbores and reservoirs, providing low resistance drainage paths like fractures, and supplying most of the produced fluids. Only a small fraction of the total production comes from outside this region (Metwally, 1995).

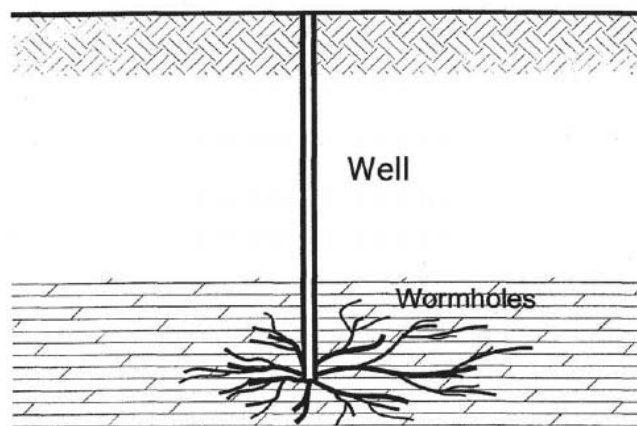


Figure 1.5: A schematic of a wormhole model as shown by Miller et al. (1999).

1.4 Disturbance of fluid properties

The development of wormholes and the formation of foamy oil will absolutely disturb fluid properties in the reservoir during heavy oil cold production. This disturbance will probably be able to be detected from seismic survey, because even very small amounts of gas can have an enormous effect on seismic data.

Figure 1.6 is a schematic phase behavior for hydrocarbon mixtures showing the relative position of heavy oil (Batzle, et al. 2006). Heavy oil can cross the bubble point line in two directions, changing from a one phase region to a two phase region. One direction is indicated by the horizontal dashed red line when the temperature of the reservoir is increased, which is the case of thermal production. Another direction is vertical dashed blue line when pore pressure of reservoir decreases, which is the case of cold production. What will the fluid properties be when heavy oil crosses the bubble point line? Figure 1.7 is the calculated fluid bulk modulus for a heavy oil of API=7 as a function of pressure (Batzle, et al. 2006). Even with a low gas-oil ratio (GOR) of 2, heavy oil crosses the bubble point at about 2 MPa. Above the bubble point, the bulk modulus of the homogeneous mixture is very high: 2.6-2.8 GPa. However, after crossing the bubble point line, gas comes out of solution, and the bulk modulus drops to near zero very quickly. Hence, the seismic properties will be strongly dependent on the reservoir conditions and the production history.

The dramatic reduction of fluid bulk modulus will decrease the traveling compressional wave velocity, and the response of seismic survey will be disturbed subsequently. Among many seismic properties which can be analyzed from seismic survey, I will research how cold heavy oil production affects the V_p/V_s ratio and AVO response, in order to reveal the feasibility of using V_p/V_s ratios and AVO analysis to

monitor the recovery process of cold heavy oil production, where AVO is referred to the amplitude of a reflected P-wave as a function of offset.

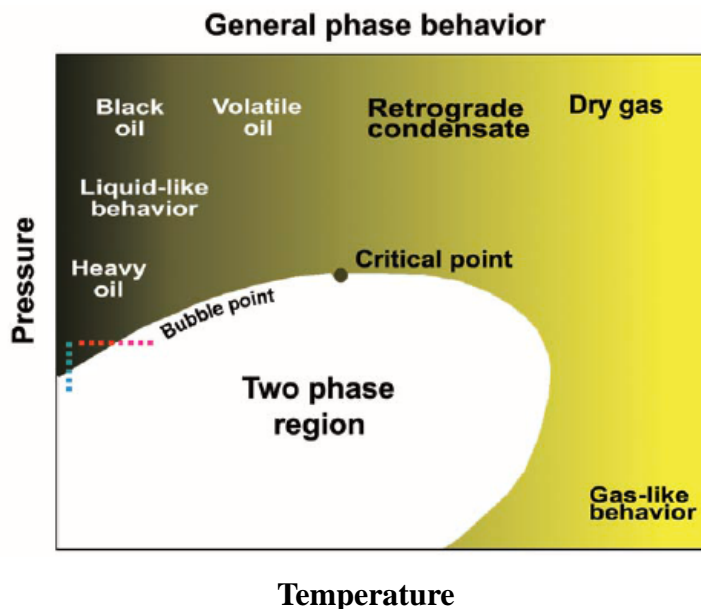


Figure 1.6: Schematic phase behavior for hydrocarbon mixtures showing the relative position of heavy oils (Batzle et al., 2006).

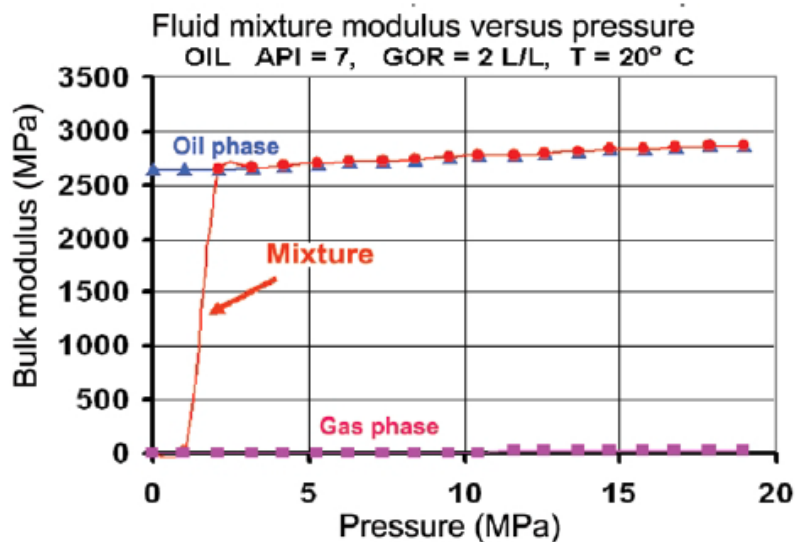


Figure 1.7: Heavy oil bulk modulus (mixture) as a function of pressure (Batzle et al., 2006).

CHAPTER 2

REVIEW OF PREVIOUS SEISMIC MONITORING RESEARCH IN HEAVY OIL COLD PRODUCTION

2.1 Introduction

Simultaneous extraction of oil and sand during the heavy oil cold production creates a wormhole network and a foamy oil drive, while disturbing the initial reservoir state. A key question is the following. What kind of roles can seismology play for mapping the disturbance of the initial reservoir state? Lines et al. (2003) revealed the possibility of detecting wormhole presence instead of imaging individual wormholes by the normal seismic method. Chen et al. (2004) calculated elastic parameters of heavy oil reservoir before and after cold production based on Gassmann's equation, and discussed the use of time-lapse reflection seismology theoretically for detecting the presence of foamy oil and wormholes. Zou et al. (2004) analyzed a repeated 3D seismic survey over a cold production field in eastern Alberta, showed an interesting correlation between time-lapse seismic changes and heavy oil cold production. All of the above research is encouraging, since it confirms that seismology can play an important role in mapping the disturbance of initial reservoir state due to heavy oil cold production.

2.2 Seismic pursuit of wormholes

Due to the development of high-porosity tubes termed "wormholes", the recovery of heavy oil is boosted, operators who plan infill drilling rely on wormhole distribution information to optimize well spacing. To map these induced sand channels, Lines et al. (2003) performed feasibility tests based on a number of models from the literature.

Wormhole patterns have a fractal-like nature similar to root systems or tree branches (Figure 1.5), with about 10cm diameters, although Tremblay et al (1999) suggests that they could be as large as 1 meter. These dimensions are far less than seismic wavelengths, making seismic resolution of individual wormholes extremely difficult. For the given wormhole model, Lines et al. (2003) generated the exploding reflector seismogram in Figure 2.1, which was computed for a seismic wavelet with a peak frequency of 185Hz and the image is quite blurred, demonstrating that seismic detection of individual wormholes is not feasible, even though individual wormholes can be detected with extremely high frequency of 3000Hz (Figure 2.2).

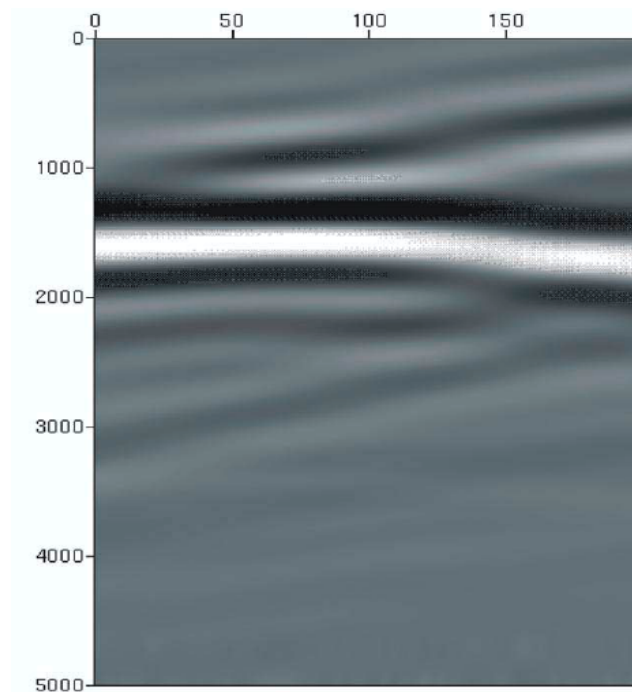


Figure 2.1: Synthetic seismogram for the given wormholes' model with the peak frequency of 185 Hz (Lines et al., 2003).

On the other hand, wormholes can create connectivity within the reservoir and can extend for 100-250 m. If enough wormholes exist, the porosity of the producing oil sands should affect the seismic response. Furthermore, foamy oil, which has a texture not

unlike shaving cream, is caused by depressurization of gas saturated heavy oil. This depressurization increases the total fluid volume, forcing gas and oil into borehole. The presence of small amounts of gas can dramatically decrease the fluid bulk modulus and should also affect the seismic response. So instead of imaging individual wormholes, if we examine the seismic response before and after (during) the production of oil sands, then merely differencing the seismograms may illuminate wormhole development due to the increased porosity, the creation of foamy oil, or both of them. The case history presented by Mayo (1996) indicates that wormholes may create a seismic effect. Attention was focused on this possibility when it was noticed that seismic amplitude anomalies were created around cold production wells (Figure 2.3). The seismic anomalies may have been caused by the production process, possibly due to the existence of wormholes.

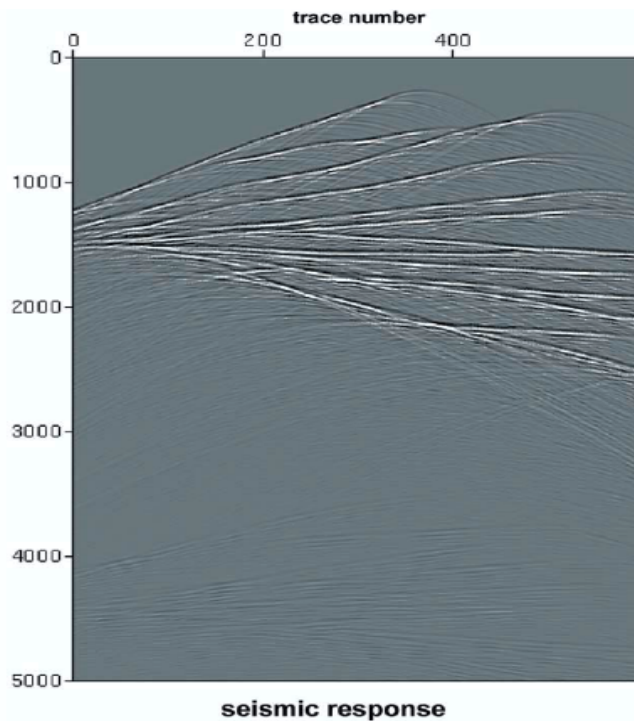


Figure 2.2: Synthetic seismogram for the given wormholes' model with the peak frequency of 3000 Hz (Lines et al., 2003).

In summary, modeling studies demonstrate that seismic detection of individual wormholes is not feasible. However, the presence of many high-porosity wormholes coupled with foamy oil could alter medium properties sufficiently to manifest a seismic response. The important issue is that wormholes will increase the porosity, cause the release of foamy oil, and thereby decrease the seismic velocity. Therefore, time-lapse seismic monitoring methods may also apply to heavy oil cold flow production.

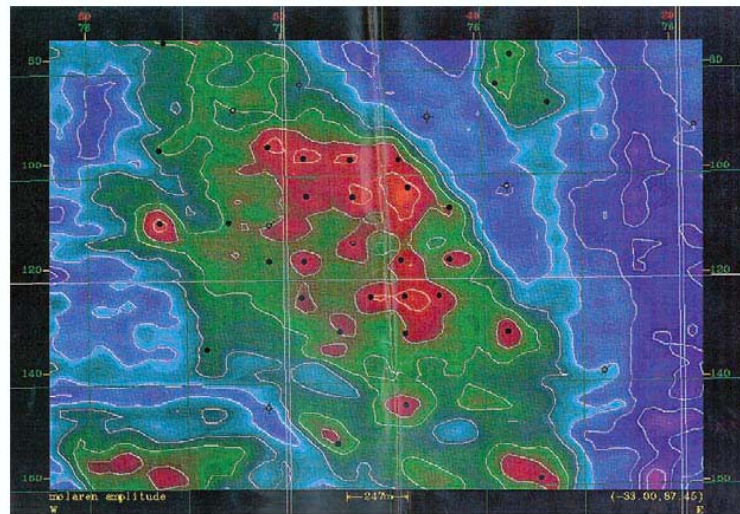


Figure 2.3: Map of seismic amplitude from Mayo (1996).

2.3 Time-lapse seismology to determine foamy oil and wormhole footprints

Commencement of cold production disturbs the initial reservoir state through the presence of foamy oil and wormholes, modifying the fluid phase and elastic properties within drainage areas (Table 2.1, Chen 2004). For the porosity increase from wormholes, the empirical relations between moduli and porosity of pure sands (Murphy et al., 1993) have been used by Chen to calculate elastic moduli of wormhole sands, and Gassmann's equation is applied to obtain both P-wave and S-wave velocities. Figure 2.4 shows that both V_p and V_s decrease with increasing porosity. V_s tends to be zero when the porosity is greater than the critical porosity, because the sand grains become fluid supported.

Table 2.1: Rock properties of drainage sands with the presence of foamy oil. As reservoir pressure decreases from 3 MPa to 1.5 MPa, S_o changes from 80% to 70%, and S_g from 0 to 10% (Chen, 2004).

physical properties of	pre-production	post-production		
driantage zones with foamy oil effects	$S_g=0, S_o=0.8$	$S_g=0.1, S_o=0.7$		
		Reuss	Voigt	Average
saturated rock bulk modulus (Gpa)	10.616	5.2252	10.113	7.807
saturated shear modulus (Gpa)	4.6726	4.6777	4.6777	4.676
saturated bulk density (kg/m^3)	2156.5	2126.6	2126.6	2126
V_p (m/s)	2795	2325	2773	2570
V_s (m/s)	1472	1483	1483	1483

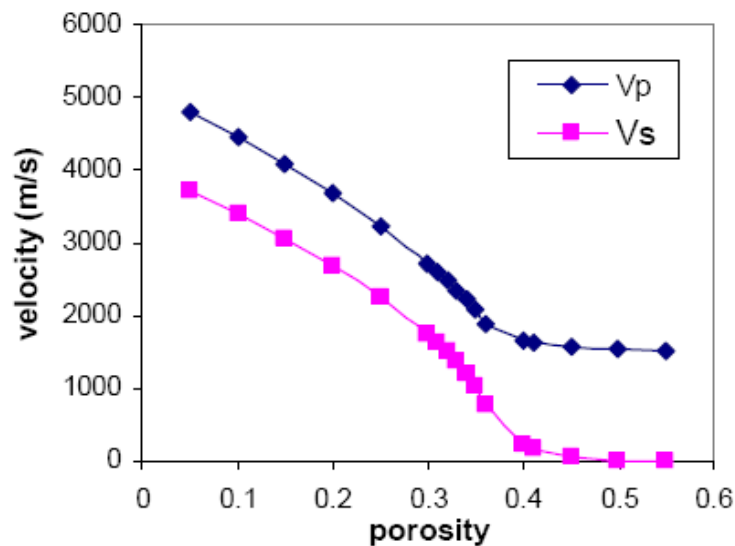


Figure 2.4: P-wave and S-wave velocities versus porosity using Murphy's empirical relations (Chen, 2004).

Figures 2.5 and 2.6 respectively show the depth migrated sections from the pre- and post-production models with a 200 Hz frequency bandwidth. The amplitude anomalies and travel time delays caused by the low velocity drainage zones filled with gas bubbles are evident. The stacked PP and PS seismic sections were generated for the creation of wormholes and shown in Figures 2.7 and 2.8. Because of the greater contrast in V_s , the

amplitude anomalies and travel time delay on the PS section are more readily seen than on PP section, where only subtle changes can be detected around area with high wormhole densities.

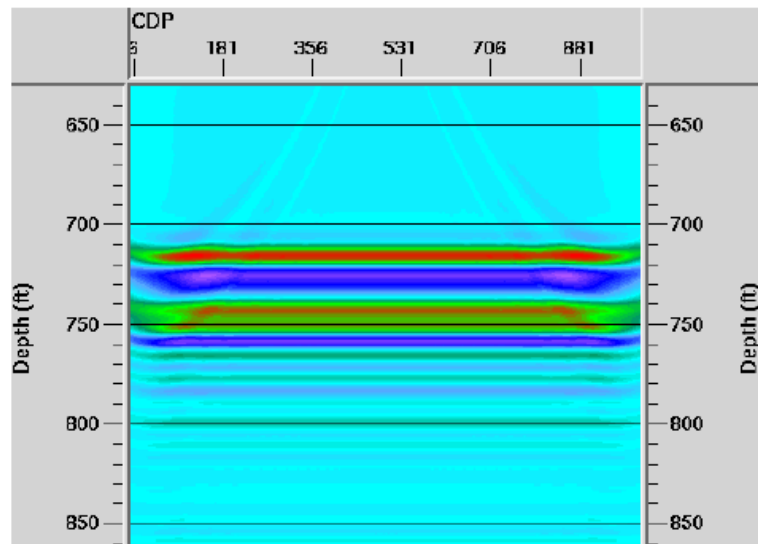


Figure 2.5: Seismic response of pre-production model to research the effect of foamy oil (Chen, 2004).

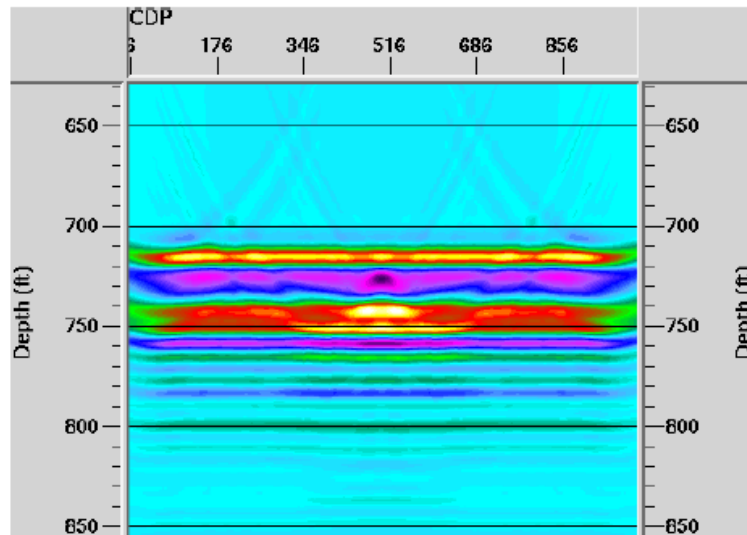


Figure 2.6: Seismic response of post-production model to research the effect of foamy oil (Chen, 2004).

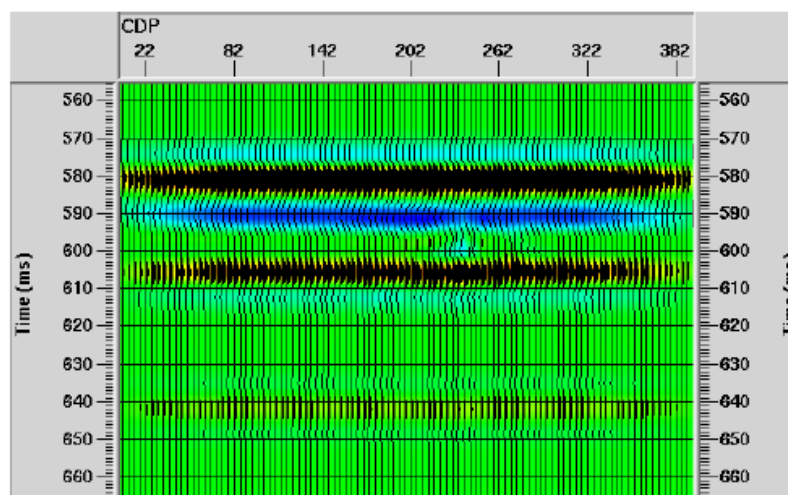


Figure 2.7: PP seismic response of post-production model to research the effect of wormholes (Chen, 2004).

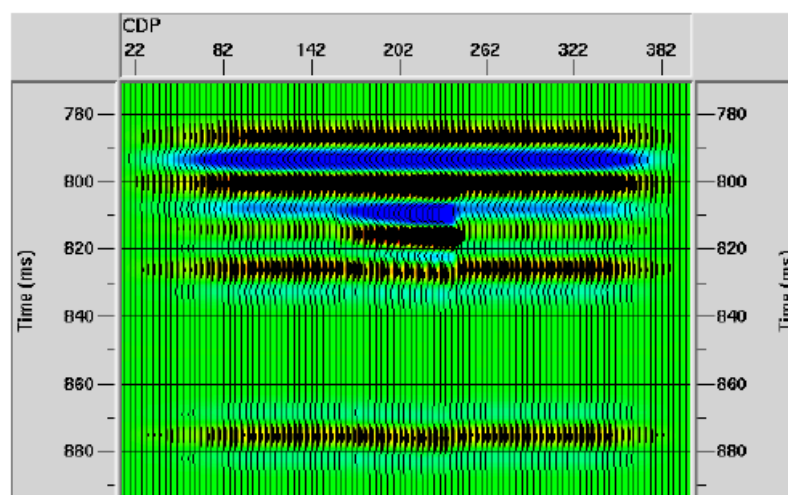


Figure 2.8: PS seismic response of post-production model to research the effect of wormholes (Chen, 2004).

2.4 Time-lapse seismic analysis of a heavy oil cold production field

The Provost Upper Mannville BB pool has been under cold production since the early 1980's. There have been three 3D surveys over the pool since 1987. Zou et al.(2004)

studied two of these surveys, which were acquired in 1987 and 1996. The McLaren member (about 660 ms) and a reference reflection (about 940 ms) were interpreted on both surveys. Horizon slices for the McLaren were generated from the correlated volumes, and the resulting seismic amplitude maps are shown in Figures 2.9 and 2.10. Since the McLaren is represented by a trough, the mapped amplitudes are negative (blue). Production began after the 1987 survey in wells delineated by black squares, and wells that stopped producing at least one year before the 1996 survey are marked by yellow ellipses (Figure 2.10).

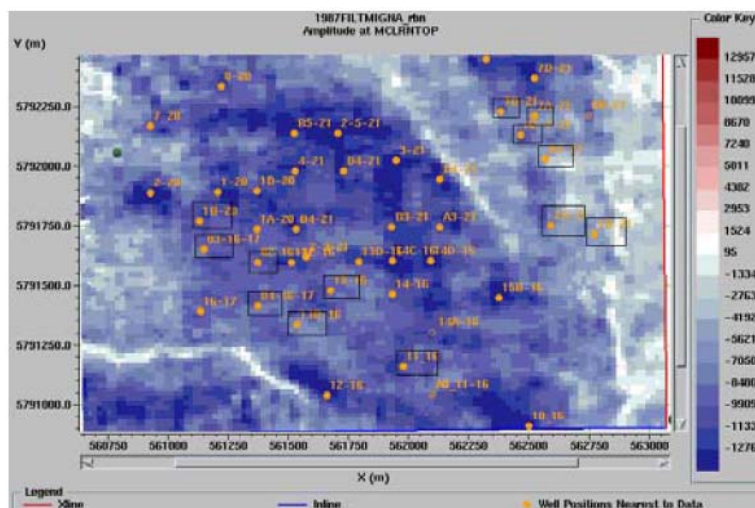


Figure 2.9: Amplitude map for McLaren event from 1987 survey (Zou et al., 2004).

The largest amplitudes (dark blue) on the McLaren horizon correlate well with producing wells (black squares; Figures 2.9 and 2.10). Shut-in wells appear to be in areas of smaller amplitudes (black squares and yellow circles; Figure 2.10). This seems to imply that there is some relationship between the dim amplitudes and the shut-in wells. If the shutting of the wells was related to the water flooding, these dim amplitudes may be explained. Water saturation can reduce the acoustic impedance contrast between the reservoir and the overlying shale, thereby causing smaller amplitudes. Wells that were

producing during both surveys are almost all in high amplitude zones, except for wells 16-17 and 14-16. Since the original seismic processing may not have been “true amplitude” processing, relative amplitudes may not be consistent within each survey, and this should be taken into consideration.

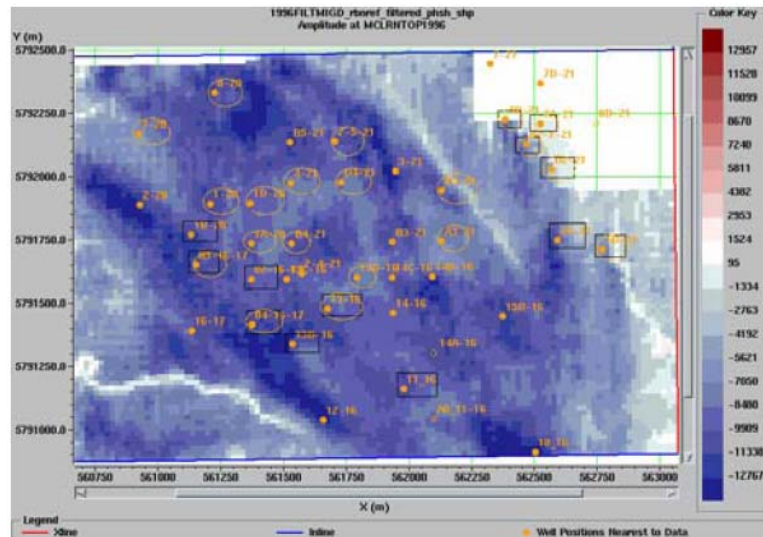


Figure 2.10: Amplitude map for McLaren event from 1996 survey (Zou et al., 2004).

From the above analysis, Zou et al. were confident that the high amplitude zones correspond to areas of acoustic impedance change due to production, possibly due to formation of wormholes and foamy oil.

A velocity decrease due to production causes travelttime delays. Isochron values were derived for the McLaren to reference reflection interval for both surveys. The 1987 isochron was then subtracted from the 1996 isochron (Figure 2.11). Wells circled in black have a cumulative production of over 15,000 m³. Since the relationship between oil production and sand production was not derived, they assumed that high oil production may correspond to higher sand production. Therefore, high production wells would correspond to larger diameter or longer wormholes, higher foamy oil saturation, and

greater acoustic impedance. Figure 2.11 shows a possible correlation between high production and traveltime delays for up to 7 ms, which is larger than the sample interval. The blue polygon is the estimated wormhole and foamy oil zone. High values on the left edge were considered to be caused by a boundary statics problem.

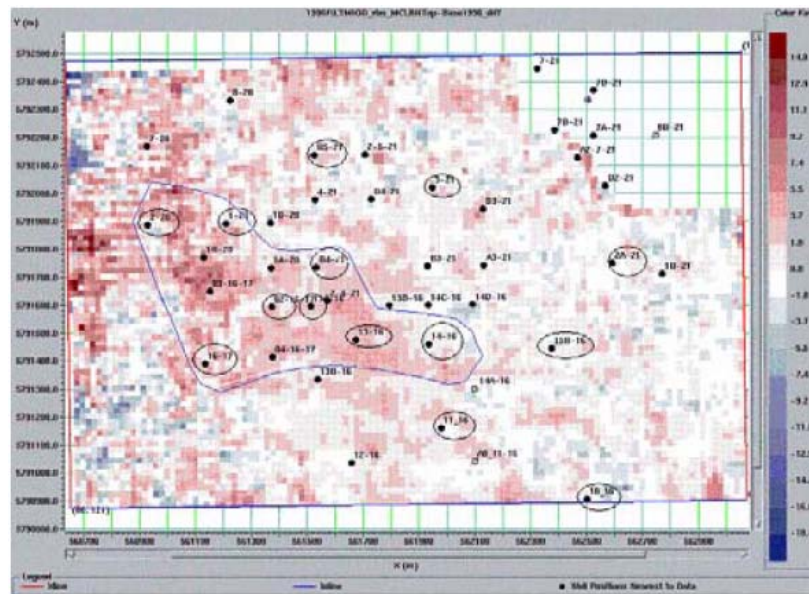


Figure 2.11: Time difference map of the 1996 isochron and the 1987 isochron (Zou et al., 2004). In the grid, each square is 100m x 100m.

CHAPTER 3

SEISMIC ROCK PHYSICS FOR HEAVY OIL

During the past 50 years or so, tremendous progress has been made in studying physical properties of rocks and minerals in relation to seismic exploration. In exploration seismology, subsurface rock and fluid information influence seismic waves in the form of traveltimes, reflection amplitudes, and phase variations. Seismic data are now commonly analyzed for determining lithology, porosity, pore fluids, and fluid saturations, because rock physics connects seismic data and reservoir properties and parameters. Seismic properties are affected in complex ways by many reservoir properties, such as pressure, temperature, fluid saturation, fluid type, porosity, and pore type (Wang, 2001). These factors are often interrelated or coupled with each other. In order to understand the rock physics application to seismic interpretation, the investigation of the effect of single factor can be studied while holding all other factors.

3.1 Fluid substitution: the Gassmann's Equation

Gassmann's (1951) equation has been used for calculating the effect of fluid substitution on seismic properties using the matrix properties. It predicts the bulk modulus of a fluid-saturated porous medium using the known bulk moduli of the solid matrix, the frame and the pore fluid in the following manner:

$$K^* = K_d + \frac{(1 - K_d / K_m)^2}{\frac{\phi}{K_f} + \frac{1 - \phi}{K_m} - \frac{K_d}{K_m^2}}, \quad (3.1)$$

where, K^* , K_d , K_m , K_f , and ϕ are the saturated porous rock bulk modulus, the frame rock

bulk modulus, the matrix bulk modulus, the fluid bulk modulus and the porosity. It is assumed that the shear modulus μ^* of the saturated rock is not affected by fluid saturation, so that:

$$\mu^* = \mu_d \quad , \quad (3.2)$$

where μ_d is the frame shear modulus. It is important to point out that the frame moduli are not the same as the dry moduli (Wang et al. 2001). With the correct use of the Gassmann's equation, frame moduli should be measured at irreducible saturation conditions of the wetting fluid (normally water). The overdrying of a rock in the laboratory will result in erroneous results for the purposes of Gassmann's equation.

P-wave and S-wave velocities, V_p and V_s , for an isotropic, homogeneous, elastic material are given by:

$$V_p = \sqrt{\frac{K^* + 4\mu^*/3}{\rho^*}} \quad , \quad (3.3)$$

and

$$V_s = \sqrt{\frac{\mu^*}{\rho^*}} \quad , \quad (3.4)$$

where ρ^* is the saturated rock bulk density and can be calculated as:

$$\rho^* = \rho_m(1 - \phi) + \rho_f\phi \quad , \quad (3.5)$$

where ρ_m and ρ_f are the densities of solid grains and the fluid mixture at reservoir conditions.

Equations (3.1) to (3.5) establish the relationships between the rock moduli and the seismic velocities. The accuracy of the Gassmann's equation for calculating the seismic velocities is based on some basic assumptions (Wang, 2001):

- (1) The rock (both the matrix and the frame) is macroscopically homogeneous;

- (2) All the pores are interconnected or communicating;
- (3) The pores are filled with a frictionless fluid (liquid, gas, or mixture);
- (4) The pore fluid does not interact with the solid in a way that would soften or harden the frame.

Assumption (1) is common to many theories of wave propagation in porous media. The frequency ranges from seismic bandwidths to laboratory experiments generally assure that the wavelengths are long enough compared to the grain and pore size. Assumption (2) implies that the porosity and permeability are high and there are no isolated or poorly connected pores in the rock. For seismic waves, however, only unconsolidated sands can approximately meet this assumption because of the sand's high porosity and permeability (Wang, 2001). Assumption (3) implies that the viscosity of the saturating fluid is zero. In reality, all fluids have finite viscosities, so most calculations using the Gassmann's equation will violate this assumption. This may be the most questionable assumption for heavy oil, especially at cold temperatures (about 20-40 °C). Assumption (4) ignores any effects of chemical and physical interactions between the rock matrix and the pore fluid. It is difficult to give an explicit description for the interaction.

To research the effect of the fluid displacement, Wang (2001) compared the results from Gassmann's equation and laboratory results. He concluded that the Gassmann-predicted and the laboratory measured effects of fluid displacement on seismic properties might be directly applied to 4D seismic feasibility studies and interpretations, even though the above assumptions are violated to some extent in the real world.

3.2 Rock physics for heavy oil

Heavy oil is a viscoelastic liquid. At the frequencies and temperatures of interest, heavy hydrocarbon liquids possess elastic properties that are very different from those of water. More importantly, the heavy hydrocarbon has a nonzero rigidity due to their high viscosity. Viscosity is often the limiting factor in heavy oil production, and it also has a strong influence on seismic properties. Although viscosity is influenced by pressure and gas content, it is primarily a function of oil gravity and temperature. The shear wave results for the very heavy oil sample (API=-5) are shown in Figure 3.1 (Batzle et al., 2006). At low temperatures (-12.5 °C), a sharp shear arrival is apparent. Thus, by many definitions, because this oil has a shear modulus, it is a solid, or glass. Increasing the temperature not only decreases the shear velocity, but also dramatically reduces the shear wave amplitude. At this point, this oil is only marginally solid. Figure 3.2 shows the derived effective bulk and shear moduli for this heavy oil (Batzle et al., 2006). Both moduli decrease approximately linearly with increasing temperature, and the shear modulus approaches zero at about 80 °C.

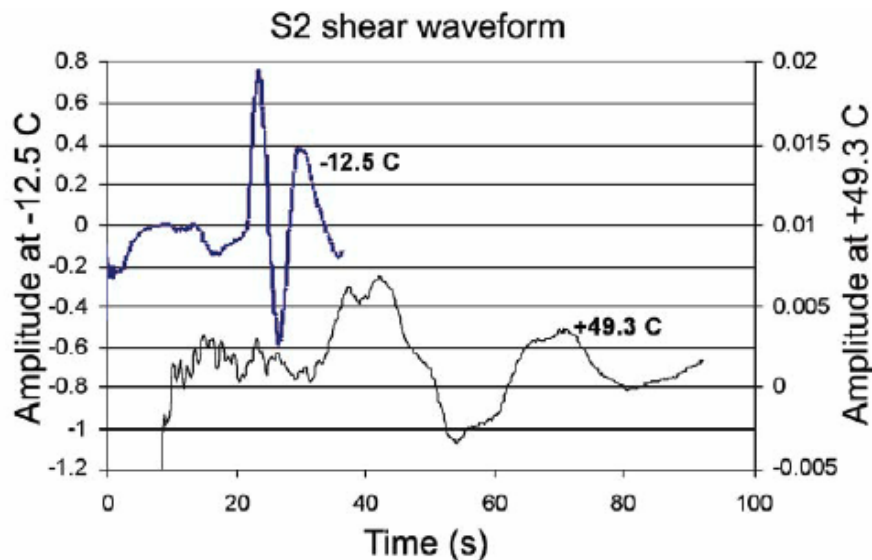


Figure 3.1: Ultrasonic shear waveforms in very heavy oil at -12.5 °C and 49.3 °C (Batzle et al., 2006).

As we have seen, a shear wave can propagate through very viscous fluids. Not only will temperature play a major role, but there also will be a strong modulus or velocity dependence on frequency. Figure 3.3 shows strong temperature and frequency dependence of the shear properties in Uvalde heavy oil with API=-5 (Batzle et al., 2006). At low temperature (0 °C), this oil acts like a solid. However, by +20 °C, the shear properties are in transition. At high frequencies, such as with laboratory ultrasonics, this material is still effectively a solid. At seismic frequencies, however, the material can go through shear relaxation and acts like a liquid, with no shear modulus. For this oil at +40 °C, ultrasonics is in a completely different viscoelastic regime and will not give results representative of properties at seismic frequencies. Logging frequencies can be in this transition region and yield some intermediate value between seismic and ultrasonic frequencies.

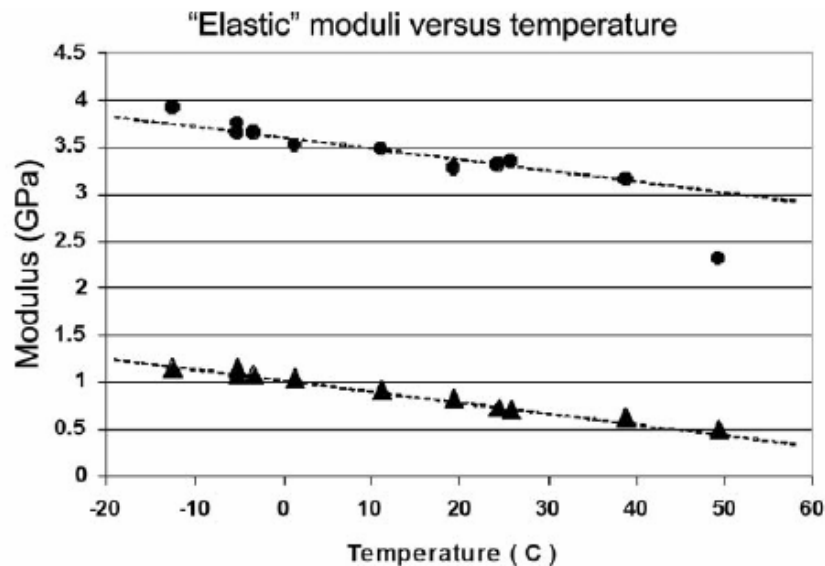


Figure 3.2: Elastic moduli of the heavy oil from ultrasonic data. The effective shear modulus (triangles) drops toward zero as temperatures approach 80 °C (Batzle et al., 2006).

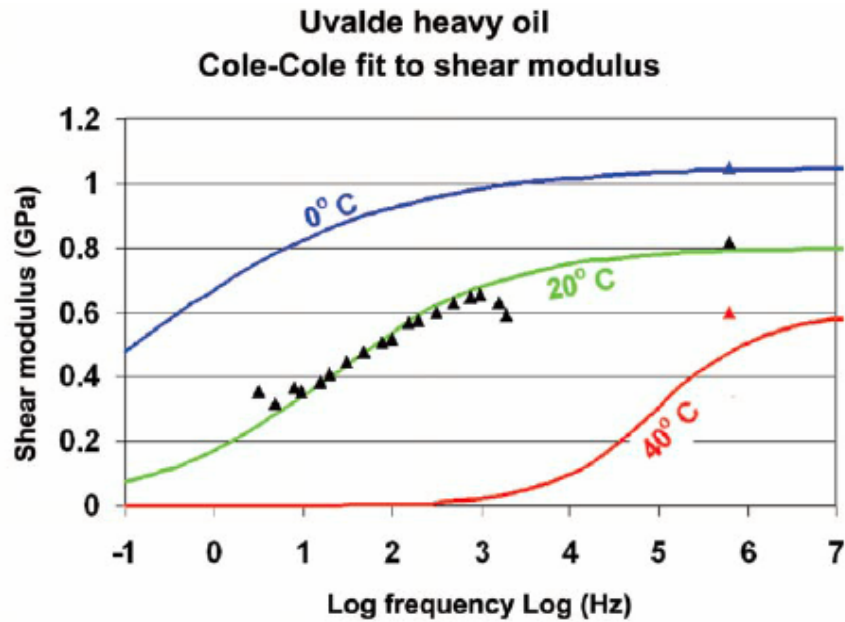


Figure 3.3: Measured (triangles) and calculated (lines) shear modulus in Uvalde heavy oil (API=-5) using a viscoelastic liquid (Cole-Cole) model (Batzle et al., 2006).

As mentioned in the first part, Gassmann's equation was based on the assumption that the viscosity of the saturating fluid is zero and was not derived to describe porous material saturated with a viscoelastic liquid. Thus, Gassmann's equation is probably inappropriate for heavy oil sands in low temperature. Because the stiffness of the frame is small in unconsolidated sands, Hornby et al. (1987) predicted the behavior of oil sands using scattering theory, which is equivalent to the Hashin-Shtrikman lower bound. The model assumes that the sands grains are suspended in a host of heavy hydrocarbons. The saturated bulk modulus is (Hornby et al., 1987):

$$K^* = K_f + \frac{1 - \phi}{\frac{1}{K_m - K_f} + \frac{\phi}{K_f + \frac{4}{3}\mu_f}}, \quad (3.6)$$

and the saturated shear modulus is (Hornby et al., 1987):

$$\mu^* = \mu_f + \frac{1-\phi}{\frac{1}{\mu_m - \mu_f} + \frac{2\phi(K_f + 2\mu_f)}{5\mu_f(K_f + \frac{4}{3}\mu_f)}} , \quad (3.7)$$

where μ_f is the shear modulus of heavy oil, and other parameters are same as those in Gassmann's equation.

In the above equations, μ_f is considered to make contributions to the saturated moduli, meanwhile, which is assumed to be zero in Gassmann's equation. To manifest how much contribution is from μ_f for K^* , equation (3.6) can be re-written as:

$$\begin{aligned} K^* &= K_f + \frac{1-\phi}{\frac{\phi}{K_f + \frac{4}{3}\mu_f} \left[1 + \frac{K_f + \frac{4}{3}\mu_f}{\phi(K_m - K_f)} \right]} \\ &= K_f + \frac{(1-\phi) \left(K_f + \frac{4}{3}\mu_f \right)}{\phi} \cdot \frac{1}{1 + \frac{K_f + \frac{4}{3}\mu_f}{\phi(K_m - K_f)}} , \end{aligned} \quad (3.8)$$

$$\therefore K_m \gg K_f, \text{ and } K_m \gg \mu_f ,$$

$$\therefore K_f + \frac{4}{3}\mu_f < \phi(K_m - K_f) ,$$

and

$$\frac{K_f + \frac{4}{3}\mu_f}{\phi(K_m - K_f)} < 1 .$$

If $K_f=2.3$ GPa, $\mu_f=1.0$ GPa, $K_m=36$ GPa and $\phi=0.3$, then:

$$\frac{K_f + \frac{4}{3}\mu_f}{\phi(K_m - K_f)} = \frac{2.3 + \frac{4}{3} \times 1.0}{0.3(36 - 2.3)} \approx 0.36 < 1 \quad .$$

So, equation (3.8) can be written as:

$$\begin{aligned} K^* &\approx K_f + \frac{(1-\phi)\left(K_f + \frac{4}{3}\mu_f\right)}{\phi} \left[1 - \frac{K_f + \frac{4}{3}\mu_f}{\phi(K_m - K_f)} \right] \\ &= 2.3 + \frac{0.7(2.3 + 1.33\mu_f)}{0.3} \left(1 - \frac{2.3 + 1.33\mu_f}{10.11} \right) \\ &= 2.3 + \frac{7}{3} \left[2.3 - \frac{2.3(2.3 + 1.33\mu_f)}{10.11} + 1.33\mu_f - \frac{1.33\mu_f(2.3 + 1.33\mu_f)}{10.11} \right] \\ &= 2.3 + \frac{7}{3} (2.3 - 0.52 - 0.3\mu_f + 1.33\mu_f - 0.3\mu_f - 0.18\mu_f^2) \\ &= 2.3 + \frac{7}{3} (1.78 + 0.73\mu_f - 0.18\mu_f^2) \\ &= 6.45 + 1.7\mu_f - 0.42\mu_f^2 \quad . \end{aligned} \quad (3.9)$$

From equation (3.9), the approximate contribution from μ_f is:

$$C_f = 1.7\mu_f - 0.42\mu_f^2 \quad . \quad (3.10)$$

For $\mu_f=1.0, 0.5, 0.25,$ and 0.1 GPa separately, $C_f=1.28, 0.75, 0.4$ and 0.16 GPa respectively. So, even though $\mu_f=0.25$ GPa, the contribution from μ_f is more than 5% of total saturated bulk modulus, and the shear modulus of heavy oil is not negligible.

3.3 An in-situ example of heavy oil

Heavy oil cold production is being carried out in Plover Lake oil field and the in-situ reservoir parameters from an oil well are listed in Table 3.1, the reservoir temperature is 27°C and the gravity of heavy oil is API=12.1. From previous part and Figure 3.3, we know that the heavy oil sample with a gravity of API=-5 can go through

shear relaxation and acts like a liquid with no shear modulus at seismic frequencies by +20°C. So, for the in-situ heavy oil in Plover Lake with an API=12.1, it should be acceptable that the heavy oil acts like a liquid at seismic frequencies by 27°C. To test the feasibility of both Gassmann's equation and equations (3.6) and (3.7) from scattering theory, one in-situ well with dipole sonic log data and density log data is selected from Plover Lake oil field to do the calculation. To simplify the calculation, average values of production zone are estimated for P-wave velocity, S-wave velocity and density for pre-production condition (Table 3.2).

Table 3.1: Reservoir parameters for the in-situ well.

Heavy-oil API	12.1
Specific gravity of methane	0.574
Solution gas-oil ratio (m ³ /m ³)	16.64
Reservoir temperature(°C)	27
Reservoir pressure(MPa)	6.4
Water saturation(%)	25
Oil saturation(%)	75
Gas saturation(%)	0
Water salinity(ppm)	19,280

Table 3.2: Estimated average values of production zone for V_p , V_s , and ρ^* .

P-wave velocity V_p (km/s)	S-wave velocity V_s (km/s)	Density ρ^* (g/cc)
3.1	1.53	2.13

From equation (3.4), we can get saturated shear modulus for pre-production condition:

$$\mu^* = \rho^* V_s^2 = 2.13 \times 1.53^2 \approx 5.00 \text{ (GPa)} .$$

Also from equation (3.3), saturated bulk modulus is available:

$$K^* = \rho^* V_p^2 - \frac{4}{3} \mu^* = 2.13 \times 3.1^2 - \frac{4}{3} \times 5.00 = 13.8 \text{ (GPa)} .$$

Moreover, based on Batzle-Wang formulas (Batzle et al., 1992) and from the in-situ reservoir parameters in Table 3.1, we can calculate fluids moduli and densities in the in-situ condition and listed in Table 3.3.

Table 3.3: Fluid properties for pre-production condition.

Parameters	Oil	Gas	Brine
Density (g/cc)	0.97	0.048	1.01
Bulk modulus (GPa)	2.2166	0.01	2.37

Gas-oil ratio (GOR) to calculate above fluids properties is 14.678, which is bubble point for in-situ reservoir parameters for pre-production condition. If GOR is bigger than this value, the calculated bulk modulus of heavy oil will decrease dramatically, as shown in Figure 1.10. For GOR=16.64, the calculated heavy oil bulk modulus is 0.1946 GPa, which is about the bulk modulus of foamy oil and is the case for post-production condition.

Right now, we need to examine the physical properties of solid matrix mineral. Han et al. (2004) show that matrix mineral moduli are not constant and can vary across a wide range, depending on mineral composition, distribution and in-situ conditions. For sandstone, mineral bulk modulus can increase by more than 10% with increasing differential pressure; for shaly sandstones, the mineral bulk modulus decreases about 1.7 GPa per 10% increment of clay content. Table 3.4 (Han et al., 2004) lists mineral moduli for shaly sands, where C is the fractional clay content, P_d is differential pressure, K_o and

μ_o are mineral moduli (different denotation from K_m and μ_m). Because the in-situ reservoir is about 820 meters in depth, and very low fractional clay content, the differential pressure P_d is between 10-20 MPa and C is almost zero, we choose $K_m \approx 39$ GPa (K_o in the table), $\mu_m \approx 27$ GPa (μ_o in the table). As to mineral density, we can use book value, $\rho_m \approx 2.65$ g/cc.

Table 3.4: Mineral moduli for shaly sands (Han et al., 2004).

P_d (MPa)	$C = 0$		$C = 0.1$		$C = 0.2$	
	K_o (GPa)	μ_o (GPa)	K_o (GPa)	μ_o (GPa)	K_o (GPa)	μ_o (GPa)
40	39.03	32.83	37.27	29.40	35.51	26.16
30	39.08	31.91	37.26	28.56	35.44	25.40
20	39.27	30.45	37.30	27.29	35.35	24.30
10	38.74	26.46	36.72	25.73	34.72	22.94

From saturated density, densities of all constitutes and their fractions, we can get reservoir porosity ϕ based on following equation:

$$\rho^* = \rho_m(1 - \phi) + \phi(S_w\rho_w + S_o\rho_o + S_g\rho_g), \quad (3.11)$$

where ρ_w , ρ_o , and ρ_g are densities of brine, heavy oil and gas at in-situ conditions; S_w , S_o and S_g are saturations of brine, heavy oil and gas respectively.

If

$$\begin{aligned} \rho_f &= S_w\rho_w + S_o\rho_o + S_g\rho_g = 0.25 \times 1.01 + 0.75 \times 0.97 + 0.00 \times 0.048 \\ &= 0.2525 + 0.7275 + 0.00 \approx 0.98 \text{ (g/cc)}, \end{aligned} \quad (3.12)$$

then

$$\phi = \frac{\rho^* - \rho_m}{\rho_f - \rho_m} = \frac{2.13 - 2.65}{0.98 - 2.65} \approx 0.31, \quad (3.13)$$

where ρ_f is volume average of fluids densities.

First, let's test the feasibility of Gassmann's equation. For equations (3.1) and (3.2), unknown parameters K_d and μ_d can be given in following equations (Mavko and Mukerji, 1998a,b):

$$K_d = K_m(1 - \phi / \phi_c) , \quad (3.14)$$

$$\mu_d = \mu_m(1 - \phi / \phi_c) , \quad (3.15)$$

where, ϕ_c is critical porosity, separating mechanical and acoustic behavior of rocks into two distinct domains: load bearing and suspension. For sandstone, $\phi_c \approx 38\%$. So, in our case,

$$K_d = 39 \times (1 - 0.31 / 0.38) = 39 \times 0.184 \approx 7.184 \text{ (GPa)} ,$$

$$\mu_d = 27 \times (1 - 0.31 / 0.38) = 27 \times 0.184 \approx 4.968 \text{ (GPa)} ,$$

and

$$\mu^* = \mu_d = 4.968 \text{ (GPa)} .$$

There are two cases of interest for average fluid bulk modulus calculations (Mavko et al., 2005). When various fluids are mixed together uniformly, the average bulk modulus is Reuss average of these fluids bulk moduli:

$$\frac{1}{K_f^R} = \frac{S_w}{K_w} + \frac{S_o}{K_o} + \frac{S_g}{K_g} . \quad (3.16)$$

If these fluids are mixed in a patchy way, the average bulk modulus is Voigt average:

$$K_f^V = S_w K_w + S_o K_o + S_g K_g , \quad (3.17)$$

where K_f^R and K_f^V are Reuss and Voigt average bulk modulus of fluids mixer respectively.

In the real world, the actual value of average bulk modulus (K_f) lies between the Reuss average and the Voigt average, and can be given as:

$$K_f = \frac{1}{2}(K_f^R + K_f^V) . \quad (3.18)$$

For the in-situ case,

$$\begin{aligned} K_f^R &= \left(\frac{0.25}{2.37} + \frac{0.75}{2.2166} + \frac{0.00}{0.01} \right)^{-1} \\ &= (0.1055 + 0.3383 + 0.00)^{-1} \approx 2.253 \text{ (GPa)} , \end{aligned}$$

$$\begin{aligned} K_f^V &= 0.25 \times 2.37 + 0.75 \times 2.2166 + 0.00 \times 0.01 \\ &= 0.5925 + 1.66245 + 0.00 \approx 2.255 \text{ (GPa)} , \end{aligned}$$

$$K_f = \frac{1}{2}(2.253 + 2.255) = 2.254 \text{ (GPa)} .$$

Now, all parameters for calculating the saturated bulk modulus (K^*) using equation (3.1) are available, and

$$\begin{aligned} K^* &= 7.184 + \frac{\left(1 - \frac{7.184}{39}\right)^2}{\frac{0.31}{2.254} + \frac{1-0.31}{39} - \frac{7.184}{39^2}} \\ &= 7.184 + \frac{0.6655}{0.1375 + 0.0177 - 0.0047} = 7.184 + 4.422 \approx 11.6 \text{ (GPa)} . \end{aligned}$$

Equations (3.6) and (3.7) from scattering theory are only applicable when pore fluid is just heavy oil, otherwise, if there is water and/or gas, the calculated saturated shear modulus μ^* will be zero and the velocity of shear wave will be zero, too. In this case, we assume that pore fluid is just heavy oil, and $K_f=2.2166$ GPa. At seismic frequencies, by +20°C, from Figure 3.3, we can assume that $\mu_f=0.6$ GPa, and

$$\begin{aligned}
K^* &= 2.2166 + \frac{1-0.31}{\frac{1}{39-2.2166} + \frac{0.31}{2.2166 + \frac{4}{3} \times 0.6}} \\
&\approx 2.2166 + \frac{0.69}{0.027 + 0.103} \approx 2.2166 + 5.31 \approx 7.53 \text{ (GPa)}, \\
\mu^* &= 0.6 + \frac{1-0.31}{\frac{1}{27-0.6} + \frac{2 \times 0.31 \times (2.2166 + 2 \times 0.6)}{5 \times 0.6 \times \left(2.2166 + \frac{4}{3} \times 0.6\right)}} \\
&= 0.6 + \frac{0.69}{0.0379 + \frac{2.1183}{9.0498}} \approx 3.14 \text{ (GPa)}.
\end{aligned}$$

Table 3.5 lists all calculated saturated moduli from well log data, Gassmann's equation, and scattering theory. Due to the application limitation of scattering theory, its results are not better than those from Gassmann's equation. Gassmann's equation gives much better estimations of both saturated bulk modulus and shear modulus. As stated previously, for oil that is not extremely heavy, the shear modulus of heavy oil is negligible and Gassmann's equation is still applicable at seismic frequencies for temperatures of +20°C. This conclusion can be further supported by one of the results in Chapter 5.

Table 3.5: Calculated saturated moduli from well log data, Gassmann's equation, and scattering theory.

Parameters	Well log	Gassmann's equation	Scattering theory
Saturated bulk modulus K^* (GPa)	13.8	11.6	7.53
Saturated shear modulus μ^* (GPa)	5.0	4.968	3.14

CHAPTER 4

EFFECTS OF HEAVY OIL COLD PRODUCTION ON RESERVOIR PROPERTIES

4.1 Difference of heavy oil physical properties between pre- and post-production

As described in Chapter 1, heavy oil reservoirs experience a dramatic change as a result of cold production: porosity increases due to sand extraction, pore pressure decreases due to porosity increase, and there is a phase transition of heavy oil to foamy oil due to pore pressure decrement. Table 4.1 lists a typical comparison of reservoir parameters between pre- and post cold production in Plover Lake oil field. These changes of reservoir parameters, especially the decrement of reservoir pressure from 6.4 MPa for pre-production to 0.6 MPa for post-production, will absolutely change the physical properties of heavy oil in the reservoir. Table 4.2 shows calculated physical properties of reservoir fluids before and after cold production based on the Batzle-Wang formulas (Batzle et al., 1992) and reservoir parameters are from Table 4.1, except solution gas oil ratio.

If GOR (gas-oil ratio) = 16.64, the calculated bulk modulus of heavy oil is 0.1946 GPa. This is a very low value, meaning that heavy oil is already in the phase of foamy oil before cold production. In this case, we use GOR=14.678, which is the saturation GOR (bubble point) calculated by software, and the calculated bulk modulus is 2.2166 GPa, which is much higher and keeps accordance with the lab measurement (Figure 1.10) of heavy oil bulk modulus for pre-production. When GOR is more than 14.678, the calculated bulk modulus will decrease dramatically. We assume that there is some error in

measured reservoir parameters listed in Table 4.1.

Table 4.1: A typical comparison of reservoir parameters between pre- and post- cold production in Plover Lake oil field.

Parameters	Pre-production	Post-production
Heavy-oil API	12.1	12.1
Specific gravity of methane	0.574	0.574
Solution gas-oil ratio (m ³ /m ³)	16.64	0.9
Reservoir temperature(°C)	27	27
Reservoir pressure(MPa)	6.4	0.6
Water saturation(%)	25	19
Oil saturation(%)	75	62
Gas saturation(%)	0	19
Water salinity(ppm)	19,280	19,280

Table 4.2: Calculated physical properties of reservoir fluids for pre- and post- cold production.

Parameters	Pre-production			Post-production		
	Heavy oil	Gas	Water	Heavy oil	Gas	Water
Bulk modulus(GPa)	2.2166	0.01	2.37	0.0636	0.0008	2.34
Density(g/cc)	0.97	0.048	1.01	0.97	0.004	1.0088

Compared with the bulk modulus of heavy oil for pre-production (2.2166GPa), the bulk modulus of foamy oil for post-production is just about 0.0636 GPa, which is a dramatic decrease. Such a decrease will cause the reduction of P-wave velocity, and will absolutely affect the response of seismic survey. However, regional and lithologic variations in P-wave velocity may be even greater than these anomalies. Hence,

observations of P-wave velocity alone may not be sufficient to identify zones of interest. Theoretically and experimentally, the S-wave velocity of a porous rock has been shown to be less sensitive to fluid saturants than P-wave velocity, it can be used as a normalizing quantity with which to compare P-wave velocity, and observations of the ratio of the seismic velocities for P-wave and S-wave which traverse a changing or laterally varying zone could produce an observable anomaly which is independent of the regional variation in P-wave velocity (Tatham et al., 1976). Moreover, the V_p/V_s ratio is especially sensitive to the pore fluid found in sedimentary rocks. In particular, the V_p/V_s value is much lower (10-20%) for gas saturation than for liquid saturation, and there is a characteristic drop in V_p/V_s ratio for gas saturated sandstones (Tatham, 1982).

4.2 Effects of heavy oil cold production on V_p/V_s ratio

As discussed in Chapter 3, for extremely heavy oil, shear modulus of heavy oil is not negligible and Gassmann's equation is not suitable. For heavy oil with an API more than 10, the shear modulus of heavy oil is negligible for seismic frequencies at +20°C, and heavy oil acts still like a liquid, especially after cold production when foamy oil is created due to the dissolved gas from heavy oil, and the mobility of reservoir fluids is improved much. In this case, Gassmann's equation can still help us understand the response of heavy oil reservoir to seismic survey for pre- and post- cold production.

Using the patchy model, where $K^* = K_p + K_d$, Murphy et al.(1993) introduced another expression of Gassmann's equation (3.1) as:

$$\rho V_p^2 = K_p + K_d + \frac{4}{3}\mu^* \quad , \quad (4.1)$$

where K_p is the pore space modulus, other parameters are same as those described in Chapter 3. If we recall Gassmann's equation (3.1), K_p can be expressed as:

$$K_p = \frac{\alpha^2}{\frac{\alpha - \phi}{K_m} + \frac{\phi}{K_f}} , \quad (4.2)$$

where α is the compliance of the frame relative to that of the solid grains and is defined as:

$$\alpha = 1 - K_d / K_m . \quad (4.3)$$

From equation (3.14), equation (4.3) can be written as:

$$\alpha = 1 - (1 - \phi / \phi_c) = \phi / \phi_c . \quad (4.4)$$

While the explicit dependence of K_p on porosity is fairly weak, the implicit dependence through α cannot be neglected, because K_d is a strong function of porosity (equation 3.14). In practice, the contribution of K_p to V_p is quite significant at high porosities where the frame moduli (K_d, μ_d) are relatively weak. At low porosities, where $K_d \rightarrow K_m$ and $\alpha \rightarrow 0$, the effect of K_p is insignificant. It's good news for our case because most heavy oil reservoirs are less than 1000 meters in depth and reservoir porosities are around 30%. Hilterman (2001) gave an example (Figure 4.1). For the unconsolidated case, the dry-rock contribution (1.63 GPa) is only 30% that of the contribution from the fluid (5.51 GPa). The choice of pore-fluid saturant dominates the value obtained for V_p . However, the opposite is true for consolidated rocks. The pore-fluid contribution, be it water or gas, contributes little to the rock's total moduli. Accurate estimates of lithology and porosity are important when dealing with consolidated rocks (Hilterman, 2001).

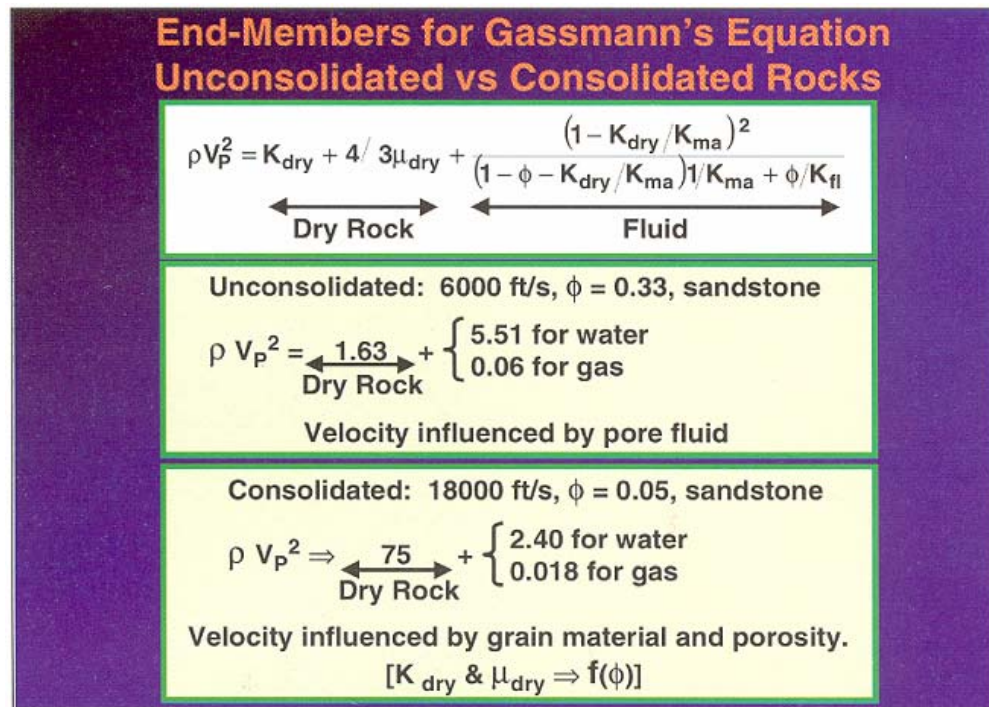


Figure 4.1: The contribution from the fluid is much higher in unconsolidated sands than in consolidated sands (Hilterman, 2001).

To explicitly reveal the dependence of K_p on porosity, equation (4.2) can be simplified as:

$$\begin{aligned} K_p &= \frac{\alpha^2}{\frac{(\alpha - \phi)K_f + \phi K_m}{K_m K_f}} = \frac{\alpha^2 K_m K_f}{\phi K_m + (\alpha - \phi)K_f} \\ &= \frac{\alpha^2 K_m K_f}{\phi K_m \left[1 + \frac{(\alpha - \phi)K_f}{\phi K_m} \right]} \end{aligned} \quad (4.5)$$

If $\phi = 30\%$, $\phi_c = 38\%$, $K_f = 1$ GPa, $K_m = 40$ GPa, then:

$$\alpha = \phi / \phi_c = 0.3 / 0.38 \approx 0.79 \quad ,$$

$$\frac{(\alpha - \phi)K_f}{\phi K_m} \approx \frac{(0.79 - 0.3) \times 1}{0.3 \times 40} \approx 0.04 \ll 1 \quad ,$$

and using the binomial approximation that $(1+x)^{-1} \approx 1-x$ for small x , equation (4.5) can be approximately written as:

$$\begin{aligned} K_p &\approx \frac{\alpha^2 K_m K_f}{\phi K_m} \left[1 - \frac{(\alpha - \phi) K_f}{\phi K_m} \right] \\ &= \frac{\alpha^2 K_f}{\phi} - \frac{\alpha^2 (\alpha - \phi)}{\phi^2 K_m} K_f^2 . \end{aligned} \quad (4.6)$$

To compare the two terms in equation (4.6), let's substitute real values into the two terms:

$$\begin{aligned} \frac{\alpha^2 K_f}{\phi} &= \frac{0.79^2 \times 1}{0.3} \approx 2.08 , \\ \frac{\alpha^2 (\alpha - \phi)}{\phi^2 K_m} K_f^2 &= \frac{0.79^2 \times (0.79 - 0.3)}{0.3^2 \times 40} \times 1^2 \\ &= \frac{0.306}{3.6} \approx 0.085 \ll 2.08 . \end{aligned}$$

So, the latter term is the second order compared with the first term, and equation (4.6) can be further simplified as:

$$K_p \approx \frac{\alpha^2}{\phi} K_f . \quad (4.7)$$

Substitute equation (4.4) into (4.7), then

$$K_p \approx \frac{\phi}{\phi_c^2} K_f . \quad (4.8)$$

Equation (4.8) explicitly reveals the proportional dependence of K_p on porosity and K_f , this relationship also keeps accordance with the fact that the contribution of K_p to V_p is quite significant at high porosities compared with that at low porosities. The contribution of K_f to V_p is the same fact.

By dividing equation (3.2) into (4.1), the velocity ratio may be naturally expressed in the terms of the moduli that are introduced above:

$$R^2 = \left(\frac{V_p}{V_s} \right)^2 = \frac{K_p}{\mu^*} + \frac{K_d}{\mu^*} + \frac{4}{3} . \quad (4.9)$$

Note that R^2 is always greater than 1.333. From equations (3.2), (3.14) and (3.15), we obtain:

$$\frac{K_d}{\mu^*} = \frac{K_m}{\mu_m} . \quad (4.10)$$

So, the ratio of the frame moduli K_d/μ^* is independent of the pore fluid. Finally, from above discussion, K_p/μ^* represents the pore fluid contribution, which is an important factor at high porosity and is insignificant at low porosity. This is the source that we can use time lapse technology to monitor the recovery process of unconsolidated reservoir.

From equations (3.2), (3.15) and (4.8), we can further reveal the contribution of porosity to V_p/V_s ratio:

$$\begin{aligned} \frac{K_p}{\mu^*} &\approx \frac{K_p}{\mu_m(1-\phi/\phi_c)} = \frac{K_p\phi_c}{\mu_m(\phi_c-\phi)} \\ &\approx \frac{\phi K_f \phi_c}{\mu_m \phi_c^2 (\phi_c - \phi)} = \frac{\phi K_f}{\mu_m \phi_c (\phi_c - \phi)} . \end{aligned} \quad (4.11)$$

Usually, $K_f^R \approx 0$, equation (3.18) can be written as:

$$K_f = \frac{1}{2}(K_f^R + K_f^V) \approx \frac{1}{2} K_f^V = \frac{1}{2}(S_w K_w + S_o K_o + S_g K_g) . \quad (4.12)$$

By substituting equations (4.10), (4.11) and (4.12) into (4.9), one obtains:

$$R^2 = \left(\frac{V_p}{V_s} \right)^2 \approx \frac{K_p}{\mu^*} + \frac{K_m}{\mu_m} + \frac{4}{3} = \frac{K_f \phi}{\mu_m \phi_c (\phi_c - \phi)} + \frac{K_m}{\mu_m} + \frac{4}{3}$$

$$\approx \frac{(S_w K_w + S_o K_o + S_g K_g)\phi}{2\mu_m \phi_c (\phi_c - \phi)} + \frac{K_m}{\mu_m} + \frac{4}{3} . \quad (4.13)$$

Equation (4.13) explicitly reveals the dependence of V_p/V_s ratio on porosity and fluids saturation. For a completely gas saturated reservoir, $K_f \approx 0$, $K_p/\mu^* \approx 0$ and equation (4.13) reduces to:

$$R^2 = \left(\frac{V_p}{V_s}\right)^2 \approx \frac{K_m}{\mu_m} + \frac{4}{3} . \quad (4.14)$$

The V_p/V_s ratio is constant and the smallest compared with other fluid saturations. For partial fluids saturation, K_f and ϕ have opposite effects on the V_p/V_s ratio, the larger value of K_f will increase the V_p/V_s ratio, and by contrast, larger porosity values will reduce the V_p/V_s ratio. Let's do some more work for these two points. For $\phi=0.31$, $\phi_c=0.38$, $K_m=39$ GPa, $\mu_m=27$ GPa, equation (4.13) is:

$$R^2 = 0.432K_f + 2.778 . \quad (4.15)$$

Figure 4.2 displays the effect of K_f on V_p/V_s ratio in this case and the V_p/V_s ratio will decrease with the reduction of K_f . As to the effect of porosity on V_p/V_s ratio, it is a little bit complicated. Figure 4.3 (Murphy et al., 1993) shows that V_p/V_s ratio will increase in different rates for different fluids partial saturation. The V_p/V_s ratio keeps constant for gas saturated sands, and will increase more for water saturated sands with the increment of porosity. From Table 4.1 and 4.2, we can get $K_f \approx 0.244$ GPa based on equation (3.18), and equation (4.13) is:

$$R^2 = \frac{0.244\phi}{10.26(0.38 - \phi)} + 2.778 . \quad (4.16)$$

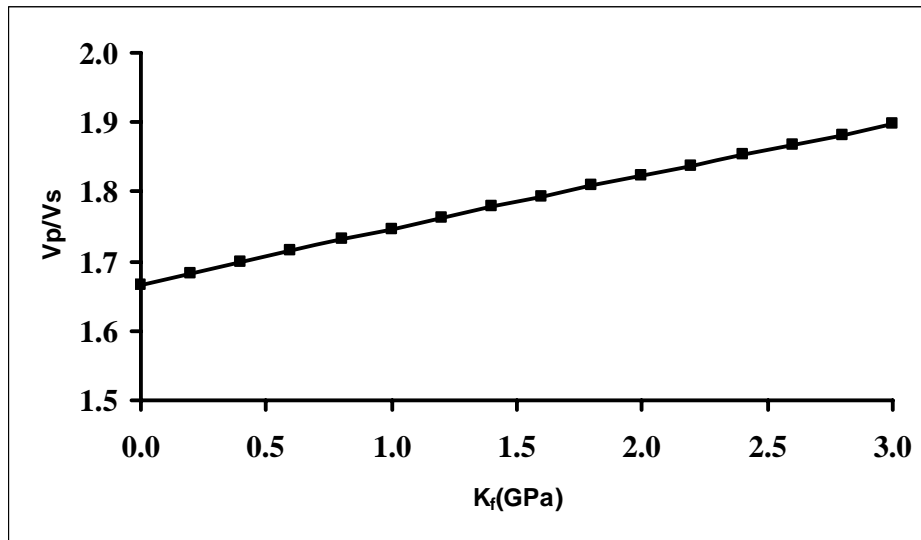


Figure 4.2: The effect of K_f on V_p/V_s ratio.

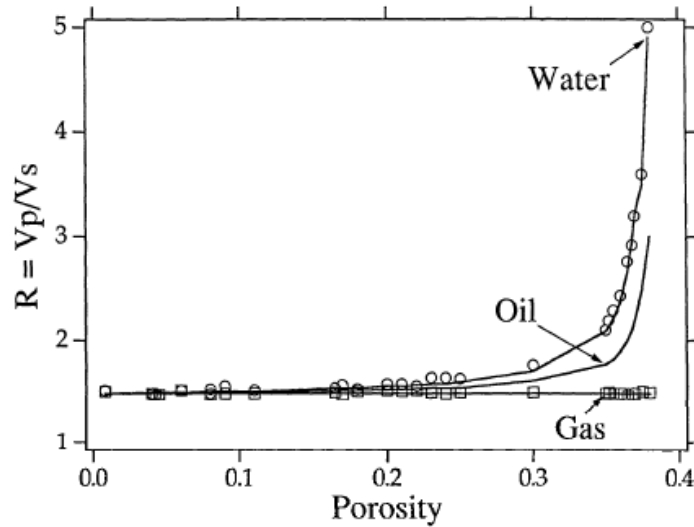


Figure 4.3: The velocity ratio $R=V_p/V_s$, plotted versus porosity as a function of pore fluid saturation for gas, oil, and water in clean quartz sandstones. The marks are laboratory measurements. The lines are the Gassmann's predictions (Murphy et al., 1993).

Figure 4.4 shows the result from equation (4.16). For $\phi < 0.30$, V_p/V_s ratio almost keeps constant and has very little increment with the improvement of porosity; but for

$\phi > 0.30$, V_p/V_s ratio will increase relatively quickly.

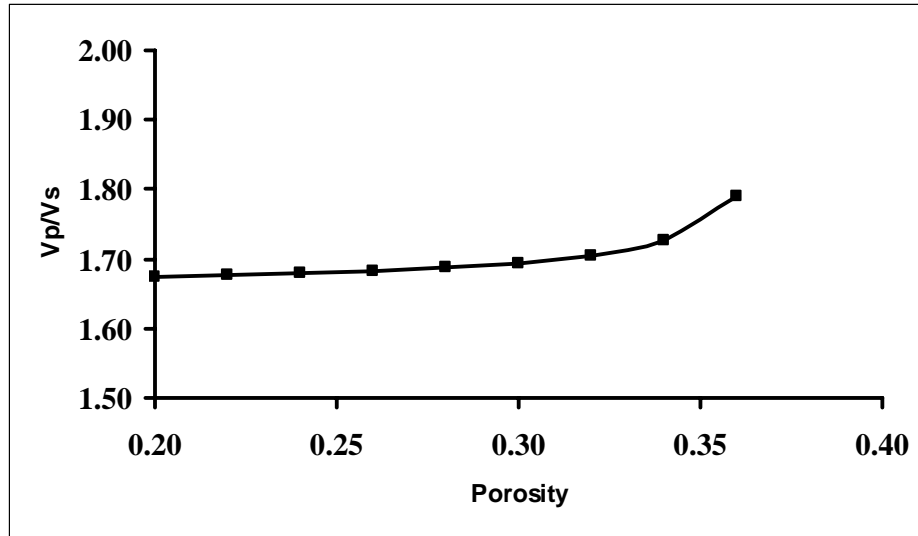


Figure 4.4: The effect of porosity on V_p/V_s ratio.

For the in-situ case, let's see how V_p/V_s ratio changes after heavy oil cold production. From Tables 4.1 and 4.2, and equation (3.18), we can get $K_f \approx 2.254$ GPa for pre-production, then from equation (4.15), $V_p/V_s \approx 1.937$. For post-production, from previous context, $K_f \approx 0.244$ GPa, which decreases dramatically due to the creation of foamy oil. If reservoir porosity is improved to 0.35 from 0.31, then from equation (4.16), $V_p/V_s \approx 1.748$, the reduction of V_p/V_s ratio is about 0.189 due to cold production. This value is for the assumption that fluids are mixed together between patchy and uniform. If fluids are mixed together uniformly, the bulk modulus K_f will be decreased to 0.004 GPa from 2.254 GPa due to cold production and the creation of foamy oil. Similarly, from equation (4.13), V_p/V_s ratio will be reduced to 1.668 from 1.937, the reduction value is 0.269. So generally, even though porosity has an opposite effect on V_p/V_s ratio, the reduction of fluids bulk modulus will have a more significant effect on V_p/V_s ratio, and V_p/V_s ratio will decrease after heavy oil cold production.

As to the effect of porosity on V_p/V_s ratio, there are several conflicting results published on various literatures. Castagna et al. (1985) establish general V_p/V_s ratio relationships for clastic silicate rocks by comparing in-situ and laboratory data with theoretical model data:

$$V_p/V_s = 1.33 + 0.63/(3.89 - 7.07\phi) \quad . \quad (4.17)$$

Equation (4.17) explicitly reveals the dependence of V_p/V_s ratio on porosity; for clean sand, the V_p/V_s ratio will increase with the increasing porosity.

Hornby et al. (1987) presented equations (3.6) and (3.7) rather than Gassmann's equations to determine the saturated moduli K^* and μ^* in oil sands. Figure 4.5 displays the theoretical V_p/V_s ratio of sand suspended in coal tar pitch at 0°C, and the increasing porosity increases V_p/V_s ratio too.

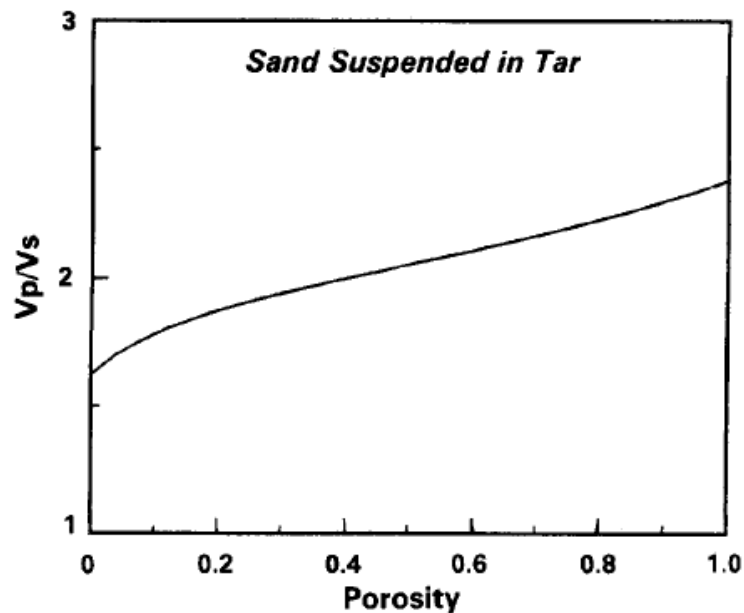


Figure 4.5: Theoretical V_p/V_s ratio of sand suspended in coal tar pitch at 0°C (Hornby et al., 1987).

Eberhart-Phillips et al. (1989) used a multivariate analysis to investigate the influence of effective pressure P_e , porosity ϕ , and clay content C on the compressional velocity V_p and shear velocity V_s of sandstones. In Figure 4.6, the combinations of (ϕ, C, P_e) predict a given V_p/V_s and V_s/V_p using their relationships are described by the intersection of the two surfaces. A normal to a V_p/V_s ratio line (arrow in Figure 4.6) shows that an increment in the V_p/V_s ratio indicates a decrement in porosity, which is opposite to the above mentioned conclusions, but this is good news for our research because the increasing porosity will further reduce the V_p/V_s ratio after heavy oil cold production, together with the reduction of the V_p/V_s ratio due to the creation of foamy oil, and it will be easier for the seismic survey to detect the reduction of the V_p/V_s ratio after production.

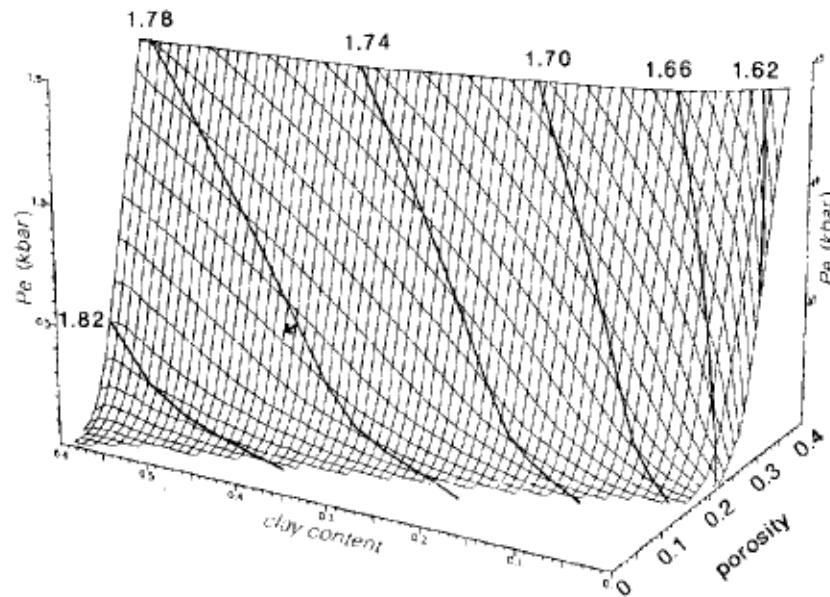


Figure 4.6: Influence of effective pressure P_e , porosity ϕ , and clay content C on V_p/V_s ratios indicated by the number next to lines (Eberhart-Phillips et al., 1989).

Zimmer et al. (2002) presented measurements of P-wave and S-wave velocities

through sand and glass bead samples at a range of porosities. They also discussed the effects of pressure, sorting, and compaction on the velocities and porosities, and the implications for the evaluation of pore pressures using V_p/V_s ratio in unconsolidated sands. V_p/V_s ratios for all the Gassmann fluid-substituted glass bead data are shown in Figure 4.7, plotted against pressure and color-coded by porosity. At low pressures, the fluid-substituted V_p/V_s ratio is a function of both the pressure and the porosity, with lower porosities corresponding to higher V_p/V_s ratios. As the relative porosity effect at high pressures is similar for the P-wave and S-wave velocities, there is relatively little scatter in V_p/V_s ratio above 10 MPa, which is close to the effective pressure for our in-situ reservoir condition.

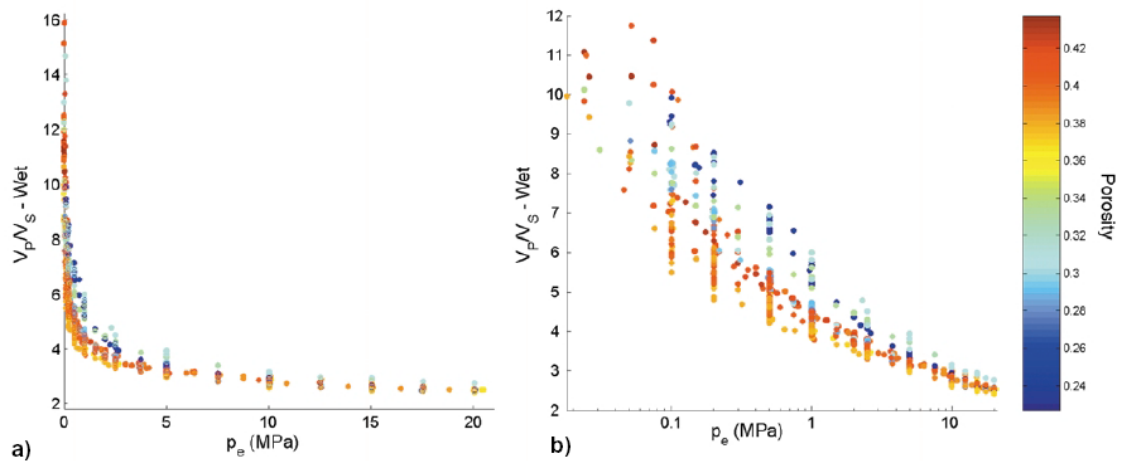


Figure 4.7: V_p/V_s ratios for all the Gassmann fluid-substituted glass bead data are plotted against pressure and color-coded by porosity. (a) Linear scale pressure-axis. (b) Log scale pressure-axis (Zimmer et al., 2002).

4.3 Effect of pressure on the V_p/V_s ratio

As described in the first Chapter, during heavy oil cold production, the pore pressure will decrease with the simultaneous extraction of sand and the increasing

porosity, the differential pressure will increase subsequently. Research results about the effects of differential pressure on V_p / V_s ratio published on literatures are similar. Eberhart-Phillips et al. (1989) used a multivariate analysis to investigate the influence of effective pressure P_e , porosity ϕ , and clay content C on the compressional velocity V_p and shear velocity V_s of sandstones. They concluded that V_p / V_s ratio is largest at very low P_e and decreases as P_e increases. Even though there are variations among the individual samples, the general pattern of behavior is common to all rocks measured. Zimmer et al. (2002) presented similar results and has been described in previous part.

Prasad (2002) published acoustic measurements in unconsolidated sands at low effective pressure and overpressure detection. Figure 4.8 displays V_p / V_s ratio as a function of pressure for the data collected in his study. The figure reveals an exponential increase in V_p / V_s ratio with differential pressure reduction. Prasad also gave an empirical fit to the data as:

$$V_p / V_s = 5.6014P_d^{-0.2742} \quad , \quad (4.18)$$

where P_d is differential pressure in MPa. If pressure gradient is about 1psi/ft, for the in-situ reservoir at the depth of about 820 meters, the confining pressure P_c is about 18.55 MPa. From table 4.1, the differential pressure will be increased to 17.95 MPa from 12.15 MPa after heavy oil cold production, and the calculated V_p / V_s ratio will be decreased to 2.538 from 2.824. The reduction of V_p / V_s ratio is about 10%. These calculated V_p / V_s ratios should be for water saturated condition.

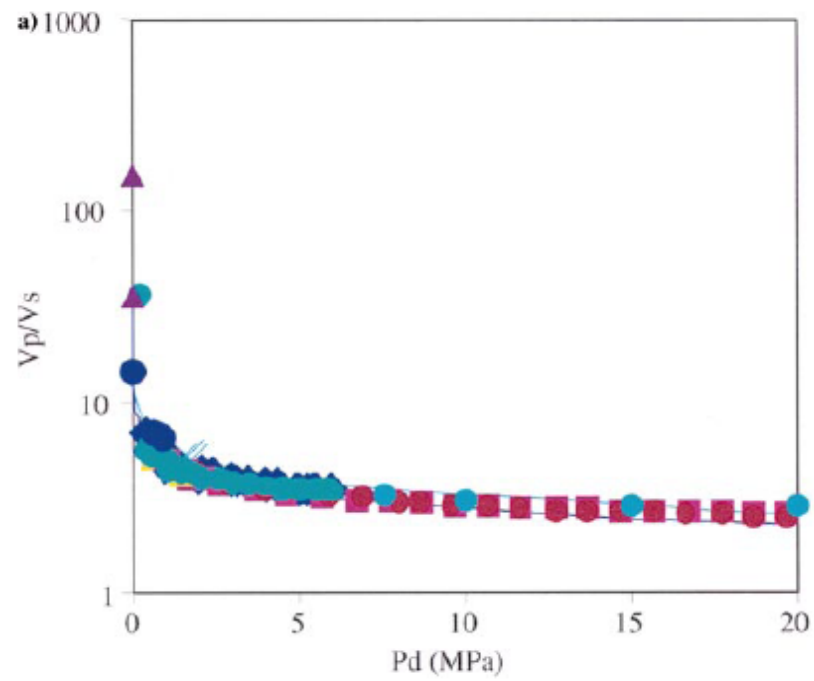


Figure 4.8: Relationship between V_p/V_s ratio and differential pressure for the data collected in Prasad's study (Prasad, 2002).

CHAPTER 5

THE ROBUSTNESS OF V_P/V_S MAPPING

5.1 Introduction

Multicomponent seismology is a useful tool for enhanced reservoir characterization of heavy-oil fields. As shown by Watson et al. (2002) and Lines et al. (2005), multicomponent data can provide maps of the P-wave to S-wave velocities (V_P/V_S), and these V_P/V_S maps provide important information about lithology and reservoir changes. In this discussion largely taken from Zhang and Lines (2006), one can show that V_P/V_S mapping, as derived from traveltimes measurements on vertical and radial component data, is a robust procedure. The following discussion explores two aspects of this type of V_P/V_S mapping. First, I explore the spectral differences of PP and PS seismic volumes and design band pass filters that can significantly improve the quality of V_P/V_S maps. Second, I perform an error analysis of this mapping and show that the derivation of V_P/V_S maps from reflection traveltimes picks is not overly sensitive to the choice of reflecting horizons above and below the reservoir.

The computation of V_P/V_S maps from 3C/3D seismic data is straight-forward for flat-layered geology where the vertical component contains predominantly PP reflections and the radial component contains predominantly PS reflections. By picking reflection times for horizons above and below a reservoir on both the vertical and radial components, Watson (2004) (among others) has shown that the V_P/V_S ratio can be derived from the following equation:

$$\frac{V_P}{V_S} = \frac{2\Delta t_{PS} - \Delta t_{PP}}{\Delta t_{PP}}, \quad (5.1)$$

where Δt_{PP} is the interval travel time of the interpreted interval from PP sections and Δt_{PS} is the interval travel time from PS sections for the same pairs of reflectors on both sections. Watson et al. (2002), Lines et al. (2005), Pengelly (2005), Zhang and Lines (2006) describe successful applications of this mapping to the characterization of different heavy-oil fields in Western Canada.

I noted the robustness of V_P/V_S mapping using multicomponent traveltimes in equation (5.1) through a sequence of mapping experiments for the Plover Lake data set, as discussed by Lines et al. (2005). Several interpreters constructed V_P/V_S maps using prominent reflectors above and below the target formation, the Mississippian oil sands of the Bakken formation. In these studies, V_P/V_S maps were produced by interpreting reflections on the same multicomponent data sets. Although the interpreters picked slightly different reflection events above and below the reservoir zone, it was interesting to see that the various maps were similar to the original map, despite the fact that slightly different reflection events were picked. Although consistency is no proof of correctness, the lithology boundaries on the various maps generally agreed with the core information from the 60 wells in the area. This interesting (and encouraging) mapping result caused us to analyze the robustness of this estimation method.

If the PP and PS sections contain zero-phase wavelets positioned at prominent separated reflectors, the traveltime intervals (isochrons) are relatively insensitive to spectral differences between wavelets. This can be seen by examining modeled seismic traces of Figure 5.1 (Zhang and Lines, 2006). Figure 5.1 compares traces with the same arrival times which contain Ricker wavelets (polarity reversed) with peak frequencies of 40 Hz and 20 Hz respectively. By picking the peaks of these wavelets, we note that traveltime picking of traces 1-10 (with 40 Hz Ricker wavelet) and traces 11-20 (with 20

Hz Ricker wavelet) both produce reflection events whose arrivals are at 100 ms and 150 ms respectively, giving isochron values of 50 ms on both sets of traces - despite the factor of 2 difference in the peak frequencies of the wavelets. If the significant reflectors in this analysis are separated by more than the tuning thickness, the traveltime method is very robust and not adversely affected by the peak frequencies of the wavelets. As the reflectors become more closely spaced, there will be greater tuning effects. It should be noted that synthetic seismograms obtained from dipole sonics in this field are very useful in identifying the appropriate reflectors on both the vertical and radial component seismograms.

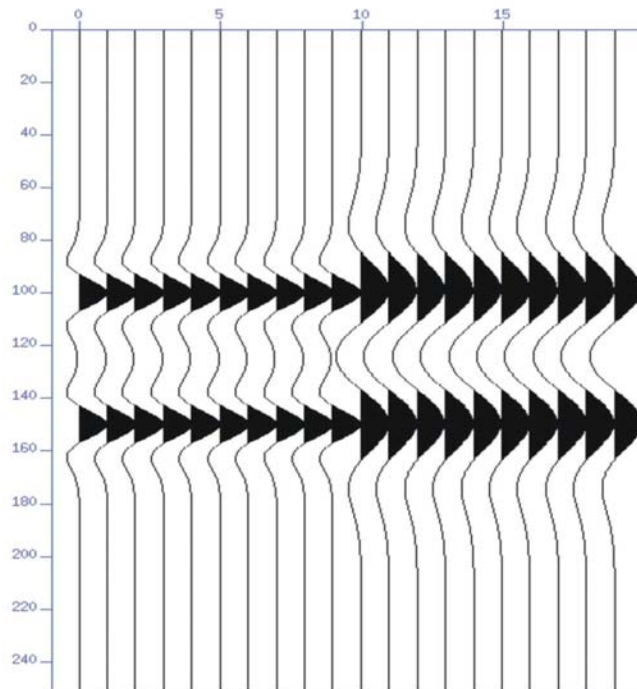


Figure 5.1: Robustness of traveltime picks for zero-phase wavelets with different spectral content. Traces 1-10 contains Ricker wavelets with peak frequencies of 40 Hz, and traces 11-20 contains Ricker wavelets with peak frequencies of 20 Hz. On both sets of traces, traveltime picks of the peaks produce isochron values of 50 ms, despite the difference in wavelet spectra. (Time scale is in samples, where 1 sample = 1 ms.) (Zhang and Lines, 2006).

It turns out that this traveltime method of V_P/V_S mapping for this particular area is reasonably robust, being relatively insensitive to the choice of reflectors or differences in the frequency content between the vertical and radial component. If the reflectors are too widely separated, there will be a degradation in vertical resolution of the target area; hence, we should generally attempt to find the strongest reflectors that are immediately above and below the target horizon. The frequency robustness of traveltime methods is fortunate, since for many multicomponent data sets, there is often a big difference between the frequency spectra of PP and PS seismic volumes. For target reflectors on the two seismic sections, the frequency band of PP spectrum is usually wider than that of the PS spectrum. With the dominant frequency of PP data usually being higher than for the PS data in this area, it might initially seem that these spectral differences could have a negative effect on the accuracy of calculated V_P/V_S ratios. However, if the wavelets in our data are consistently zero phase and the reflectors are distinctly separated, traveltime picks of peaks and troughs are relatively insensitive to spectral differences between data types.

In practice, it is often difficult to resolve reflections from the top and bottom of the target layer, especially for the PS seismic data. The reflected events from the top and bottom of the pay zone are often incoherent and difficult to pick. In such cases, we will have to select the reference horizons from above and below our target formation. If the interpreted interval between picked top and bottom horizons is thicker than the actual target layer, the calculated V_P/V_S will be smeared or affected by its surrounding layers if there are significant velocity contrasts between horizons. In such cases, the error of V_P/V_S from surrounding formations should be analyzed in order to implement the application of V_P/V_S correctly.

Although picking is relatively insensitive to spectral differences between components, I will show that bandpass filtering can provide some improvement to the quality of V_P/V_S maps. Then, through error analysis, I explain why this mapping procedure is very robust, thereby demonstrating that the V_P/V_S map is not overly sensitive to the choice of picking surrounding formations in this study area.

5.2 Interpretation of seismic data

To research the influence of foamy oil and wormholes on the physical properties, a vertical (PP) 3D data and a radial (PS) 3D data, from the Plover Lake field, were interpreted using Hampson-Russell software. More than 40 wells have already been drilled to develop heavy-oil in the area with about 8.2 km² (Figure 5.2). Detailed information is not available yet, but hands-on data is enough to give us a primary idea about the change of physical properties due to heavy-oil cold production. The 3D seismic data are composed of 145 in-lines and 282 cross-lines with bin size of 20X10 meters. Based on the interpretation of the top and bottom horizons of our target formation on both PP and PS 3D seismic data, we can calculate the V_P/V_S ratio of the target formation based on equation (5.1) to monitor the change of the V_P/V_S ratio induced by the heavy-oil cold production. Comparing the location of the drilled wells with the distribution of V_P/V_S map, we could probably find some correlation between them. If there is some discernible correlation between the change of the V_P/V_S ratio and the process of heavy-oil cold production in the real data, multicomponent seismic data will then be able to play a role to monitor the process of heavy oil cold production.

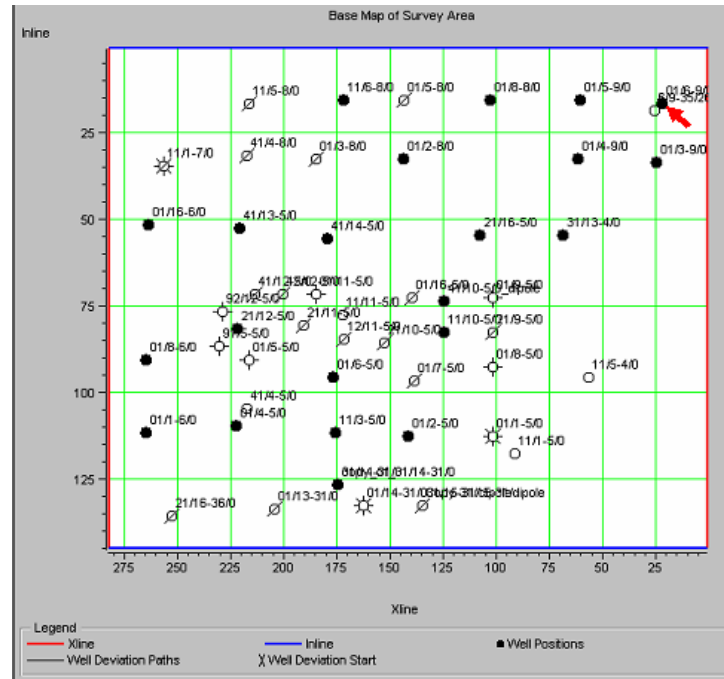


Figure 5.2: The basemap of project.

Firstly, the synthetic seismograms were created for both PP and PS seismic data based on the P-wave and S-wave sonic data from one in-situ well (Figure 5.3 and 5.4). The Bakken formation is the producing heavy-oil layer in this project and the thickness of the layer is about 20 meters. Generally, it's difficult to resolve reflections from the top and bottom of the target layer in the real seismic data, especially in the PS seismic data or the reflected events from the top and bottom of the pay zone are incoherent and difficult to pick. In this case, we will have to select the reference top and bottom horizons to pick, which surrounds our target formation. If the interpreted interval between picked top and bottom horizons is thicker than the actual target layer, the calculated V_P/V_S ratio will be smeared or affected by its surrounding layer. The error analysis will be discussed in the later part of this paper. On the other hand, the exactness and consistency of the picked reflections from the top and bottom of the layer in both PP and PS seismic data are the basis for the V_P/V_S ratio calculations. Finally, we should strike a balance between the

exactness of the interpreted horizons and the closeness of the picked horizons to the target formation. The criteria for selecting the reference top and bottom horizons are: (1) they should be coherent events across all over the seismic volume to guarantee exactness; (2) they should correspond to same reflecting geologic boundaries for both PP and PS data sets; (3) they should be as close as possible to the target formation to reduce the smearing effect.

According to above criteria, the final reference top and bottom horizons in both PP and PS synthetic seismograms were selected and they are plotted together in Figure 5.5, including P-wave and S-wave sonic log. In Figure 5.5, both PP and PS sections are displayed in PP time scale. The PS section was converted to the PP time scale according to the correlation of the corrected P-wave and S-wave sonic data after correlating both PP and PS synthetic seismograms with correspondent real seismic data. Actually, the PP section can be displayed in PS time scale either by similar conversion. From Figure 5.5, we can see that the selected reference horizons correspond with each other very well between PP and PS sections.

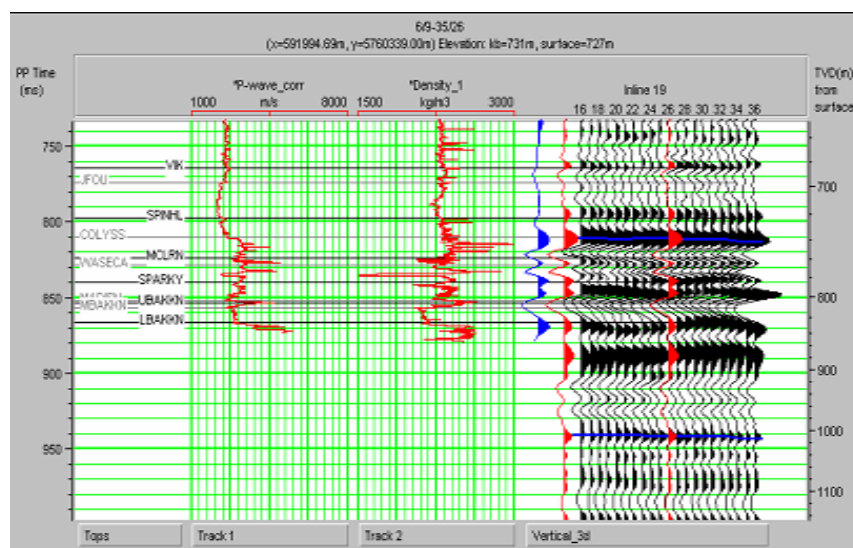


Figure 5.3: Synthetic seismogram for PP data

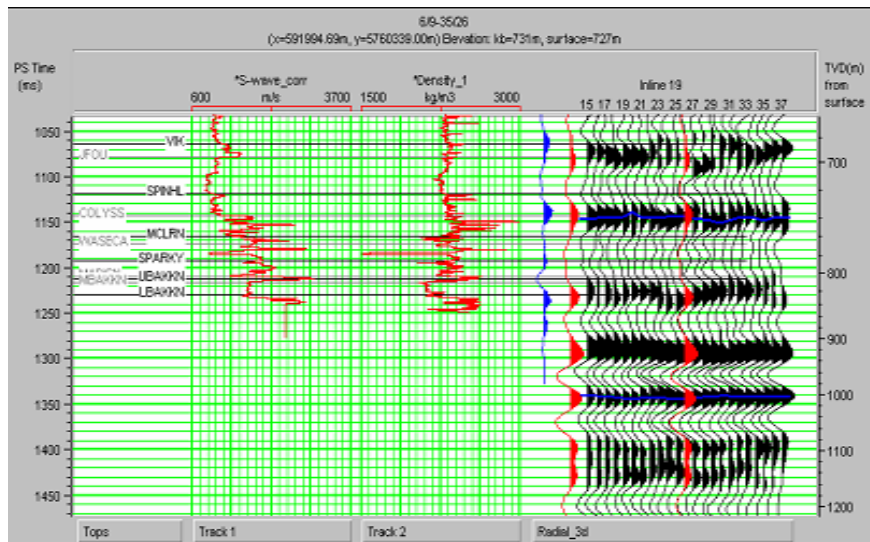


Figure 5.4: Synthetic seismogram for PS data

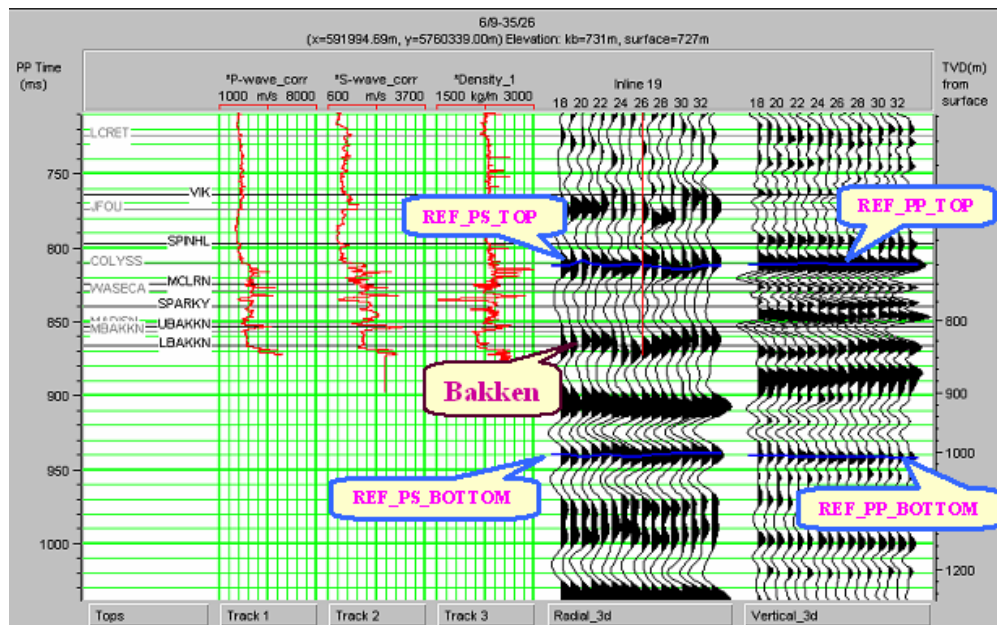


Figure 5.5: Selected reference top and bottom horizons.

5.3 Spectral differences between PP and PS seismic data

As previously mentioned, the frequency spectra of the PP and PS seismic volumes in the depth of our target formation are often quite different. Figure 5.6 shows typical amplitude spectra for wavelets extracted from PP and PS seismic data at Plover Lake.

The frequency band of the PP spectrum is wider than that of the PS spectrum and the dominant frequency of PP data is usually much higher.

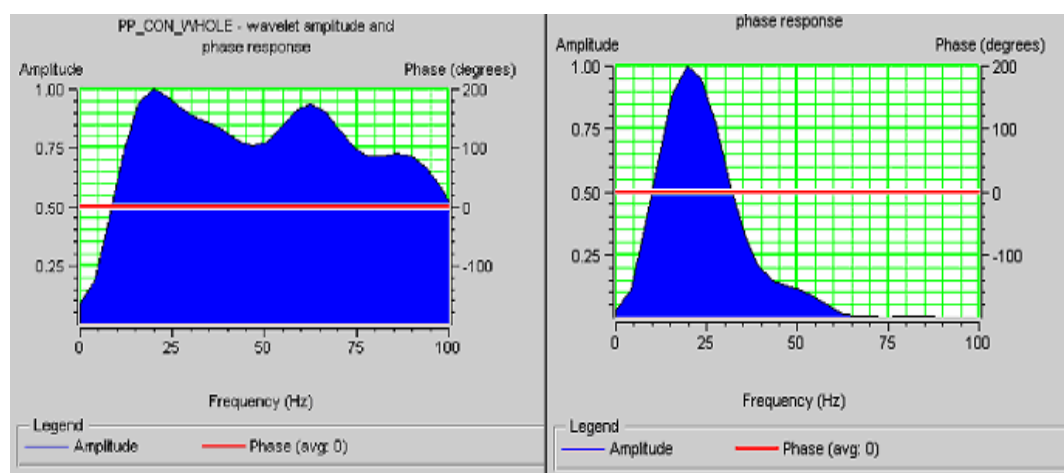


Figure 5.6: Amplitude spectra of wavelets extracted from PP (left) and PS (right) seismic data at Plover Lake field.

To reduce the problem of spectral differences, I applied a low-pass filter to the PP seismic data to the same bandwidth as the PS data. We designed a bandpass filter (0, 10, 30, 55Hz) based on the amplitude spectrum of PS seismic volume, which has a narrower frequency band and a lower dominant frequency, and applied the designed band pass filter to PP seismic data, which has a wider frequency band and higher dominant frequency. (Another possibility for matching frequencies between the PP and PS data could involve the use of matched filters instead of bandpass filtering, although the authors have not yet tested this procedure.) Comparing unfiltered PP data with filtered PP data (Figure 5.7), we can see the differences of reflection-event character between them. For the top reference horizon, we note that two closely distributed events with higher frequency on the unfiltered PP data merged into one event with lower frequency on filtered PP data. (For easier event correlation, the seismic sections on the left side of Figures 5.7, 5.8 and 5.9 are plotted in reversed direction to those on the right side.) From

Figures 5.8 and 5.9, we can clearly see that the similarity between PP and PS data is improved after application of band pass filter on PP data, especially for the selected reference top horizon.

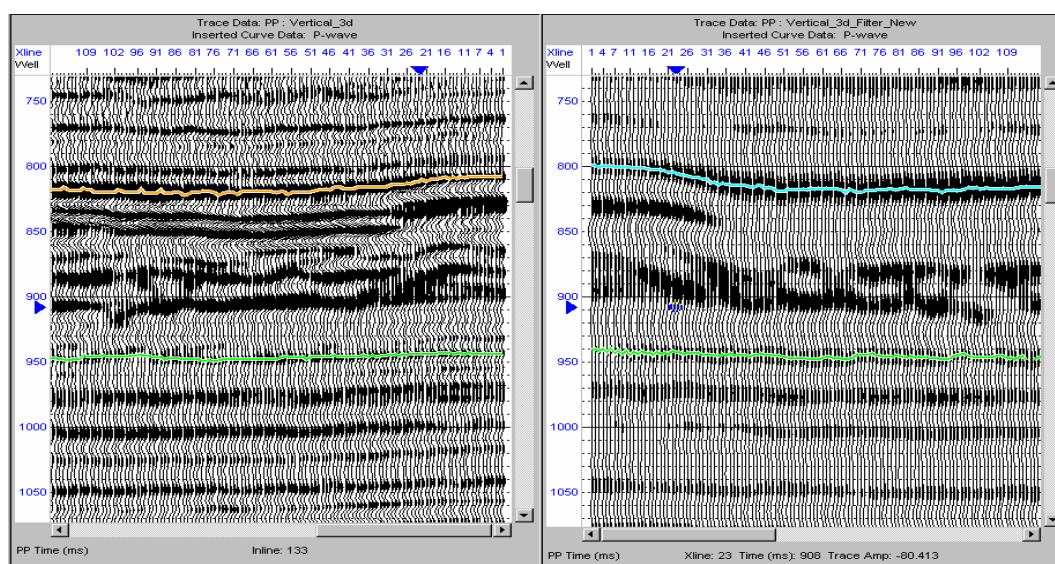


Figure 5.7: Comparison between unfiltered PP (left) and filtered PP (right) seismic data (Line on left is plots traces 116-1 and line on the right plots traces 1-116).

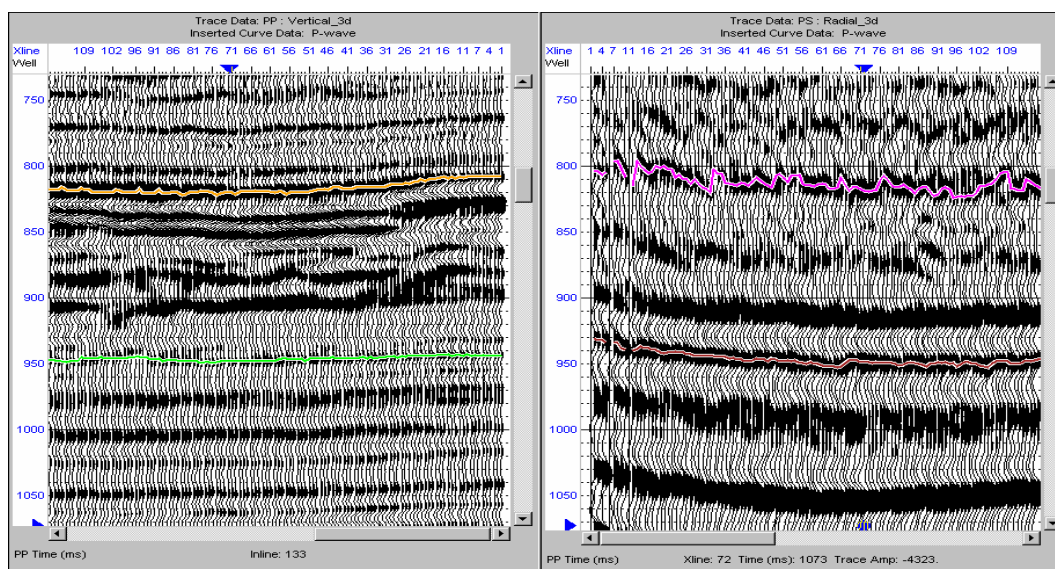


Figure 5.8: Comparison between unfiltered PP (left) and PS (right) seismic data. The frequency content of the PP section is much higher than the corresponding PS section.

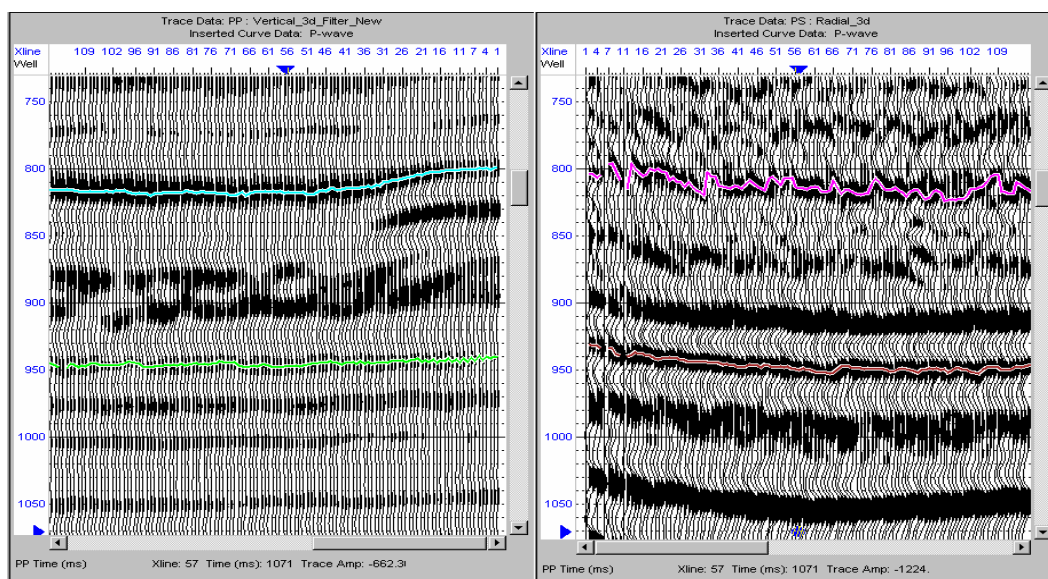


Figure 5.9: Comparison between filtered PP (left) and PS (right) seismic data shows a better correlation of reflecting events than in Figure 5.8.

The difference of the picked top references between the unfiltered and filtered PP data is shown in Figure 5.10. The actual difference between picked events (due to the wavelet differences) is not so prominent - being only a few milliseconds difference, but this will have an effect on the final V_P/V_S maps.

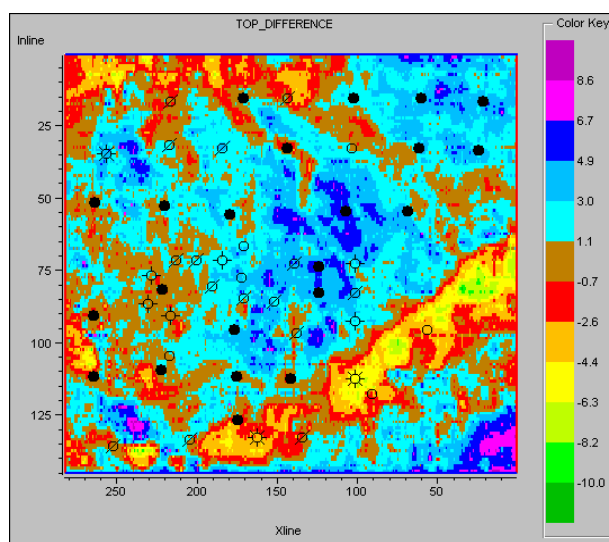


Figure 5.10: Difference of top horizons between unfiltered and filtered PP seismic data.

Figures 5.11 and 5.12 are the final maps of V_P/V_S between the interpreted reference top and bottom horizons for unfiltered and filtered data. Yellow, orange and red colors show zones of lower V_P/V_S values. Based on our experience with heavy-oil fields in Western Canada, such zones correspond with sand thickening and/or zones affected by heavy-oil production (as described by Watson et al., 2002; Lines et al., 2003; Chen et al., 2003). Generally speaking these maps allow us to detect thickening sand with the initial base survey, whereas we would use time-lapse seismic monitoring to detect reservoir changes.

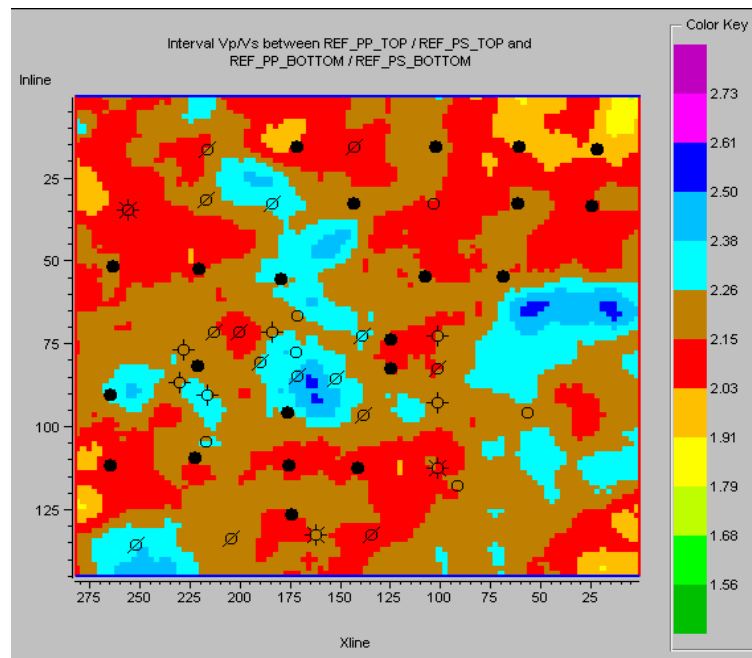


Figure 5.11: V_P/V_S between top and bottom horizons from unfiltered PP and PS data.

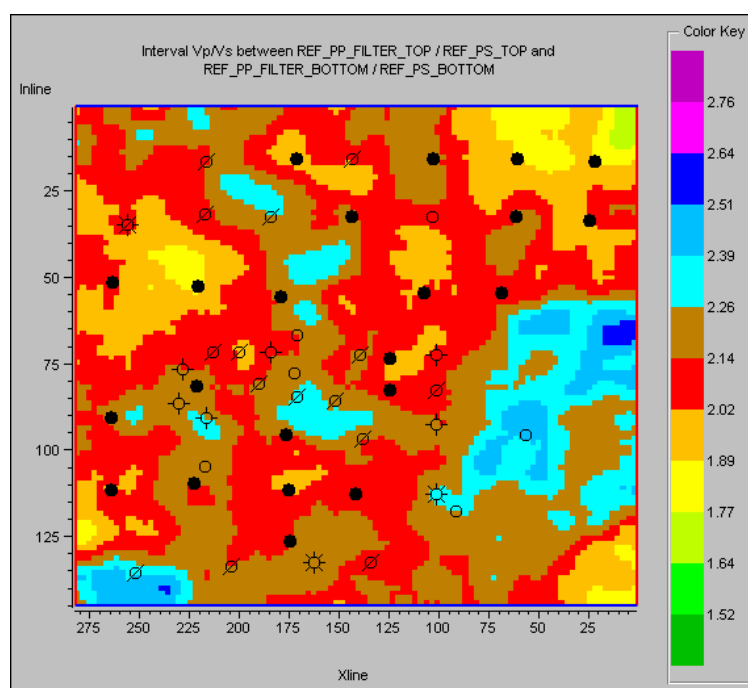


Figure 5.12: V_p/V_s between top and bottom horizons from filtered PP and PS data.

In Figures 5.11 and 5.12, the values of V_p/V_s around production wells are generally lower than elsewhere. The lower values of V_p/V_s have a good correspondence with well locations on both maps, but the map in Figure 5.12 from filtered PP and PS data has better correspondence with the well data especially in the west-center part. Although our somewhat simplistic initial analysis suggested that the mapping is not overly sensitive to differences in wavelet spectra (Figure 5.1), the comparisons of maps in Figures 5.11 and 5.12 suggests that it is worthwhile to apply bandpass filtering of the seismic volume to enhance the similarity between PP and PS seismic volumes.

It is interesting that the map in Figure 5.12 is very similar to the maps obtained by Lines et al. (2005) in which we see slightly different events both above and below the reservoir layer, with the principal difference being that the deeper reference horizon was at about 950 ms in this paper and at 1000 ms in Lines et al. (2005). This similarity of

V_P/V_S maps suggests that this mapping method is very robust. We now investigate this robustness by error analysis.

Before proceeding to error analysis, let's see some interesting results concluded from the isochron maps (Figures 5.13 and 5.14). According to the colour legends in these maps, the value of the isochron map from PP data varies between 143 ms and 115 ms, giving a variation of 28 ms; meanwhile, the value from PS data varies from 211 to 193 ms, giving a variation of 18 ms. This means that S-wave travels a longer time in the interpreted interval, but there is less lateral variation of travel time (isochron value) compared with P-wave (Figure 5.15). In Figure 5.15, the lateral variation of one-way traveltime for P-wave is 14 ms, while the lateral variation of one-way traveltime for S-wave is 4 ms. In other word, the velocity of P-wave is more sensitive to the environment than S-wave. That is the reason why the pattern of the isochron map from PP data is more colorful than that from PS data. Based on this result, we can make a conclusion that the velocity of the S-wave shows less variation laterally if the lithology of the interpreted layer doesn't change much. This conclusion further reveals that the shear modulus of heavy oil doesn't play a detectable role before and after production, Gassmann's equation is still suitable.

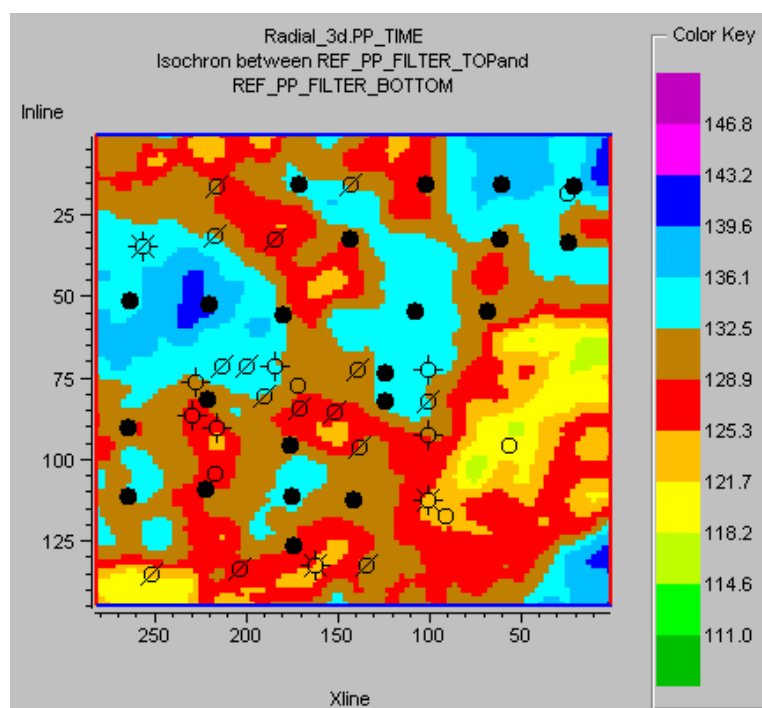


Figure 5.13: Isochron map between top and bottom horizons from filtered PP data

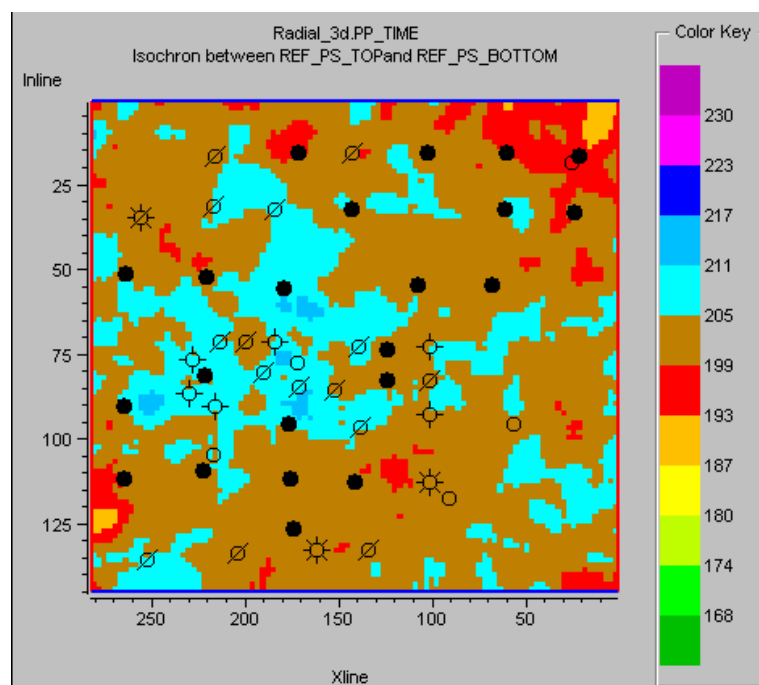


Figure 5.14: Isochron map between top and bottom horizons from PS data

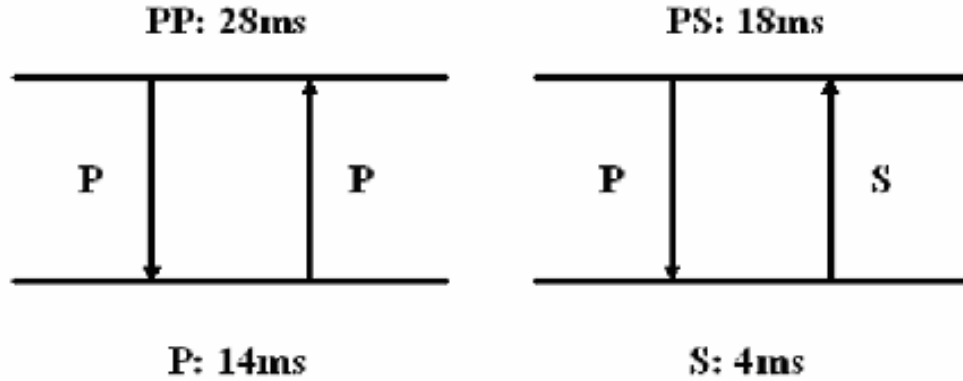


Figure 5.15: Comparing results from Figures 5.13 and 5.14. The lateral variations of P-wave and S-wave traveltimes are denoted.

5.4 Error analysis

In this analysis, we examine the mapping errors introduced by picking reflectors that are slightly above and below the target horizon. The Figure 5.16 is a sketch of the interpreted model of PP and PS data, where V_{P1} , V_P , and V_{P2} are P-wave velocities of surrounding (above-target), target, and surrounding (below-target) formations, V_{S1} , V_S , and V_{S2} are S-wave velocities of surrounding and target formations, Δt_{PP1} , Δt_{PP} and Δt_{PP2} are interpreted traveltimes of surrounding and target formations from PP seismic data, Δt_{PS1} , Δt_{PS} and Δt_{PS2} are interpreted travel times of surrounding and target formations from PS seismic data, Δd_1 , Δd and Δd_2 are the thickness of surrounding and target formations. We also assume that the total traveltime interval for PS data is $\Delta T_{PS} = \Delta t_{PS1} + \Delta t_{PS} + \Delta t_{PS2}$, and that the total traveltime for PP data is $\Delta T_{PP} = \Delta t_{PP1} + \Delta t_{PP} + \Delta t_{PP2}$. We set $C_{S1} = \Delta t_{PS1} / \Delta t_{PS}$, $C_{S2} = \Delta t_{PS2} / \Delta t_{PS}$, $C_{P1} = \Delta t_{PP1} / \Delta t_{PP}$, $C_{P2} = \Delta t_{PP2} / \Delta t_{PP}$, $r_1 = V_{P1} / V_{S1}$, $r = V_P / V_S$, $r_2 = V_{P2} / V_{S2}$. V_P^* is the average velocity of the P-wave between the interpreted interval and V_S^* is the average velocity of the S-wave between the interpreted interval, then the ratio of V_P^* and V_S^* can be expressed as:

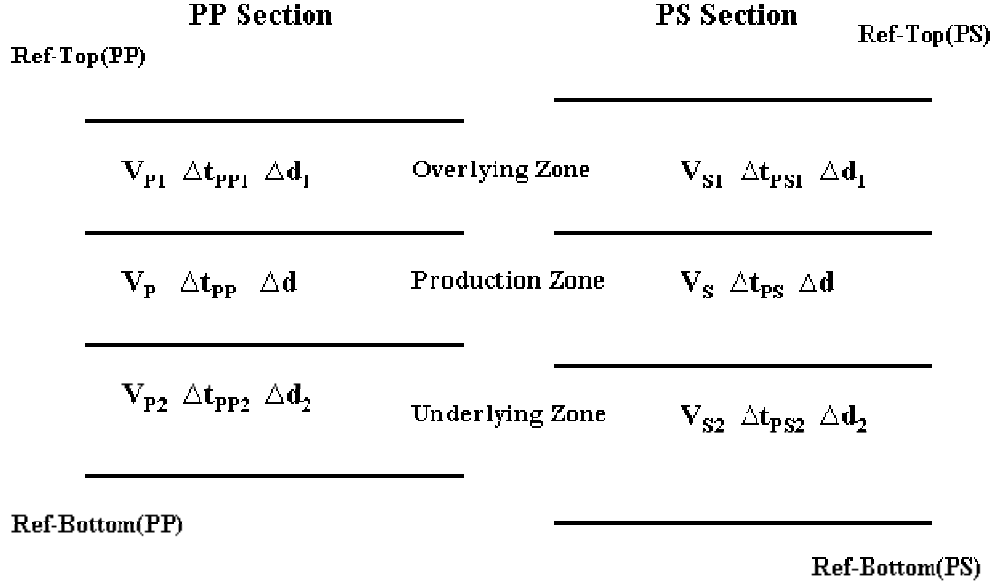


Figure 5.16: The sketch of the interpreted model.

$$\begin{aligned}
 R &= \frac{V_P^*}{V_S^*} = \frac{2\Delta T_{PS}}{\Delta T_{PP}} - 1 = \frac{2(\Delta t_{PS1} + \Delta t_{PS} + \Delta t_{PS2})}{\Delta t_{PP1} + \Delta t_{PP} + \Delta t_{PP2}} - 1 \\
 &= \frac{2(C_{S1}\Delta t_{PS} + \Delta t_{PS} + C_{S2}\Delta t_{PS})}{C_{P1}\Delta t_{PP} + \Delta t_{PP} + C_{P2}\Delta t_{PP}} - 1 \\
 &= \frac{2(C_{S1} + C_{S2} + 1)\Delta t_{PS}}{(C_{P1} + C_{P2} + 1)\Delta t_{PP}} - 1 \\
 &= \frac{C_{S1} + C_{S2} + 1}{C_{P1} + C_{P2} + 1} \left[\frac{2\Delta t_{PS}}{\Delta t_{PP}} - 1 + 1 - \frac{C_{P1} + C_{P2} + 1}{C_{S1} + C_{S2} + 1} \right] \\
 &= \frac{C_{S1} + C_{S2} + 1}{C_{P1} + C_{P2} + 1} \left[\frac{V_P}{V_S} + \frac{C_{S1} + C_{S2} - (C_{P1} + C_{P2})}{C_{S1} + C_{S2} + 1} \right] \\
 &= \frac{C_{S1} + C_{S2} + 1}{C_{P1} + C_{P2} + 1} \frac{V_P}{V_S} + \frac{C_{S1} + C_{S2} - (C_{P1} + C_{P2})}{C_{P1} + C_{P2} + 1}
 \end{aligned}$$

Since

$$C_{P1} = \frac{\Delta t_{PP1}}{\Delta t_{PP}} = \frac{\frac{\Delta d_1}{V_{P1}} + \frac{\Delta d_1}{V_{P1}}}{\frac{\Delta d}{V_P} + \frac{\Delta d}{V_P}} = \frac{\Delta d_1}{\Delta d} \cdot \frac{V_P}{V_{P1}}$$

$$C_{S1} = \frac{\Delta t_{PS1}}{\Delta t_{PS}} = \frac{\frac{\Delta d_1}{V_{P1}} + \frac{\Delta d_1}{V_{S1}}}{\frac{\Delta d}{V_P} + \frac{\Delta d}{V_S}} = \frac{\Delta d_1}{\Delta d} \cdot \frac{V_P V_S (V_{P1} + V_{S1})}{V_{P1} V_{S1} (V_P + V_S)}$$

$$= \frac{\Delta d_1}{\Delta d} \cdot \frac{V_P}{V_{P1}} \cdot \frac{\frac{V_{S1}}{V_P} + 1}{\frac{V_P}{V_S} + 1} = C_{P1} \frac{r_1 + 1}{r + 1}$$

Similarly

$$C_{S2} = C_{P2} \frac{r_2 + 1}{r + 1}$$

and then:

$$R = \frac{\frac{r_1 + 1}{r + 1} C_{P1} + \frac{r_2 + 1}{r + 1} C_{P2} + 1}{C_{P1} + C_{P2} + 1} \cdot \frac{V_P}{V_S} + \frac{\frac{r_1 + 1}{r + 1} C_{P1} + \frac{r_2 + 1}{r + 1} C_{P2} - (C_{P1} + C_{P2})}{C_{P1} + C_{P2} + 1}$$

If $r_1 \approx r_2 \approx 2$, then:

$$R \approx \frac{\frac{3}{r+1} C_{P1} + \frac{3}{r+1} C_{P2} + 1}{C_{P1} + C_{P2} + 1} r + \frac{\frac{3}{r+1} C_{P1} + \frac{3}{r+1} C_{P2} - (C_{P1} + C_{P2})}{C_{P1} + C_{P2} + 1}$$

$$= \frac{\frac{3}{r+1} (C_{P1} + C_{P2} + 1) + \frac{r-2}{r+1}}{C_{P1} + C_{P2} + 1} r + \frac{(C_{P1} + C_{P2}) \frac{2-r}{r+1}}{C_{P1} + C_{P2} + 1}$$

$$= \left(\frac{3}{r+1} + \frac{r-2}{r+1} \cdot \frac{1}{C_{P1} + C_{P2} + 1} \right) r + \frac{(C_{P1} + C_{P2} + 1) \frac{2-r}{r+1} - \frac{2-r}{r+1}}{C_{P1} + C_{P2} + 1}$$

$$\begin{aligned}
&= \frac{3r}{r+1} + \frac{2-r}{r+1} + \frac{1}{C_{P1} + C_{P2} + 1} \left[\frac{(r-2)r}{r+1} + \frac{r-2}{r+1} \right] \\
&= 2 + \frac{1}{C_{P1} + C_{P2} + 1} \cdot \frac{r^2 - r - 2}{r+1} = 2 + \frac{r-2}{C_{P1} + C_{P2} + 1} .
\end{aligned}$$

If, $\Delta d_1 \approx \Delta d_2 \approx \Delta d$, then:

$$R \approx 2 + \frac{r-2}{\frac{V_P}{V_{P1}} + \frac{V_P}{V_{P2}} + 1} . \quad (5.2)$$

If $V_{P1} \approx V_{P2}$ and $r_p = V_P/V_{P1}$, the error will be:

$$E = R - r \approx (2-r) \frac{2r_p}{2r_p + 1} . \quad (5.3)$$

The equation of error can be divided into two factors: one is $(2-r)$, another is $2r_p/(2r_p+1)$. The first factor represents the difference in the V_P/V_S ratios between the production zone and surrounding layers (above and below the production zone), since our assumption was that $r_1 \approx r_2 \approx 2.0$. The second factor is the coefficient containing r_p , the ratio of the P-wave velocity in the production zone to the value in the surrounding zone. Since both r and r_p vary laterally, the error will laterally vary.

In order to examine the error analysis for a simple example, we generate Table 5.1 of the case where: $V_{P1} \approx V_{P2} \approx 3000$ m/s, and $V_S \approx V_{S1} \approx V_{S2} \approx 1500$ m/s (since velocity of S-wave doesn't change dramatically due to production we set all shear wave velocities to be equal). Based on the above two equations of R and E , the following results are generated for different values of V_P of the target horizon (Table 5.1).

As expected, we note that the estimated values, V_P^*/V_S^* , are close to the actual values V_P/V_S , whenever the P-wave velocity of the target zone is close to the value of the

surrounding zone. Otherwise stated, the error will increase with the increasing velocity difference between the production zone and surrounding zone. We can also conclude that: if V_{P1}/V_{S1} and V_{P2}/V_{S2} don't change laterally, R will have a similar pattern to that of the ratio r of the production zone (Figure 5.17). However, if V_{P1}/V_{S1} and V_{P2}/V_{S2} change dramatically laterally, then R will probably reach a different pattern compared with r . Thus, if possible, we should interpret the strongest reference horizons as close as possible to the top and bottom of the production zone to keep the effects of the surrounding zones to a minimum.

Table 5.1: The result of error analysis.

V_P	$(V_{P1}-V_P)/V_{P1}$	V_P/V_S	V_P^*/V_S^*	E
2000	0.333	1.333	1.714	0.381
2100	0.300	1.400	1.750	0.350
2200	0.267	1.467	1.784	0.317
2300	0.233	1.533	1.816	0.282
2400	0.200	1.600	1.846	0.246
2500	0.167	1.667	1.875	0.208
2600	0.133	1.733	1.902	0.169
2700	0.100	1.800	1.929	0.129
2800	0.067	1.867	1.953	0.087
2900	0.033	1.933	1.977	0.044
3000	0.000	2.000	2.000	0.000

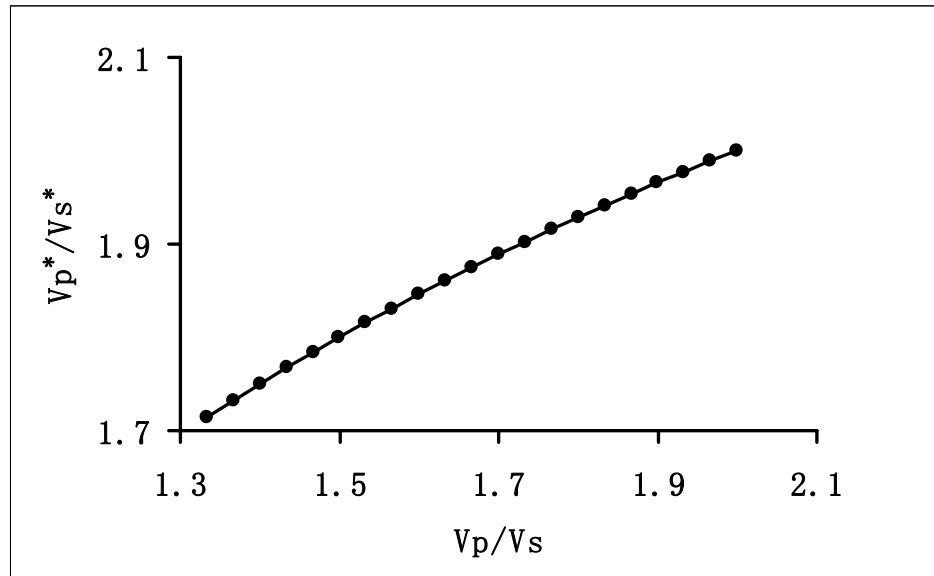


Figure 5.17: Calculated velocity ratio (V_P^*/V_S^*) versus real velocity ratio (V_P/V_S).

In most cases, the production formation is overlain and underlain by formations with the lithology of shale, which acts as seal or resource, or both. Shale is usually deposited in a deep water environment and the seismic velocity in shale layers shows little lateral variation. Figure 5.18 is the impedance inversion result from PP seismic volume, which shows that overlying and underlying formations are relatively stable compared with target formation. Moreover, the reflection events from shaly formation are usually coherent, meaning that they are good candidates for reference horizons. Both of the above facts provide a good condition for us to get a calculated V_P^*/V_S^* map from interpreted intervals, which will have a similar pattern with the V_P/V_S map of target formation.

On the other hand, if the velocities of overlying and underlying formations have a lateral dramatic change due to faulting or a changing depositional environment, we need to analyze the pattern of calculated V_P^*/V_S^* in a restricted area, where the velocities of

surrounding formations are relatively stable, so as to improve the reliability of this method.

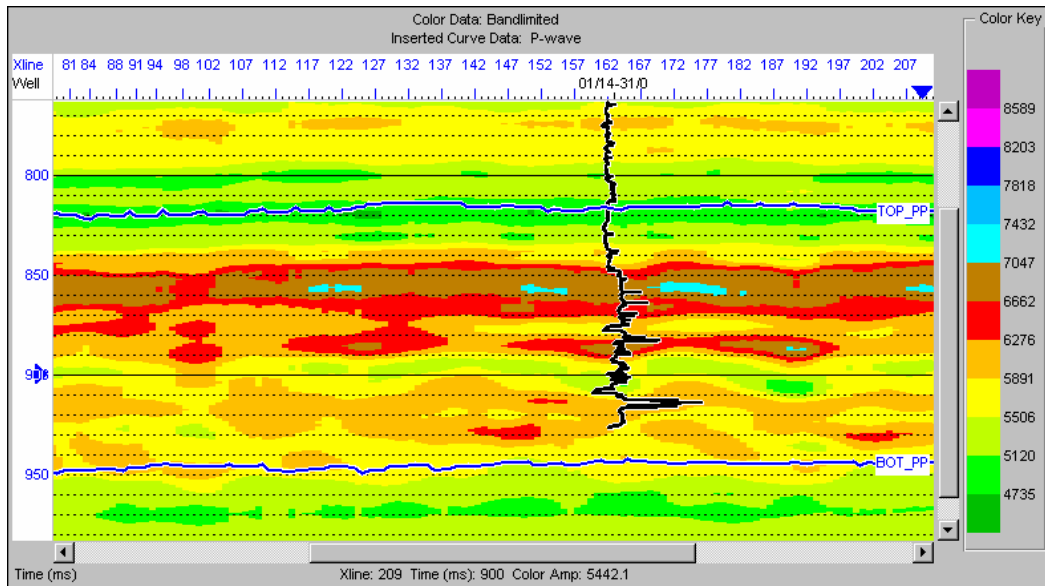


Figure 5.18: The impedance inversion result from PP seismic volume.

CHAPTER 6

THE FEASIBILITY OF AVO ANALYSIS FOR MONITORING HEAVY OIL COLD PRODUCTION

6.1 Effect of the V_p/V_s ratio on the AVO response

If the V_p/V_s ratio of average background is 2.0, and the higher-order term that becomes effective beyond incident angles of 30° is dropped, the Shuey's linear approximation equation of Zoeppritz's equation can be further simplified as (Verm and Hilterman, 1995):

$$R(\theta) \approx R_p \cos^2 \theta + \frac{\sigma_2 - \sigma_1}{(1 - \sigma_{avg})^2} \sin^2 \theta \quad , \quad (6.1)$$

where R is P-wave reflection coefficient, θ is P-wave incidental angle, R_p is normal P-wave reflection coefficient, σ_2 and σ_1 are Poisson's ratios of the underlying medium and the incident medium, σ_{avg} is the average of σ_2 and σ_1 . Equation (6.1) shows that AVO response has a close relationship with the variation of Poisson's ratios.

For an isotropic elastic medium, Poisson's ratio is simply related to V_p/V_s ratio:

$$\sigma = \frac{\frac{1}{2} \left(\frac{V_p}{V_s} \right)^2 - 1}{\left(\frac{V_p}{V_s} \right)^2 - 1} \quad . \quad (6.2)$$

This equation indicates that Poisson's ratio may be determined dynamically using field or laboratory measurements of both V_p and V_s . Figure 6.1 more clearly displays the dependence of Poisson's ratio σ on the V_p/V_s ratio. σ will decrease too with the decreasing

V_p/V_s ratio.

Koefoed (1955) made several observations on the effect of Poisson's ratio of rock strata on the reflection coefficient of plane waves, and most of his observations can be obtained from equation (6.1). For the lower P-wave velocity of the underlying medium, R_p is negative. If $\sigma_2 \approx \sigma_1$, the second term will be zero. If there is an decrease of Poisson's ratio (σ_2) for the underlying medium due to the reduction of V_p/V_s ratio after heavy oil cold production, $(\sigma_2 - \sigma_1)/(1 - \sigma_{avg})^2$ will become negative, not zero any more, the reflection coefficient R will absolutely be changed at the non-zero angles of incidence.

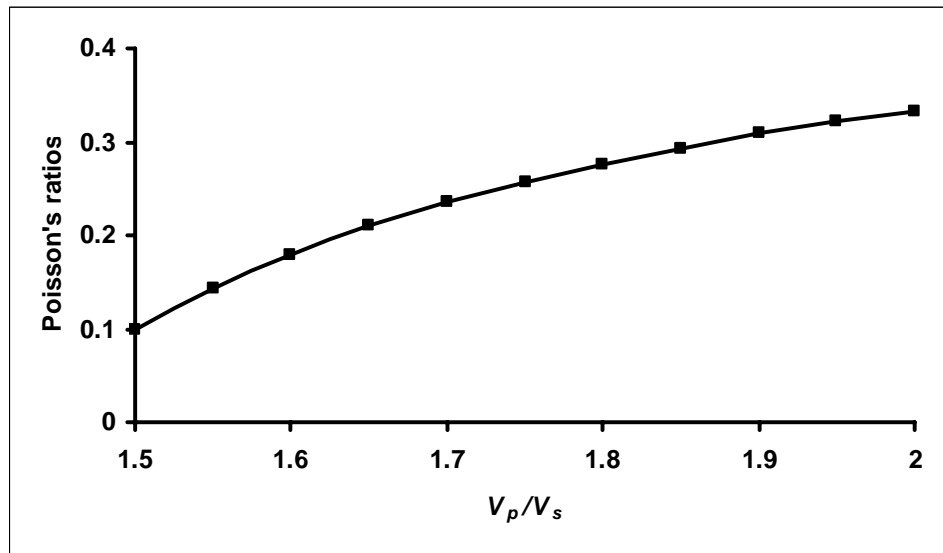


Figure 6.1: The dependence of Poisson's ratio σ on V_p/V_s ratio

For the in-situ case, the estimated physical properties from well log data for the researched well are listed in Table 6.1, and the variation of P-wave reflection coefficients with the increasing incidental angles is shown in Figure 6.2. If the Poisson's ratio of the underlying medium is decreased to 0.28 from 0.32 after heavy oil cold production, and other properties don't change, then the variation of P-wave reflection coefficients with

the increasing incidental angles is changed and shown in Figure 6.3, together with the result in Figure 6.2. These two curves reveal that the decreasing Poisson's ratio will create a quite different AVO response with a lower slope. Actually, when Poisson's ratio decreases for the underlying medium due to heavy oil cold production, P-wave velocity will decrease too, R_p will become more negative and the two curves will be separated from zero incidental angle. This will be shown in the later fluid substitution part.

Table 6.1: Estimated physical properties from well log data.

Parameters	P-wave velocity (m/s)	Density (g/cc)	Poisson's ratio
Incidental medium	4500	2.45	0.38
Underlying medium	3100	2.13	0.32

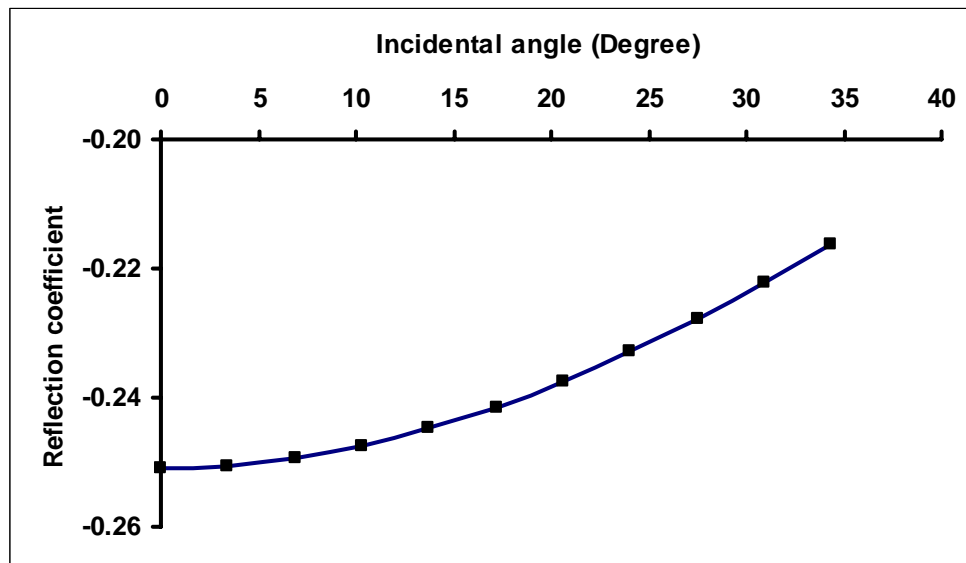


Figure 6.2: P-wave reflection coefficients before production

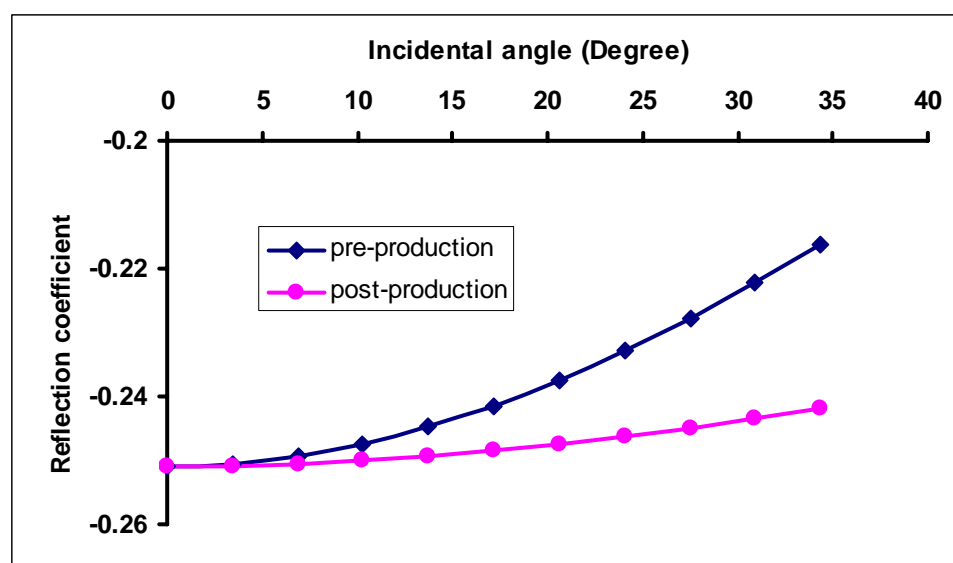


Figure 6.3: Comparison of P-wave reflection coefficients between pre- and post-production.

6.2 Fluid substitution for heavy oil cold production using S-wave sonic log data

In most cases, well log data is acquired just after the well is drilled and before production, the well log data for post-production is usually not available. To analyze the difference of AVO responses between pre- and post-production, even the wet case, we need to predict the well logs data for post-production, including the wet case.

The basic problem of fluid substitution can be generalized as: given well log data in certain cases, derive well logs data at other cases, for example, at different hydrocarbons and water saturation, and even different porosities.

Gassmann's (1951) equation (3.1) has been used for calculating the effect of fluid substitution on seismic properties using the frame properties. It calculates the bulk modulus of a fluid saturated porous medium using the known bulk moduli of the solid matrix, the frame, and the pore fluid. Finally, equations (3.3) and (3.4) are used to

calculate new P-wave and S-wave velocities for AVO modeling, equation (3.5) is used to calculate new density. In this process, the shear modulus is assumed to be independent of fluids, densities and moduli of matrix are assumed to be known, densities and bulk moduli of water and hydrocarbons are calculated based on Batzle-Wang formulas (1992).

Generally, before doing fluid substitution, we know following parameters for pre-production condition:

V_p^{pre} : P-wave velocity from well log data;

V_s^{pre} : S-wave velocity from well log data;

ρ^{pre} : density from well log data;

S_w^{pre} : water saturation (25% for the in-situ case);

S_o^{pre} : heavy oil saturation (75% for the in-situ case);

ρ_w^{pre} : density of water from Batzle-Wang formulas (1.01 g/cc for the in-situ case);

K_w^{pre} : bulk modulus of water from Batzle-Wang formulas (2.37 GPa for the in-situ case);

ρ_o^{pre} : density of heavy oil from Batzle-Wang formulas (0.97 g/cc for the in-situ case);

K_o^{pre} : bulk modulus of heavy oil from Batzle-Wang formulas (2.2166 GPa for the in-situ case);

ρ_m : density of matrix sandstone (2.65 g/cc);

K_m : bulk modulus of matrix sandstone from Han et al.,2004 (39 GPa);

μ_m : shear modulus of matrix sandstone from Han et al.,2004 (27 GPa).

The reservoir parameters are listed in Table 4.1 to calculate fluids properties based on Batzle-Wang formulas (1992). From these fluids properties and reservoir parameters, we have calculated bulk modulus of fluids mixture ($K_f^{pre}=2.254$ GPa) saturated in rock's pore in Chapter 4, and density of fluids mixture is:

$$\begin{aligned}\rho_f^{pre} &= S_w^{pre} \rho_w^{pre} + S_o^{pre} \rho_o^{pre} \\ &= 0.25 \times 1.01 + 0.75 \times 0.97 = 0.98 \text{ (g/cc)} .\end{aligned}\quad (6.3)$$

Now, it's time to calculate porosity from various densities:

$$\phi^{pre} = \frac{\rho_f^{pre} - \rho_m}{\rho_f^{pre} - \rho_m} . \quad (6.4)$$

The above calculated porosity ϕ^{pre} is the original porosity. After production, the reservoir porosity will be increased due to the simultaneous extraction of sand with heavy oil production. Recently, we don't have the data to calculate the new porosity yet, but we can assume the new porosity ϕ^{post} equals a larger value, saying 35%, which will assist us to do qualitative analysis.

In the reservoir condition of pressure depletion after heavy oil cold production, dissolved gas in live heavy oil comes out of solution as bubbles and is trapped within heavy oil. Both of heavy oil and trapped gas bubbles together create the foamy oil, which is a foamy or emulsive state. According to the reservoir parameters listed in Table 4.1, densities and bulk moduli of fluids are calculated for post-production condition based on Batzle-Wang formulas (1992):

ρ_w^{post} : density of water (1.0088 g/cc);

K_w^{post} : bulk modulus of water (2.34 GPa);

ρ_o^{post} : density of heavy oil (0.97 g/cc);

K_o^{post} : bulk modulus of heavy oil (0.0636 GPa);

ρ_g^{post} : density of gas (0.004 g/cc);

K_g^{post} : bulk modulus of gas (0.0008 GPa).

Also, Table 4.1 tells us saturation of fluids after heavy oil cold production:

S_w^{post} : water saturation (19%);

S_o^{post} : heavy oil saturation (62%);

S_g^{post} : gas saturation (19%).

Now, we can calculate density and bulk modulus of foamy oil (mixture of heavy oil and gas):

$$\begin{aligned}\rho_{o-g}^{post} &= \frac{S_o^{post}}{S_o^{post} + S_g^{post}} \rho_o^{post} + \frac{S_g^{post}}{S_o^{post} + S_g^{post}} \rho_g^{post} \\ &= \frac{0.62}{0.62 + 0.19} \times 0.97 + \frac{0.19}{0.62 + 0.19} \times 0.004 \\ &= 0.7424 + 0.0009384 \approx 0.743 \text{ (g/cc)} .\end{aligned}$$

Bulk modulus of foamy oil is calculated as the average of Voigt and Reuss averages of fluids moduli:

$$\begin{aligned}K_{o-g}^{post} &= \frac{1}{2} (K_{o-g}^{post(V)} + K_{o-g}^{post(R)}) \\ &= \frac{1}{2} (0.0489 + 0.003276) \approx 0.026 \text{ (GPa)} .\end{aligned}$$

Actually, the required parameters are well prepared right now, and what we will

have to do next is to do fluid substitution based on Gassmann's equation, together with other equations described in Chapter 3 and derived in the following context.

Firstly, from above fluids properties, bulk modulus of fluids mixture saturated in rock's pore was calculated in Chapter 4 ($K_f^{post} \approx 0.244$ GPa), and density of fluids mixture is:

$$\begin{aligned}\rho_f^{post} &= S_w^{post} \rho_w^{post} + S_o^{post} \rho_o^{post} + S_g^{post} \rho_g^{post} \\ &= 0.19 \times 1.0088 + 0.62 \times 0.97 + 0.19 \times 0.004 \\ &= 0.1924 + 0.6014 = 0.7938 \text{ (g/cc) ,}\end{aligned}$$

and total average density of fluids and rock matrix after production is:

$$\begin{aligned}\rho^{post} &= \phi^{post} \rho_f^{post} + (1 - \phi^{post}) \rho_m \\ &= 0.35 \times 0.7938 + 0.65 \times 2.65 \\ &= 0.278 + 1.723 = 2.001 \text{ (g/cc) .}\end{aligned}$$

Also, from equations (3.3) and (3.4), we can derive following equations to calculate saturated bulk modulus (K_{pre}^*) and saturated shear modulus (μ_{pre}^*) from well logs data:

$$\mu_{pre}^* = \rho^{pre} (V_s^{pre})^2 \text{ ,} \quad (6.5)$$

$$K_{pre}^* = \rho^{pre} (V_p^{pre})^2 - \frac{4}{3} \mu_{pre}^* \text{ .} \quad (6.6)$$

If

$$a = \frac{K_{pre}^*}{K_m - K_{pre}^*} - \frac{K_f^{pre}}{\phi^{pre} (K_m - K_f^{pre})} \text{ ,}$$

from Gassmann's equation (3.1), there is:

$$K_d^{pre} = \frac{a}{1+a} K_m \text{ ,} \quad (6.7)$$

where, K_d^{pre} is frame bulk modulus for pre-production. If there is no change in porosity, which is the case of thermal production, then:

$$K_d^{post} = K_d^{pre} \quad , \quad (6.8)$$

$$\mu_d^{post} = \mu_d^{pre} = \mu_{pre}^* \quad , \quad (6.9)$$

otherwise:

$$\frac{1}{K_d^{post}} = \frac{\phi^{post}}{K_\phi} + \frac{1}{K_m} \quad , \quad (6.10)$$

$$\mu_d^{post} = \mu_m (1 - \phi^{post} / \phi_c) \quad , \quad (6.11)$$

where K_ϕ^{-1} is the effective dry rock pore space compressibility, defined as the ratio of the fractional change in pore volume to an increment of applied external hydrostatic stress at constant pore pressure (Mavko et al., 1995), ϕ_c is critical porosity, K_d^{post} and μ_d^{post} are frame bulk and shear moduli for post-production. Equation (6.10) is effective for pre-production too,

$$\frac{\phi^{pre}}{K_\phi} = \frac{1}{K_d^{pre}} - \frac{1}{K_m} \quad , \quad (6.12)$$

Substitute equation (6.12) into equation (6.10), K_d^{post} can be got from K_d^{pre} :

$$\frac{1}{K_d^{post}} = \frac{1}{K_m} + \frac{\phi^{post}}{\phi^{pre}} \left(\frac{1}{K_d^{pre}} - \frac{1}{K_m} \right) \quad . \quad (6.13)$$

To get rid of ϕ_c in equation (6.11), we can get help from following equation:

$$K_d^{post} = K_m \left(1 - \phi^{post} / \phi_c \right) \quad . \quad (6.14)$$

From equations (6.11) and (6.14), there is:

$$\frac{\mu_d^{post}}{K_d^{post}} = \frac{\mu_m}{K_m} = \frac{\mu_d^{pre}}{K_d^{pre}} \quad . \quad (6.15)$$

Re-write equation (6.15), μ_d^{post} can be calculated from K_d^{post} and K_d^{pre} :

$$\mu_d^{post} = \frac{K_d^{post}}{K_d^{pre}} \mu_d^{pre} = \frac{K_d^{post}}{K_d^{pre}} \mu_{pre}^* \quad . \quad (6.16)$$

Actually, equations (6.11) and (6.14) are alternative experimental methods to calculate μ_d^{post} and K_d^{post} .

In the above derivation, we assume that K_ϕ doesn't change if $\phi^{post} \neq \phi^{pre}$. But K_ϕ is generally dependent on porosity, Mavko et al. (1995) gave the following equation to describe this relationship:

$$K_\phi = K_m(\phi_c - \phi) \quad . \quad (6.17)$$

From this equation, we can get the relationship of K_ϕ^{post} and K_ϕ^{pre} :

$$K_\phi^{post} = K_\phi^{pre} - K_m(\phi^{post} - \phi^{pre}) \quad , \quad (6.18)$$

where K_ϕ^{post} and K_ϕ^{pre} are the effective dry rock pore space incompressibilities for post- and pre-production, and equation (6.13) will be much complicated:

$$\frac{1}{K_d^{post}} = \frac{1}{K_m} + \frac{\phi^{post}}{\frac{K_m K_d^{pre} \phi^{pre}}{K_m - K_d^{pre}} - K_m(\phi^{post} - \phi^{pre})} \quad . \quad (6.19)$$

When we know μ_d^{post} and K_d^{post} , Gassmann's equation can be used to calculate velocities for post-production.

If

$$a = \frac{K_d^{post}}{K_m - K_d^{post}} + \frac{K_f^{post}}{\phi^{post} (K_m - K_f^{post})} ,$$

the saturated bulk modulus K_{post}^* for post-production will be:

$$K_{post}^* = \frac{a}{1+a} K_m , \quad (6.20)$$

and

$$V_p^{post} = \sqrt{\frac{K_{post}^* + \frac{4}{3} \mu_d^{post}}{\rho^{post}}} , \quad (6.21)$$

$$V_s^{post} = \sqrt{\frac{\mu_d^{post}}{\rho^{post}}} , \quad (6.22)$$

where V_p^{post} and V_s^{post} are P-wave and S-wave velocities for post-production.

6.3 Fluid substitution without S-wave sonic log data

A practical problem arises when we wish to estimate the change of V_p during fluid substitution, but the shear velocity is unknown – almost always the case in situ. Then, strictly speaking, the bulk modulus cannot be extracted from V_p , and Gassmann's equation cannot be applied. To get around this problem, a common approach is to estimate V_s from an empirical V_p - V_s relation (Castagna et al., 1985, Mavko et al., 1995), or to assume a dry rock Poisson's ratio and invert (Gregory, 1977) or iteratively use Gassmann's equation for the desired fluids (Greenberg et al., 1992).

6.3.1 Castagna's equation for fluid saturated rocks

Castagna et al. (1985) established general V_p - V_s relationships for clastic silicate rocks by comparing in-situ and laboratory data with theoretical model data. For water-saturated clastic silicate rocks, shear wave velocity is approximately linearly related to compressional wave velocity:

$$V_s^{wet} = A_c V_p^{wet} + B_c \quad , \quad (6.23)$$

where V_p^{wet} and V_s^{wet} are P-wave and S-wave velocities for wet case, A_c and B_c are Castagna's coefficients and should be calibrated for in-situ data set.

If the well in the reservoir is just saturated with water, then V_p^{pre} from the original well log data is equal to V_p^{wet} , we can get V_s^{wet} from equation (6.23) right away. But if the reservoir is hydrocarbon bearing, we need to get V_p^{wet} from V_p^{pre} first.

Mavko et al. (1995) gave an equivalent version of Gassmann's equation:

$$\frac{M^*}{M_m - M^*} \approx \frac{M_d}{M_m - M_d} + \frac{M_f}{\phi(M_m - M_f)} \quad , \quad (6.24)$$

where M is P-wave modulus, which is defined as:

$$M = \rho V_p^2 = K + \frac{4}{3}\mu \quad . \quad (6.25)$$

The subscripts have the same meaning as those in bulk modulus.

Equation (6.24) is for a hydrocarbon bearing reservoir. For the wet case, there is:

$$\frac{M_{wet}^*}{M_m - M_{wet}^*} \approx \frac{M_d}{M_m - M_d} + \frac{M_w}{\phi(M_m - M_w)} \quad , \quad (6.26)$$

where M_{wet}^* is saturated P-wave modulus for wet case, M_w is P-wave modulus of water.

Subtract equation (6.26) from equation (6.24), then:

$$\frac{M_{wet}^*}{M_m - M_{wet}^*} \approx \frac{M^*}{M_m - M^*} - \frac{M_f}{\phi(M_m - M_f)} + \frac{M_w}{\phi(M_m - M_w)} \quad . \quad (6.27)$$

If

$$d = \frac{M^*}{M_m - M^*} - \frac{M_f}{\phi(M_m - M_f)} + \frac{M_w}{\phi(M_m - M_w)} ,$$

then:

$$M_{wet}^* = \frac{M_m}{1+d} d . \quad (6.28)$$

From previous ρ_w^{pre} , ϕ^{pre} , and ρ_m , there is:

$$\rho_{wet} = \rho_w^{pre} \phi^{pre} + \rho_m(1 - \phi^{pre}) ,$$

and finally

$$V_p^{wet} = \sqrt{\frac{M_{wet}^*}{\rho_{wet}}} . \quad (6.29)$$

Now, we can use equation (6.23) again to get V_s^{wet} .

Because saturated shear modulus is assumed to be independent of fluids, we can easily get V_s^{pre} from V_s^{wet} :

$$V_s^{pre} = V_s^{wet} \sqrt{\frac{\rho_{wet}}{\rho^{pre}}} , \quad (6.30)$$

and we continue the process described in 6.2.

6.3.2 Estimating dry rock Poisson's ratio

For unconsolidated sands, in the absence of S-wave data, Gregory (1977) suggested using an estimated dry rock Poisson's ratio σ_{dry} as the additional seed to make the calculation. For most dry rocks and unconsolidated sands, σ_{dry} is about 0.1 and is independent of pressure. Gregory (1977) further pointed out that the calculated P-wave velocity is not very sensitive to the value of σ_{dry} . Fortunately, the error made in P-wave velocity estimation for an estimated dry rock Poisson's ratio is usually small.

Since the frequencies in seismic records are low, Biot's (1956) theory of wave propagation in the form and notation given by White (1965) can be used and the P-wave modulus (M_d^{pre}) of the empty skeleton of rock is related to bulk modulus and Poisson's ratio by:

$$M_d^{pre} = \frac{3(1 - \sigma_{dry})}{1 + \sigma_{dry}} K_d^{pre} \quad , \quad (6.31)$$

where σ_{dry} is Poisson's ratio of dry rock and is assumed to be 0.1, K_d^{pre} is the frame bulk modulus of rock before production and will be calculated later.

If

$$s = \frac{3(1 - \sigma_{dry})}{1 + \sigma_{dry}} \quad , \quad a = s - 1 \quad , \quad b = \phi^{pre} \left(\frac{K_m}{K_f^{pre}} - 1 \right) s - s + \frac{M^*}{K_m} \quad ,$$

$$c = -\phi^{pre} \left(s - \frac{M^*}{K_m} \right) \left(\frac{K_m}{K_f^{pre}} - 1 \right) \quad , \quad y = 1 - \frac{K_d^{pre}}{K_m} \quad ,$$

then, y can be solved using quadratic equation:

$$ay^2 + by + c = 0 \quad ,$$

and then:

$$y = \frac{-b + \sqrt{b^2 - 4ac}}{2a} \quad , \quad (6.32)$$

where ϕ^{pre} , K_m , K_f^{pre} and M^* have been given or calculated in previous part.

From y , we can get K_d^{pre} :

$$K_d^{pre} = K_m * (1 - y) \quad , \quad (6.33)$$

and then:

$$\mu_d^{pre} = \mu_{pre}^* = 3(1 - 2\sigma_{dry}) \frac{K_d^{pre}}{2(1 + \sigma_{dry})}, \quad (6.34)$$

where μ_d^{pre} and μ_{pre}^* are shear moduli of dry rock and saturated rock for pre-production.

When K_d^{pre} and μ_d^{pre} are got, we will be able to rerun the calculation from equations (6.8) to (6.22).

6.3.3 The Greenberg-Castagna calculation

Greenberg and Castagna (1992) developed a general iterative method to predict shear wave velocity in porous rocks, if reliable compressional wave velocity, lithology, porosity and water saturation data are available. The success of the method depends on: (1) robust relationships between compressional and shear wave velocities for water saturated pure porous lithologies; (2) nearly linear mixing laws for solid rock constituents; (3) first-order applicability of the Gassman theory to real rocks.

Empirical relations between body shear wave velocity V_{Si} and compressional wave velocity V_{Pi} in brine filled rocks of pure (monomineralic) lithology have been adequately represented by polynomials (e.g. Castagna et al., 1992). Shear wave velocity V_{Sc} in a homogeneous composite (multimineralic) brine filled rock can be approximated by averaging the harmonic and arithmetic means of the constituent pure porous lithology shear wave velocities. This averaging is analogous to obtaining a Voigt-Reuss-Hill average for the elastic moduli. For a homogeneous composite with compressional wave velocity V_{Pc} , the porosity can be partitioned among L constituents such that $V_{P1} \sim V_{P2} \sim \dots \sim V_{PL} \sim V_{Pc}$. This partitioning approximation improves as the porosity increases or the constituent grain velocities converge. These observations specify an approximate

relation between V_{Sc} and V_{Pc} for brine filled rocks given by:

$$V_{Sc} = \frac{1}{2} \left[\left(\sum_{i=1}^L X_i \sum_{j=0}^{N_i} a_{ij} V_{Pc}^j \right) + \left(\sum_{i=1}^L X_i \left(\sum_{j=0}^{N_i} a_{ij} V_{Pc}^j \right)^{-1} \right)^{-1} \right], \quad (6.35)$$

where, X_i is the dry lithology volume fraction of lithological constituent i , a_{ij} are the empirical coefficients and N_i is the order of polynomial i .

Since an analytic solution for equation (6.35) is intractable, Greenberg and Castagna (1992) developed an iterative method. Since typical in-situ variation of compressional wave velocity with brine saturation is less than 20%, a scheme to optimize the difference between compressional wave velocities at in-situ water saturation S_w and 100% brine saturation can be initiated.

Using subscript s to denote properties at brine saturation S_w and subscript l to denote properties at 100% brine saturation, then:

$$V_{Plc} = (1 + \delta) V_{Psc}, \quad (6.36)$$

where δ is a slack variable with a probable optimal value in the range 0.0-0.2.

Combining various equations in previous chapters yield a second estimate of V_{Plc} (V'_{Plc} below), which can be compared with the initial estimation of V_{Plc} from equation (6.36) to establish an iteration convergence criterion. V'_{Plc} can be obtained in four steps:

(1) Use equation (6.36), and apply equation (6.35) followed by equation (3.4) at $S_w=1$:

$$\begin{aligned} \mu_{1c} &= \mu_c \\ &= \frac{1}{4} \rho_{1c} \left[\left(\sum_{i=1}^L X_i \sum_{j=0}^{N_i} a_{ij} (1 + \delta)^j V_{Psc}^j \right) + \left(\sum_{i=1}^L X_i \left(\sum_{j=0}^{N_i} a_{ij} (1 + \delta)^j V_{Psc}^j \right)^{-1} \right)^{-1} \right]^2. \end{aligned}$$

(2) Apply equation (3.3) at S_w using μ_c from (1):

$$K_{sc} = \rho_{sc} V_{psc}^2 - \frac{4}{3} \mu_c \quad .$$

(3) Solve Gassmann's equation (3.1) for K_d and apply result at S_w using K_{sc} from (2):

$$K_d = \frac{K_m (\lambda K_{sc} - 1)}{\lambda K_m - 2 + \frac{K_{sc}}{K_m}} \quad ,$$

where

$$\lambda = \frac{\phi}{K_m} + \frac{1-\phi}{K_{sf}} \quad .$$

(4) Apply equations (3.3) and (3.1) at $S_w=1$ using μ_c from (1) and K_d from (3):

$$K_{1c} = K_d + \frac{\left(1 - \frac{K_d}{K_m}\right)^2}{\frac{\phi}{K_{1f}} + \frac{1-\phi}{K_m} + \frac{K_d}{K_m^2}} \quad ,$$

and

$$V'_{p1c} = \sqrt{\frac{K_{1c} + \frac{4}{3} \mu_c}{\rho_{1c}}} \quad .$$

When the measurements and the required shear wave velocity are for 100% brine saturated rock, $\delta=0$ and iterations are unnecessary. Otherwise, estimate error= $V'_{p1c}-V_{p1c}$ and see whether the error is small enough. If not, estimate next trial δ and restart the iteration.

6.4 Fluid substitution for a real well

One well with full set of well logs data from Plover Lake heavy oil field was selected to do fluid substitution. The quality of well logs data from this well is quite good.

Methods of fluid substitution with and without S-wave sonic data are all performed, the respective results are compared with each other, similar conclusions are derived.

Based on the previous part of this chapter, reservoir parameters and fluid properties for pre- and post-production conditions are shown in Table 6.2. First, the method of fluid substitution with S-wave sonic data is performed. To estimate well logs after heavy oil cold production, we have to calculate well logs data for wet case first from well logs data acquired in original reservoir condition.

Figure 6.4 shows the original (blue) and modified (red) logs for wet case within the analysis zone. This figure tells us that the changes to logs output from the fluid substitution. There is almost no difference between original and modified logs only except that water saturation is improved to 100% from 25%.

Table 6.2: Reservoir parameters and fluid properties for pre- and post-production conditions.

Parameters	Pre-production	Post-production
Bulk modulus of matrix (GPa)	39	39
Shear modulus of matrix (GPa)	27	27
Water saturation (%)	25	19
Bulk modulus of hydrocarbon (GPa)	2.2166	0.026
Density of hydrocarbon (g/cc)	0.97	0.743
Bulk modulus of brine (GPa)	2.37	2.34
Density of brine (g/cc)	1.01	1.0088

From calculated well logs in wet case, we can get logs for post-production condition by fluid substitution, water saturation is reduced to 19% from 100% (Figure

6.5). This figure displays dramatic changes to logs output due to cold production. There is about 300 m/s reduction for P-wave velocity, 0.05 g/cc reduction for density data, and 20 m/s improvement for S-wave velocity. Actually, the about 10% reduction of P-wave velocity is from about 30% reduction of saturated bulk modulus. Finally, there is about 20% reduction of Poisson's ratio. From original and above modified logs data, synthetic seismograms are created for wet case, pre- and post-production conditions respectively (Figure 6.6). The wavelet is created zero phase Ricker wavelet with 70 Hz dominant frequency and 200 ms length (Figure 6.7). Figure 6.5 implicates the different AVO response from the changes of P-wave velocity and density due to cold production, but not visually reveals the difference between those synthetic seismograms (Figure 6.6). Figure 6.8 displays the events that have been picked from the top of the reservoir in three synthetic seismograms. The reflection from the top of the reservoir for post-production is obviously discriminated from the other two cases, and has more negative intercept (normal P-wave reflection coefficient).

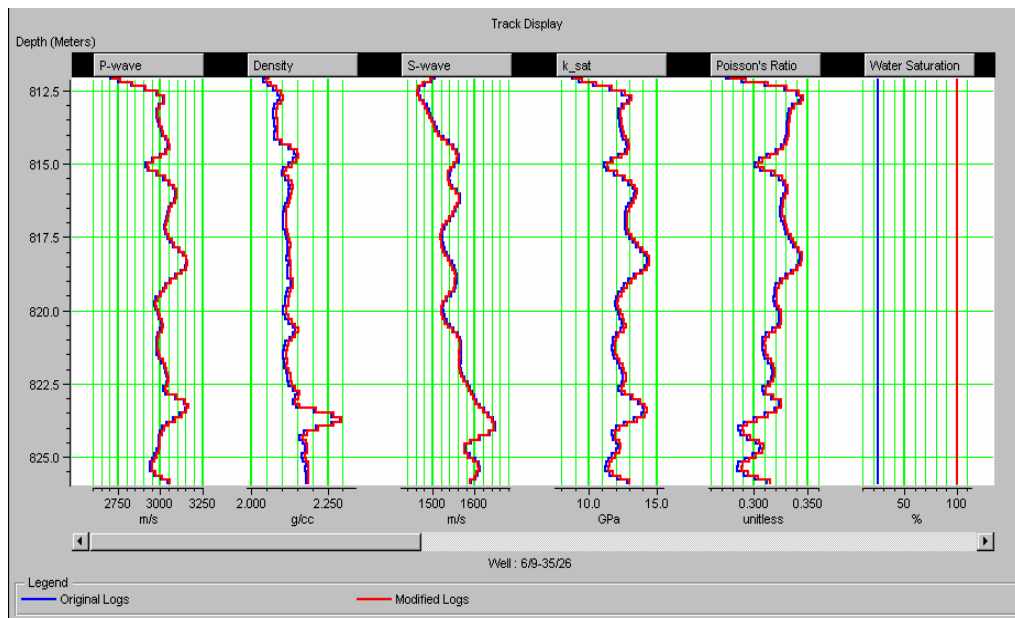


Figure 6.4: Well logs for pre-production (blue) and wet case (red) within analysis zone.

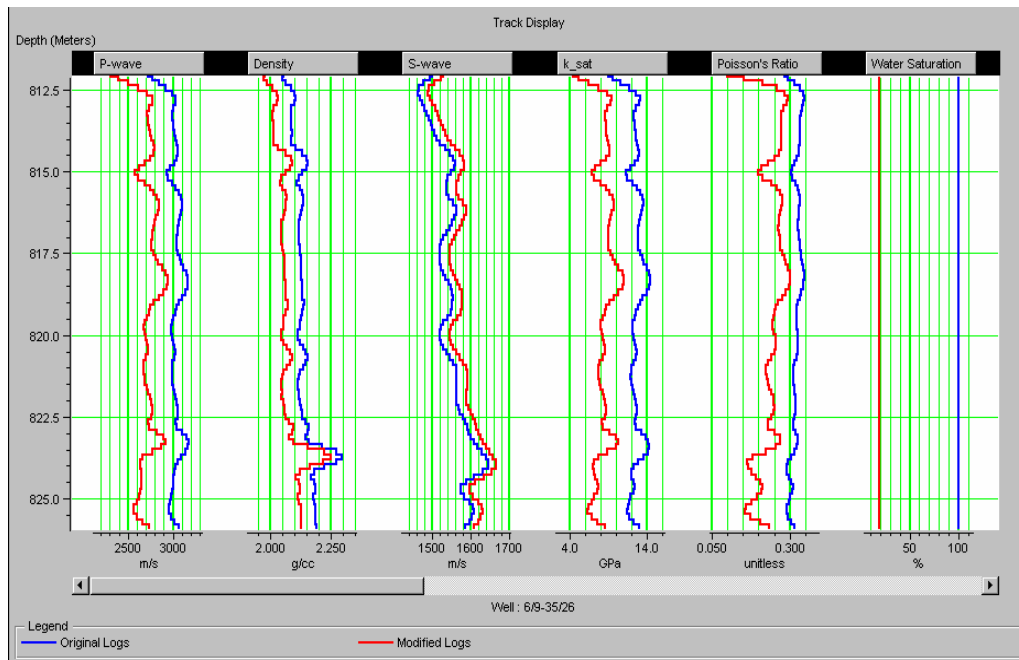


Figure 6.5: Well logs for wet case (blue) and post-production (red) within analysis zone.

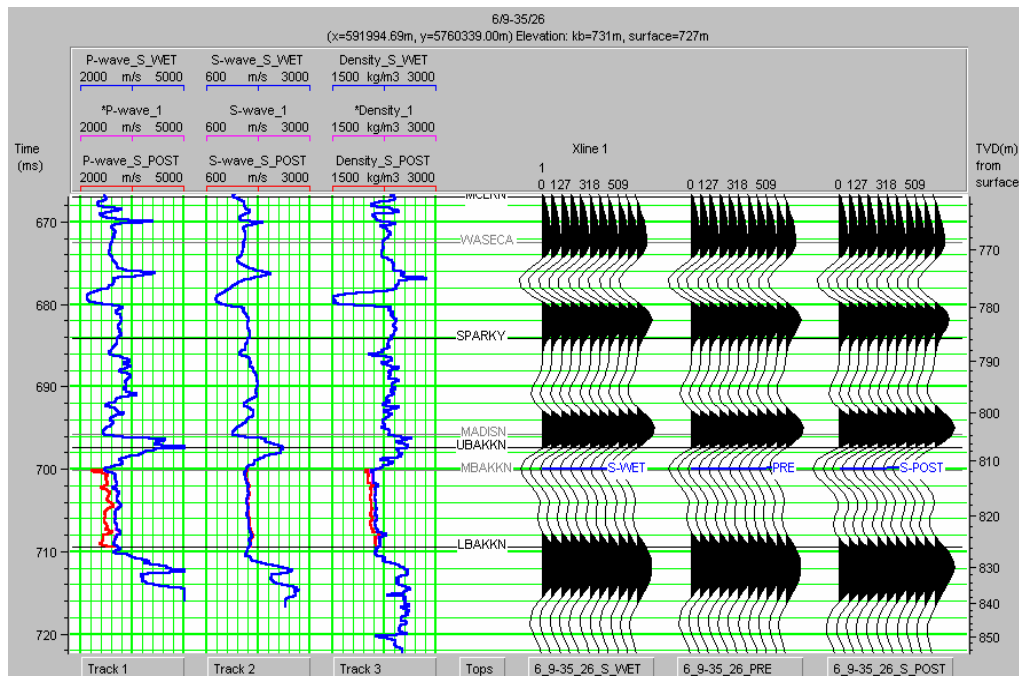


Figure 6.6: Synthetic seismograms for wet case, pre- and post-production conditions.

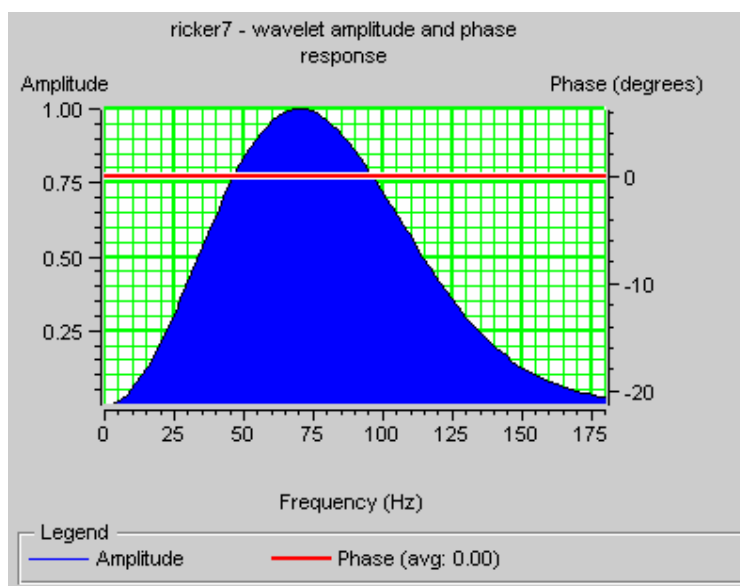


Figure 6.7: Created zero phase Ricker wavelet with 70 Hz dominant frequency.

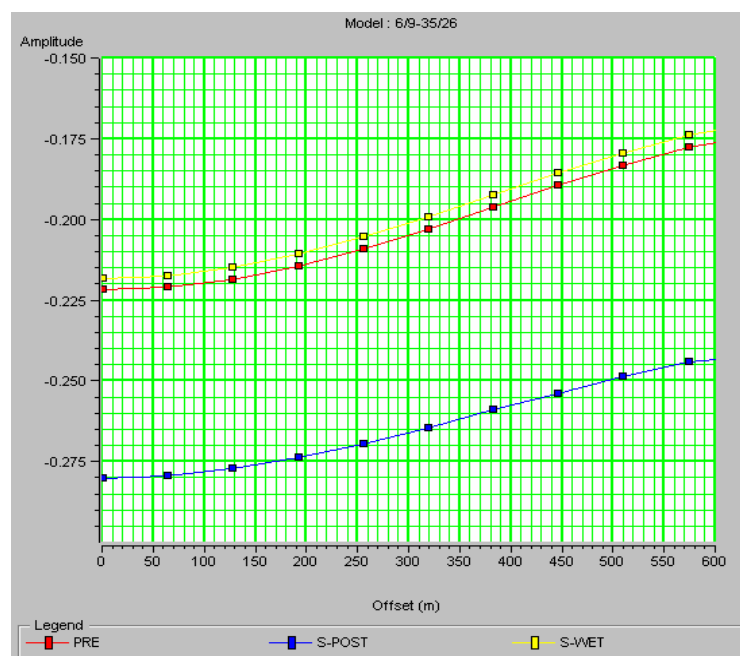


Figure 6.8: Picked events from the top of the reservoir in three synthetic seismograms.

The above AVO responses for all three conditions do not belong to any of the three classifications given by Rutherford and Williams (1989), which is based only on the

P-wave normal incidence reflection coefficient. Castagna et al. (1998) augmented Rutherford and Williams' classification based on both intercept and gradient, and defined Class IV with negative intercept, but positive gradient, whereas both intercept and gradient of Class III are negative (Figure 6.9). In other words, Class III sands are lower impedance than the overlying shales (classical bright spots), and exhibit increasing reflection magnitude (more negative) with offset, and Class IV sands are also lower impedance, but reflection magnitude decreases (positive gradient) with increasing offset (Figure 6.10).

Table 6.3 summarizes the possible AVO behavior for the various types of gas sands (Castagna et al., 1998). They found either an A-B quadrant identification or an augmented Rutherford and Williams' classification to be more informative than one based only on the normal-incidence compressional wave reflection coefficient. Class IV sands, though not explicitly discussed by Rutherford and Williams, may be considered to be a subdivision of their Class III sands.

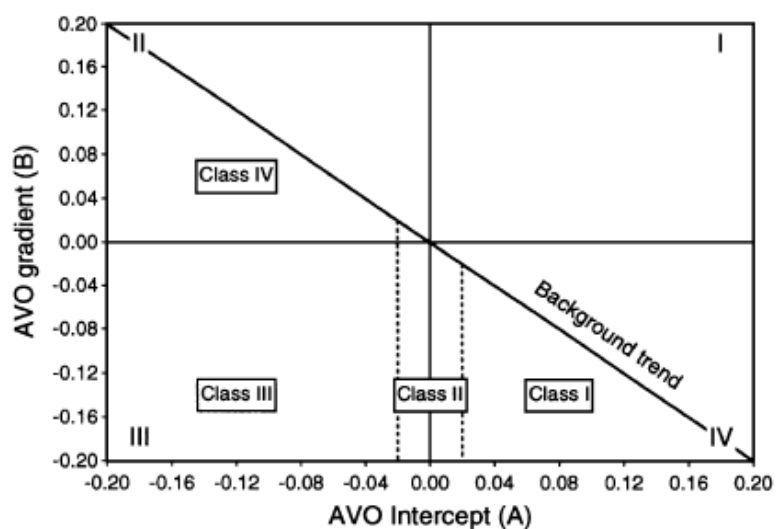


Figure 6.9: AVO intercept (A) versus gradient (B) crossplot showing four possible quadrants (Castagna et al., 1998).

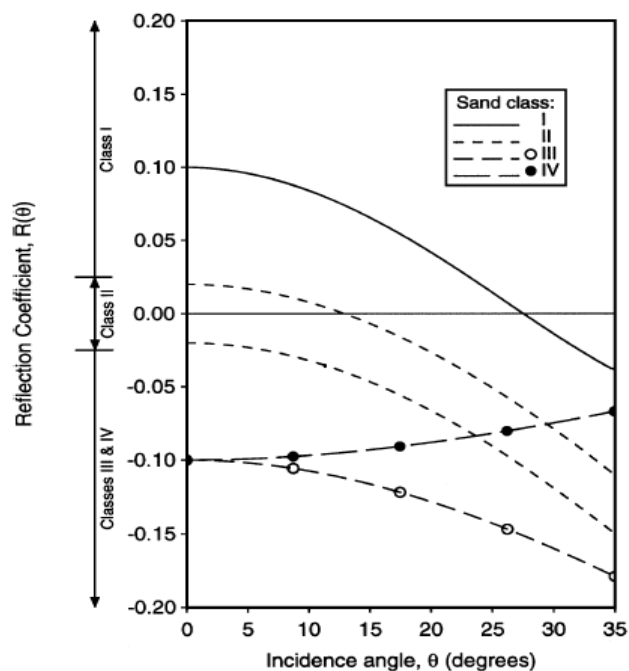


Figure 6.10: Plane-wave reflection coefficients at the top of each augmented Rutherford and Williams' classification of sands (Castagna et al., 1998).

Table 6.3: Top sand reflection coefficient versus offset behavior for the four augmented Rutherford and Williams' Classes I-IV, assuming a typical "background" trend with negative slope (Castagna et al., 1998).

Class	Relative impedance	Quadrant	A	B	Remarks
I	Higher than overlying unit	IV	+	-	Reflection coefficient (and magnitude) decrease with increasing offset
II	About the same as the overlying unit	III or IV	\pm	-	Reflection magnitude may increase or decrease with offset, and may reverse polarity
III	Lower than overlying unit	III	-	-	Reflection magnitude increases with offset
IV	Lower than overlying unit	II	-	+	Reflection magnitude decreases with offset

Class IV sands frequently occur when a porous sand is overlain by a high-velocity unit, such as a hard shale (e.g., siliceous or calcareous), siltstone, tightly cemented sand or a carbonate (Castagna et al., 1998). Table 6.4 gives well log V_p , V_s and density for a sand and an overlying shale and tight unit. Castagna et al. (1998) showed that when the sand is overlain by shale, the AVO intercept (A) is large and negative, and the AVO

gradient (B) is negative. This falls in quadrant III of Figure 6.9, and represents a typical well behaved Rutherford and Williams' Class III sand. However, when the overlying unit is a tight unit, the AVO intercept (A) is large and negative, but the AVO gradient (B) is positive. Thus, although one would classify this reflection as Class III based on compressional wave impedance contrast alone, the reflector falls in quadrant II of Figure 6.9, since its amplitude decreases with offset. Furthermore, the same sand produces very different AVO behavior depending on its overlying shale. Thus, it is incorrect to classify a reflector based on the properties of the sand alone.

Table 6.4: Well log velocities and densities for an East African gas sand and overlying strata (Castagna et al., 1998).

Lithology	V_P (m/s)	V_S (m/s)	ρ (gm/cm ³)
Shale	2900	1330	2.29
Tight unit	3250	1780	2.44
Gas sand	2540	1620	2.09

To understand this unusual but highly significant behavior, Castagna et al. (1998) referred to the original Richards and Frasier (1976) approximation as given in Aki and Richards (1980) to approximately decompose the contributions to the reflection coefficient variation with offset by changes in V_p , V_s and density (ρ). Actually, from the approximation of Wiggins et al. (1983) as given in Hilterman (2001), we can also get a clear understanding of this unusual behavior:

$$R(\theta) \approx R_p + (R_p - 2R_s) \sin^2 \theta \quad , \quad (6.37)$$

where θ is P-wave incidental angle, R_p and R_s are normal-incidence reflection coefficients of P-wave and S-wave respectively. From above equation, the AVO intercept (A) and gradient (B) can be easily expressed as:

$$A = R_p \quad , \quad (6.38)$$

$$B = R_p - 2R_s \quad . \quad (6.39)$$

For V_p , V_s and density (ρ) given in Table 6.4, when the gas sand is overlain by shale, R_p and R_s are -0.1115 and 0.0529 respectively, and gradient B is -0.2173. However, when the gas sand is overlain by tight unit, R_p and R_s are -0.198 and -0.124 respectively, and gradient B is +0.05, which is a positive value, the reflection magnitude will decrease (more positive) with offset.

As to the in-situ case, the target zone of the Middle Bakken member is overlain by the Upper Bakken member with black, pyretic carbonaceous and fissile shale (Mageau et al., 2001). Original well log V_p , V_s and density (ρ) for the Middle Bakken member and the overlying Upper Bakken member are listed in Table 6.5, the relevant R_p and R_s for pre-production condition are -0.246 and -0.262 respectively, thus intercept A and gradient B are -0.246 and +0.278, the reflection coefficient of the top of the Middle Bakken member sand becomes more positive with increasing offset, yet decreases in amplitude with offset. For post-production condition, R_p and R_s are -0.331 and -0.279 respectively, thus intercept A and gradient B are -0.331 and +0.227, with more negative intercept, similar positive gradient.

Table 6.5: Well log velocities and densities for the in-situ case.

Lithology	V_p (m/s)	V_s (m/s)	ρ (g/cc)
Upper Bakken carbonaceous shale	4300	2200	2.5
Middle Bakken sand (pre-production)	3100	1530	2.1
Middle Bakken sand (post-production)	2700	1550	2.0

With the aid of Richards and Frasier's (1976) approximation, Castagna et al. (1998) further pointed out that the contribution due to the density contrast has a positive slope for both Class III and IV sands, whereas the contribution due to the V_p contrast has a negative slope. However, the key parameter is the shear wave velocity contrast. When sands have higher shear wave velocity (Class III), the shear contribution becomes more negative with increasing offset, thereby enhancing the total amplitude. On the other hand, when pay sands have lower shear wave velocity (Class IV), the shear contribution becomes more positive with increasing offset. The net result is a small decrease in the total reflection coefficient with increasing offset, thereby resulting in a Class IV sand in quadrant II, having a positive gradient B .

Most importantly, Castagna et al. (1998) pointed out that whereas Class IV sands exhibit unexpected absolute AVO behavior according to established rules of thumb and are difficult to interpret on partial offset stacks or using product (AXB) indicators, they do not confound A versus B crossplot based indicators, such as Smith and Gidlow's (1987) fluid factor. The "fluid factor" concept was introduced in Smith and Gidlow (1987) to highlight gas bearing sandstones. The crossplot of V_p against V_s in Figure 6.11 is derived from Castagna et al. (1985). Water saturated sandstones, siltstones and shales fall approximately along the mudrock line. Gas saturated sandstones have lower P-wave velocities and slightly higher S-wave velocities (Domenico, 1974) and therefore fall in the indicated gas zone. Based on the equation of the mudrock line given by Castagna et al. (1985),

$$V_p = 1360 + 1.16V_s \quad (\text{m/s}), \quad (6.40)$$

Fatti et al. (1994) derived the following equation:

$$R_p - 1.16(V_s / V_p)R_s = 0 \quad . \quad (6.41)$$

This relationship holds true along the mudrock line, and the fluid factor (ΔF) was defined

by Fatti et al. (1994) as:

$$\Delta F = R_p - 1.16(V_s/V_p)R_s \quad (6.42)$$

If the layers above and below the boundary that produce a reflection lying on the mudrock line, then $\Delta F = 0$. But if one of the layers lies on and the other lies off the mudrock line, then $\Delta F \neq 0$. For example, if one of the layers is a shale or a water sandstone and the other layer is a gas sandstone, this produces a nonzero value of ΔF . For the in-situ case, the gas sandstone is replaced by foamy oil sandstone, we would expect nonzero values of ΔF at the top and base of foamy oil sandstones, but zero values of ΔF for all other boundaries. The amplitude of the ΔF “reflection” from gas sandstones should be proportional to the separation between the gas sandstone and mudrock lines in Figure 6.11.

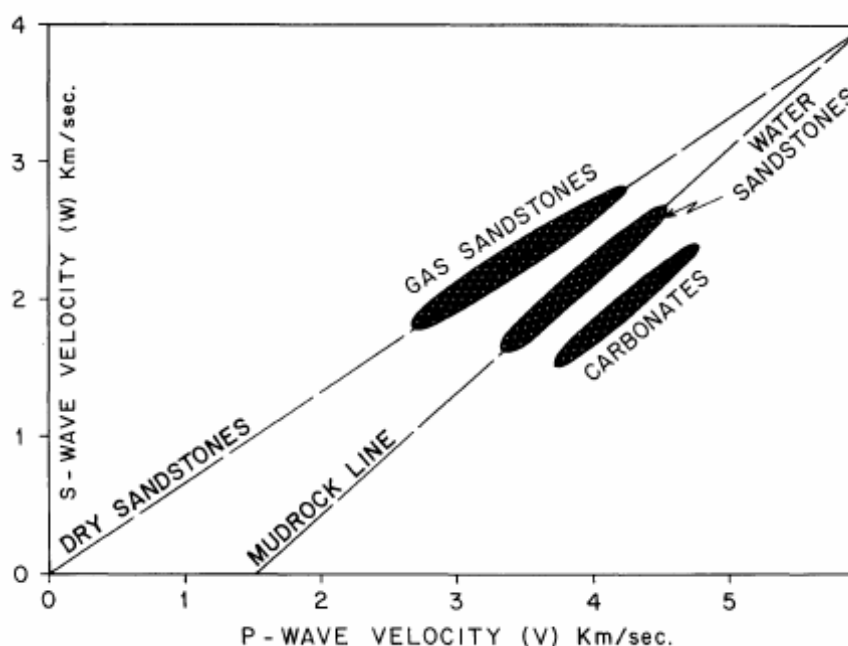


Figure 6.11: Diagrammatic crossplot of P-wave velocity against S-wave velocity (Castagna et al., 1985).

Fatti et al. (1994) also gave another way of looking at equation (6.42): ΔF is the difference between the actual P-wave reflection coefficient R_p and the calculated P-wave reflection coefficient ($1.16(V_s/V_p)R_s$) for the same sandstone in a water saturated state. The calculated P-wave reflection coefficient is determined from the S-wave reflection coefficient (R_s) using the local mudrock line relationship. Finally, Fatti et al. (1994) re-wrote the equation (6.42) as:

$$\Delta F(t) = R_p(t) - g(t)R_s(t) \quad , \quad (6.43)$$

where,

t = two-way time;

$\Delta F(t)$ =fluid factor trace;

$R_p(t)$ =P-wave reflectivity trace;

$R_s(t)$ =S-wave reflectivity trace;

$g(t)=M(V_s/V_p)$ =a time-varying gain function;

M =slope of the mudrock line, which could be an appropriate local value, rather than that of Castagna et al. (1985).

The function $g(t)$ is time-varying because V_s/V_p varies with time (Figure 6.12), and the slope of the mudrock line also vary with depth. Figure 6.13 is the crossplot of V_p against V_s for the whole well depth from the in-situ well, the regressional relationship between V_p and V_s is:

$$V_p = 1128.15 + 1.30793V_s \quad (\text{m/s}) \quad , \quad (6.44)$$

and M is 1.30793. Meanwhile, the regressional relationship between V_p and V_s from the crossplot of V_p against V_s around the target zone for wet condition (Figure 6.14) is:

$$V_p = 734.648 + 1.57527V_s \quad (\text{m/s}) \quad , \quad (6.45)$$

and M is 1.57527. Combined with the value of V_p/V_s ratio (≈ 2.1) around target zone in

Figure 6.10, the most appropriate value of $g(t)$ around target zone is about 0.75. If we know R_p and R_s , then equation (6.43) could be used to calculate the fluid factor.

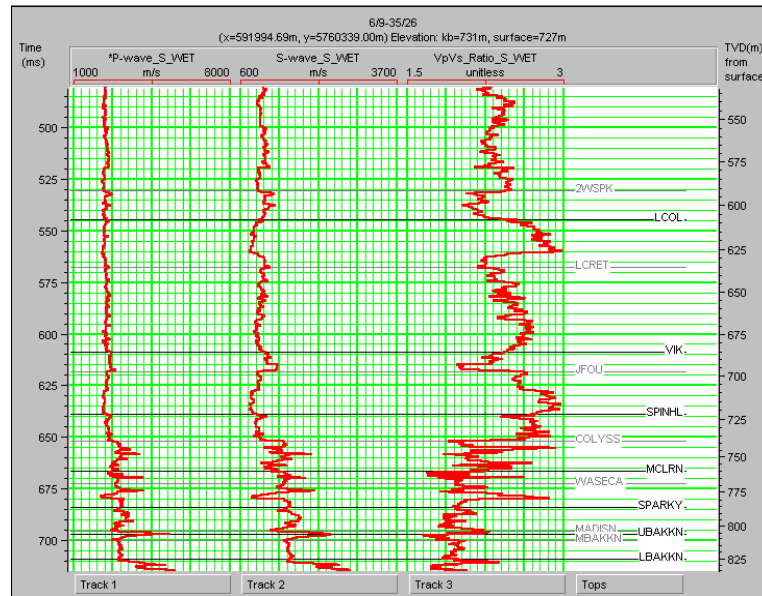


Figure 6.12: Calculated V_p/V_s ratio log from the in-situ well.

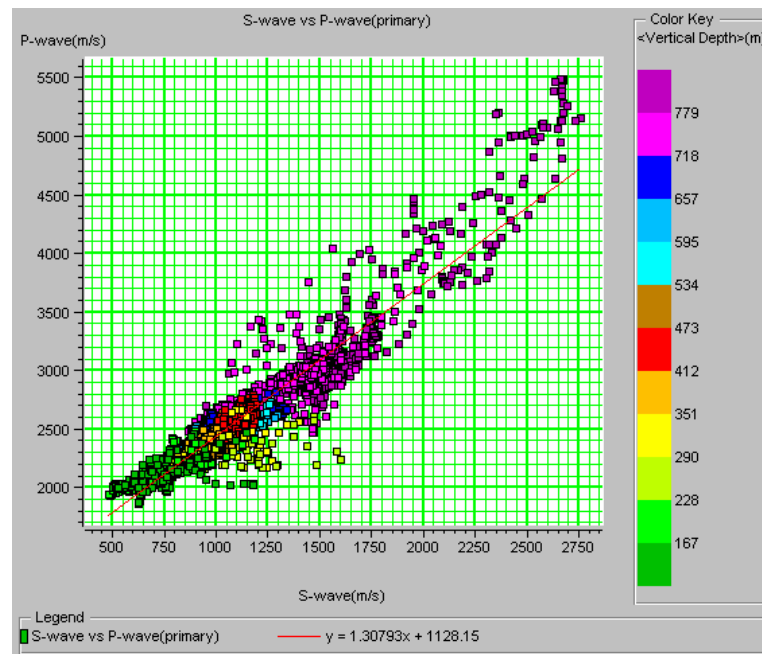


Figure 6.13: Crossplot of V_p against V_s for the whole well depth from the in-situ well.

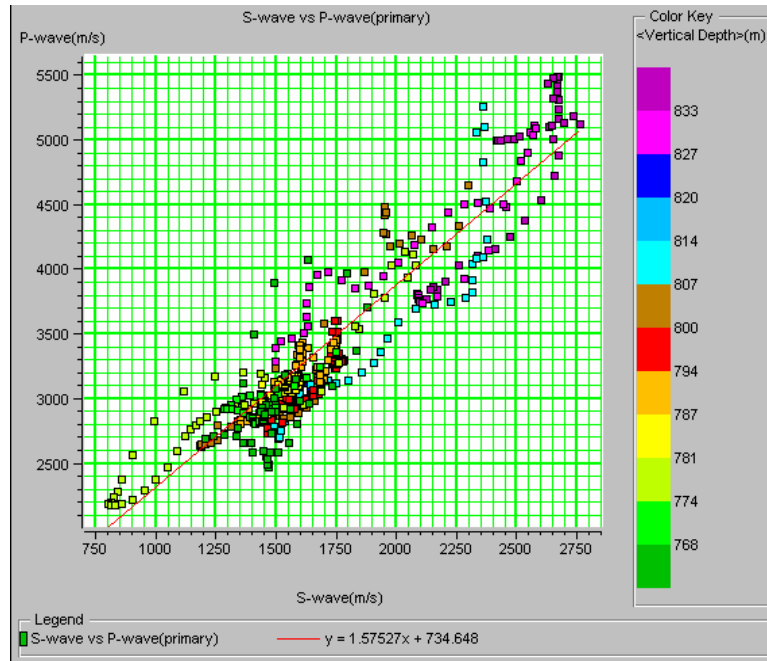


Figure 6.14: Crossplot of V_p against V_s for the target zone from the in-situ well.

To get the fluid factor, the synthetic seismograms for wet condition, pre- and post-production conditions are concatenated into one volume with replicating each of the input volumes 5 times prior to concatenation (Figure 6.15). The first six gathers is for wet condition, the second six gathers is for pre-production, and the third ones is for post-production. Then, the concatenated volume is analyzed to determine the zero-offset P-wave and S-wave reflection coefficients at each time sample, based on the Geostack method described by Fatti et al. (1994) and given by Hampson-Russell software, which describes the amplitude of any pre-stack data sample as:

$$D(x,t) = R_p(t) * a(x,t) + R_s(t) * b(x,t) , \quad (6.46)$$

where $a(x,t)$ and $b(x,t)$ are functions of the incidence angle of P-wave at this sample.

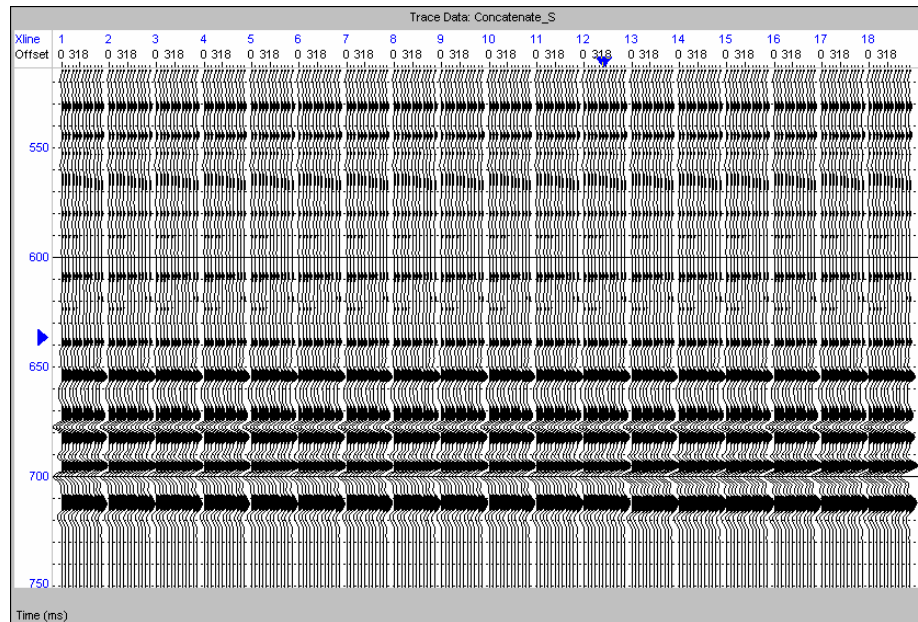


Figure 6.15: Synthetic seismograms for wet condition, pre- and post-production conditions are concatenated into one volume with replicating each of the input volumes 5 times prior to concatenation.

When the AVO attributes of R_p and R_s are calculated for every time sample in each gather, the fluid factor could be further calculated based on equation (6.43) and viewed in a single output window to see the difference of the fluid factors for the three separate conditions (Figure 6.16). The first six traces is for wet condition, the second six traces is for pre-production and the third six traces is for post-production. As described in this figure, the trace data is R_p and the fluid factor is shown in color. Figure 6.17 is the fluid factor with default $g(t)$ from software. Comparing these two figures, both reveal the different fluid factors around the target zone (700-710 ms) between post- and pre-production conditions, but the fluid factor with $g(t)=0.75$ give a better discrimination between post- and pre-production conditions, while the fluid factors for pre-production and wet conditions are similar in both figures.

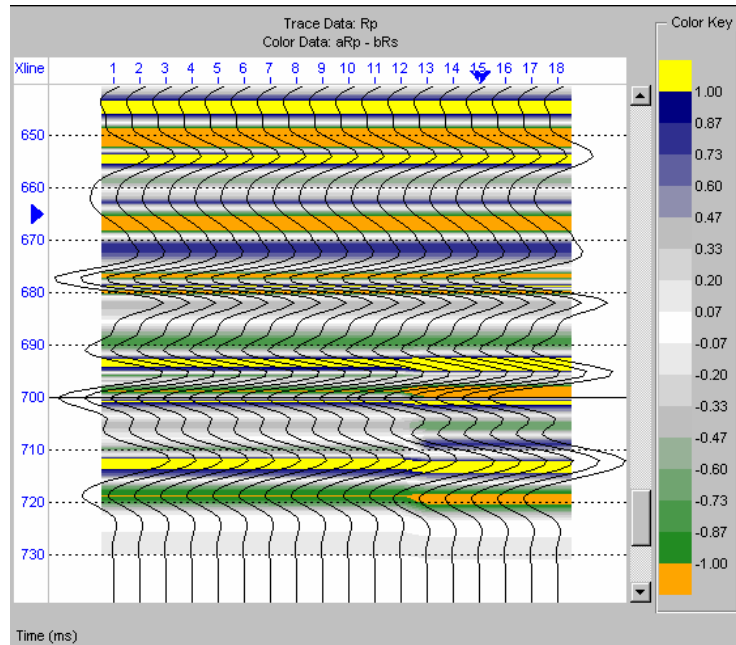


Figure 6.16: Fluid factors for the three separate conditions with $g(t)=0.75$.

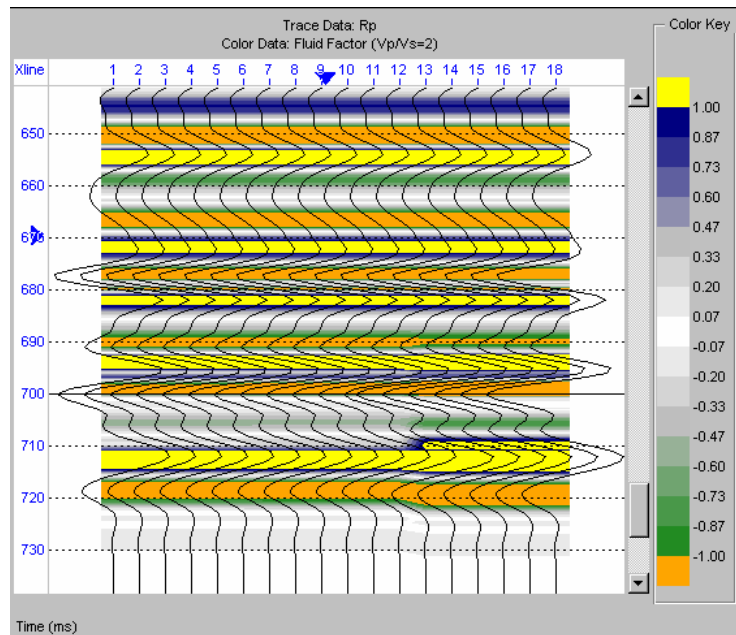


Figure 6.17: Fluid factors for the three separate conditions with default $g(t)$.

Figure 6.18 shows all three V_p/V_s ratios for pre-production, wet and

post-production conditions after fluid substitution. The curve in Track 4 is the difference of V_p/V_s ratios between post- and pre-production conditions (Track 3 and 1). There are about 0.2 reduction of V_p/V_s ratio after heavy oil cold production and about 10% reduction shown in Track 5. This figure provides a similar result with that described in Chapter 4.

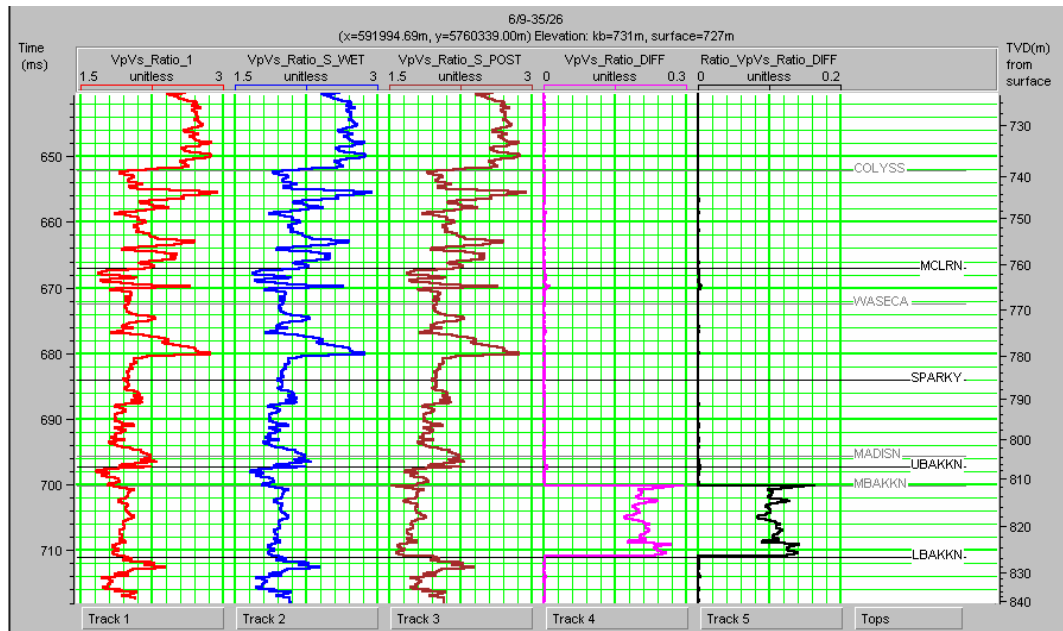


Figure 6.18: All three V_p/V_s ratios for pre-production, wet and post-production conditions after fluid substitution and the difference of V_p/V_s ratios between post- and pre-production conditions.

For the case when the S-wave sonic log data is not available, all of the three methods described in 6.3 to perform fluid substitutions are tested for the in-situ well without using the available S-wave sonic data and the results are shown in Figure 6.19 and 6.20, together with the result using available S-wave log data. In Figure 6.19, S-wave_GC_PRE is calculated S-wave log data for pre-production using Greenberg-Castagna's calculation, S-wave_DP_PRE is assuming dry rock Poisson's ratio, S-wave_C_PRE is assuming Castagna's equation is correct for wet case, while S-wave-1

is original S-wave log data. For P-wave and Density logs data, the denotations are same. In Figure 6.20, the denotations are similar with that in Figure 6.19, except that POST denotes post-production and P-wave_S_POST, S-wave_S_POST and Density_S_POST are the results with using available S-wave log data to do fluid substitution. The conclusions from these two figures are that these methods, whether using or not using original S-wave log data, will result in same P-wave and Density logs data, similar and some kind of different S-wave logs data. In both figures, the closest calculated S-wave log data to the S-wave log data with using available original S-wave log data is from Greenberg-Castagna's calculation. Assuming Castagna's equation is correct for wet case gives a relatively small S-wave log data, while assuming dry rock Poisson's ratio gives a relatively high S-wave log data. But overall, all of the methods give the similar AVO response from the top of the target zone (Figure 6.21).

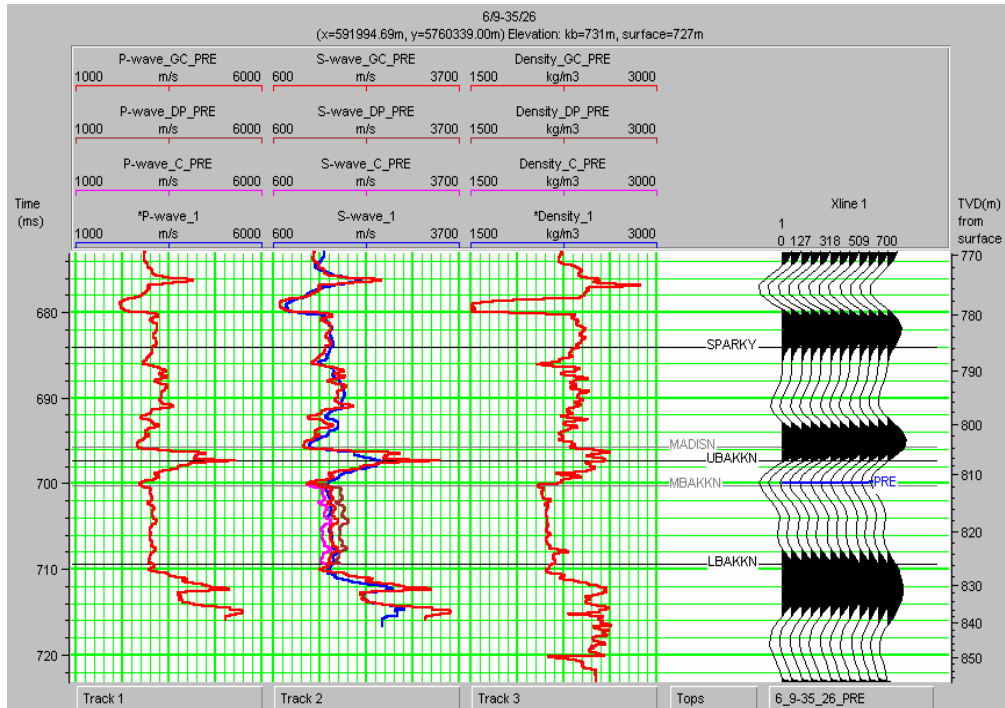


Figure 6.19: Calculated well logs from fluid substitutions for pre-production without using original S-wave log data.

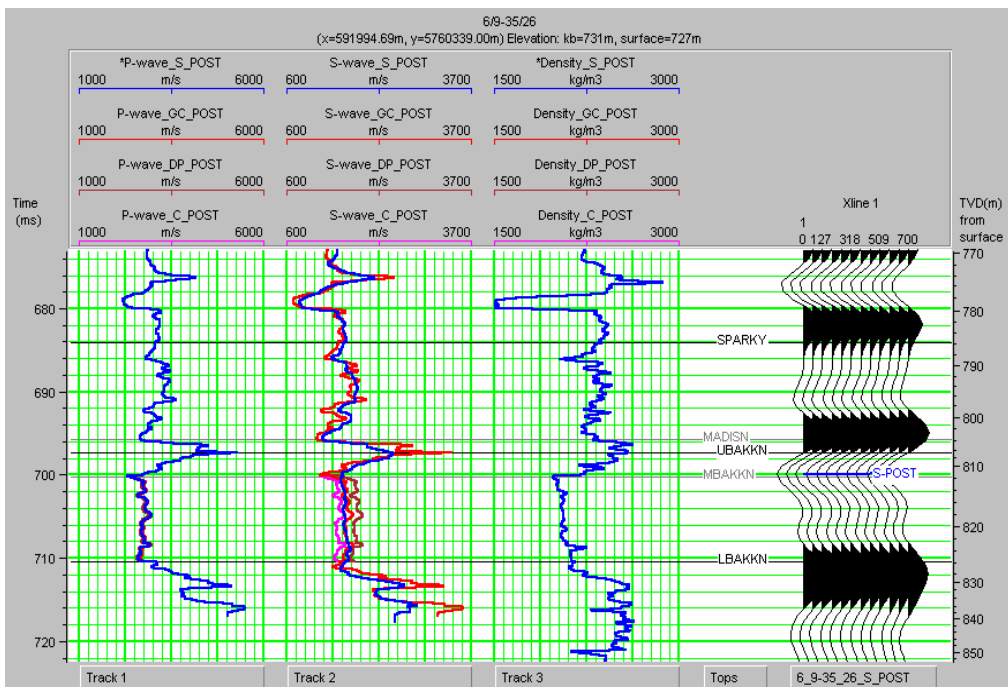


Figure 6.20: Calculated well logs from fluid substitutions for post-production without using original S-wave log data.

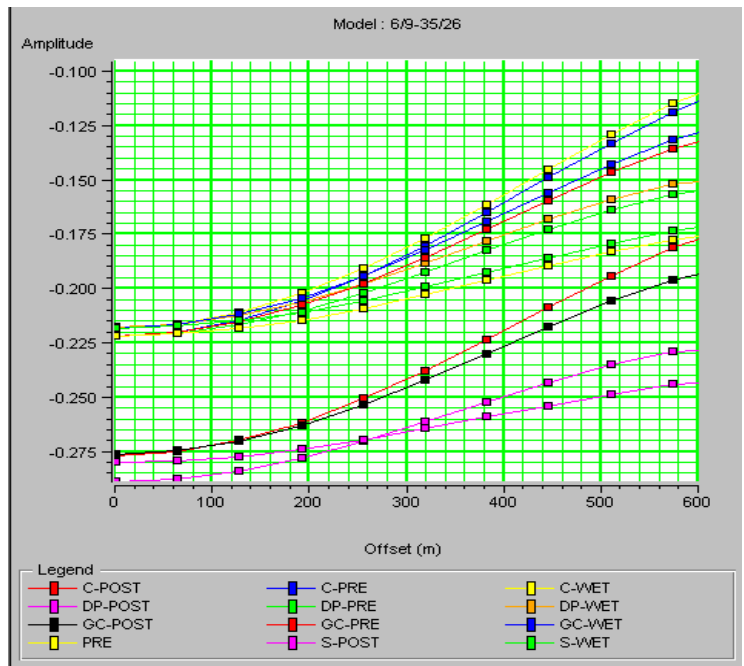


Figure 6.21: Picked events from the top of the reservoir in synthetic seismograms based on calculated well logs from fluid substitutions without using original S-wave log data.

CHAPTER 7

CONCLUSIONS AND FUTURE WORK

Simultaneous extraction of oil and sand during the heavy oil cold production generates high porosity channels termed “wormholes”. These highly permeable wormhole channels have been observed in post-production logging and radioactive tracer tests in the field. The development of wormholes causes reservoir pressure to fall below the bubble point, resulting in dissolved-gas coming out of solution to form foamy oil. Both foamy oil and wormholes are believed to be two key factors in the enhancement of oil recovery.

The presence of small amounts of gas trapped in the foamy oil can dramatically decrease the fluid bulk modulus, thereby reducing the P-wave velocity of saturated sands, while slightly increasing the S-wave velocity. Therefore, Poisson’s ratio and V_p/V_s ratio have a subsequent reduction.

To detect what kind of roles seismology can play to map the disturbance of initial reservoir state, Lines et al. (2003) revealed the possibility of detecting wormhole presence instead of imaging individual wormholes by normal seismic method. Chen et al. (2004) calculated elastic parameters of heavy oil reservoir before and after cold production based on Gassmann’s equation, and discussed the use of time-lapse reflection seismology theoretically for detecting the presence of foamy oil and wormholes. Zou et al. (2004) analyzed a repeated 3D seismic survey over a cold production field in eastern Alberta, showed an interesting correlation between time-lapse seismic changes and heavy

oil cold production. All of the above research is encouraging and confirms that time-lapse seismology can play an important role in mapping the disturbance of initial reservoir state due to heavy oil cold production.

In exploration seismology, seismic waves bring out subsurface rock and fluid information, which can be obtained from seismic traveltimes, reflection amplitudes, and phase variations. Seismic data are now commonly analyzed for determining lithology, porosity, pore fluids, and saturations, because rock physics bridges seismic data and reservoir properties and parameters. Gassmann's equation has been used for calculating the effect of fluid substitution on seismic properties using the matrix properties. But one of the assumptions for the accuracy of Gassmann's equation is that the pores are filled with a frictionless fluid (liquid, gas, or mixture). This assumption implies that the viscosity of the saturating fluid is zero. In reality, heavy oil is defined as not only having high densities, but also having extremely high viscosities. The calculations using Gassmann's equation for heavy oil are questionable.

To get around this problem, Hornby et al. (1987) predicted the behavior of oil sands using scattering theory, which is equivalent to the Hashin-Shtrikman lower bound. The model assumes that the sands grains are suspended in a host of heavy hydrocarbons. Equations from scattering theory are only applicable when pore fluid is just heavy oil, otherwise, if there is water and/or gas, the calculated saturated shear modulus μ^* will be zero and the velocity of shear wave will be zero, too.

Fortunately, Batzle et al. (2006) found that although viscosity is influenced by pressure and gas content, it is primarily a function of oil gravity and temperature. Increasing the temperature will decrease sample's viscosity, both bulk and shear moduli

decrease approximately linearly with increasing temperature, and the shear modulus approaches zero at about 80 °C. Moreover, the frequency also plays an important role for traveling waves in heavy oil. At high frequencies, such as with laboratory ultrasonics, heavy oil sample is still effectively a solid at low temperature (0 °C), but for not extremely heavy oil, at seismic frequencies, by +20 °C, the shear modulus of heavy oil is negligible and heavy oil acts still like liquid, especially after cold production when foamy oil is created due to the dissolved gas from heavy oil, and the mobility of reservoir fluids is improved much. In this case, Gassmann's equation can still help us understand the response of heavy oil reservoir to seismic survey for pre- and post- cold production.

V_p/V_s ratio is a function of both fluid bulk modulus and porosity. For unconsolidated sands with high porosity, fluids in the pore have a significant influence on final V_p/V_s ratio. Due to the dramatic reduction of fluids bulk modulus after heavy oil cold production, V_p/V_s ratio will have a detectable reduction, even though the increasing porosity from wormholes has an opposite effect and will increase V_p/V_s ratio a little bit. Meanwhile, for unconsolidated sands, lower pore pressure and increasing differential pressure will decrease the final V_p/V_s ratio too.

Interpreting multicomponent seismic data to get the V_p/V_s ratio map from traveltimes measurements on vertical and radial component data is straightforward. But in practice, it is often difficult to resolve reflections from the top and bottom of the target layer, especially for the PS seismic data. Usually, we will have to select the reference horizons from above and below our target formation. Error analysis and practical mapping tells us that the calculated V_p/V_s ratio will not be overly sensitive to the choice of picking surrounding formations and is a robust method for us to monitor the reduction of V_p/V_s ratio due to heavy oil cold production.

The frequency spectra of PP and PS seismic volumes in the depth of our target formation are often quite different. Although the picking is relatively insensitive to spectral differences between components, bandpass filtering can provide some improvement to the quality of final V_p/V_s ratio map, by enhancing the similarity between PP and PS seismic volumes.

The difference of Poisson's ratio between pre- and post-production will create different AVO responses. The calculated result from fluid substitution reveals that there about 10% reduction of P-wave velocity, about 30% reduction of saturated bulk modulus and about 20% reduction of Poisson's ratio due to heavy oil cold production. Further calculation displays that there is about 0.2 reduction of V_p/V_s ratio after heavy oil cold production. Meanwhile, there is no detectable difference between pre-production and wet case. It means that we cannot use V_p/V_s ratio and AVO analysis to originally find heavy oil field.

Synthetic seismograms from the results of fluid substitution reveal that all the AVO responses for pre- and post-production and wet case belong to Class IV, which is given by Castagna et al. (1998). The AVO response for post-production is separated from the other two cases. Although using the product of intercept and gradient is difficult to discriminate Class IV AVO responses, the fluid factor is useful to interpret Class IV AVO response. Because V_p/V_s ratio varies with time, calibrated $g(t)$ will give a better result of fluid factor for the target zone.

For the in-situ well, four methods to do fluid substitution are performed, one of them using available S-wave sonic log data, others not using available S-wave sonic log

data. Greenberg-Castagna's calculation gives the closest calculated S-wave log data to the calculated S-wave log data with using available original S-wave log data. Assuming Castagna's equation is correct for the wet case gives a relatively small S-wave velocity, while assuming dry rock Poisson's ratio gives a relatively high S-wave velocity. But overall, all of the methods give the similar AVO responses from the top of the target zone, which are Class IV AVO responses, and the AVO responses for post-production are separated from other two cases.

In order to obtain the change of V_p/V_s ratio during reservoir production, we could use time-lapse AVO on single component data. However, multicomponent time-lapse seismic surveys would allow us to find the time variation of V_p/V_s ratio more directly. These multicomponent time-lapse seismic surveys were not completed in this heavy oil field, but this would be a very interesting future project.

This study has examined the effects of cold heavy oil production on both model and real data. The study shows that cold production has an effect on both V_p and V_s velocities, which in turn affects seismic amplitudes and traveltimes. These exciting results should be examined further using time-lapse multicomponent seismology as a reservoir characterization tool.

REFERENCES

- Batzle, M., and Wang, Z., 1992, Seismic properties of pore fluid: *Geophysics*, **57**, 1396-1408.
- Batzle, M., Hofmann, R., and Han, D.H., 2006, Heavy oils – Seismic properties: *The Leading Edge*, **25**, 750-756.
- Castagna, J.P., Batzle, M.L., and Eastwood, R.L., 1985, Relationships between compressional-wave and shear-wave velocities in clastic silicate rocks: *Geophysics*, **50**, 571-581.
- Castagna, J.P., Batzle, M.L., and Kan, T.K., 1993, Rock Physics – The Link Between Rock Properties and AVO Response, in Castagna, J.P., and Backus, M.M., Eds., *Offset-dependent reflectivity – theory and practice of AVO analysis*: Soc. Expl. Geophys., 135-171.
- Castagna, J.P., and Smith, S.W., 1994, Comparison of AVO indicators: A modeling study: *Geophysics*, **59**, 1849-1855.
- Castagna, J.P., Swan, H.W., and Foster, D.J., 1998, Framework for AVO gradient and intercept interpretation: *Geophysics*, **63**, 948-956.
- Chen, S., Lines, L., and Daley, P., 2004, Foamy oil and wormhole footprints in heavy oil cold production reservoirs: *CSEG Recorder*, Vol. **29**, No. 10, 49-51.
- Chen, S., 2004, Time-lapse Seismology to Determine Foamy Oil and Wormhole Footprints in Heavy Oil Cold Production Reservoir: M.Sc Thesis, University of Calgary.
- Domenico, S.N., 1974, Effect of water saturation on seismic reflectivity of sand reservoirs encased in shale: *Geophysics*, **39**, 759-769.
- Domenico, S.N., 1976, Effect of brine-gas mixture on velocity in an unconsolidated sand reservoir: *Geophysics*, **41**, 882-894.
- Domenico, S.N., 1977, Elastic properties of unconsolidated porous sand reservoirs: *Geophysics*, **42**, 1339-1368.

- Fatti, J.L., Smith, G.C., Vail, P.J., Strauss, P.J., and Levitt, P.R., 1994, Detection of gas in sandstone reservoirs using AVO analysis: A 3-D seismic case history using the Geostack technique: *Geophysics*, **59**, 1362-1376.
- Gal, D., Dvorkin, J., and Nur, A., 1998, A physical model for porosity reduction in sandstones: *Geophysics*, **63**, 454-459.
- Gassmann, F., 1951, Über die elastizität poroser medien: *Vierteljahrsschrift der Naturforschenden Gesellschaft in Zurich*, **96**, 1-23.
- Greenberg, M.L., and Castagna, J.P., 1992, Shear-wave velocity estimation in porous rocks: Theoretical formulation, preliminary verification and applications: *Geophys. Prosp.*, **40**, 195-210.
- Gregory, A.R., 1976, Fluid saturation effects on dynamic elastic properties of sedimentary rocks: *Geophysics*, **41**, 895-921.
- Gregory, A.R., 1977, Aspects of rock physics from laboratory and log data that are important to seismic interpretation – in exploration AAPG memoir **26**, 15-46.
- Hampson, D., and Russell, B., 2003, Manual of Hampson-Russell software.
- Han, D.H., and Batzle, M.L., 2004, Gassmann's equation and fluid-saturation effects on seismic velocities: *Geophysics*, **69**, 398-405.
- Hilterman, F.J., 2001, Seismic Amplitude Interpretation: SEG and EAGE – 2001 Distinguished Instructor Short Course.
- Hornby, B.E., and Murphy, W.F., 1987, V_p/V_s in unconsolidated oil sands: Shear from Stoneley: *Geophysics*, **52**, 502-513.
- Huffman, A.R., and Castagna, J.P., 2001, The petrophysical basis for shallow-water flow prediction using multicomponent seismic data: *The Leading Edge*, **20**, 1030-1036.
- Lines, L.R., Chen, S., Daley, P.F., and Embleton, J., 2003, Seismic pursuit of wormholes: *The Leading Edge*, **22**, 459-461.

- Lines, L.R., Zou, Y., Zhang, D.A., Hall, K., Embleton, J., Palmiere, B., Reine, C., Bessette, P., Cary, P., and Secord, D., 2005, V_p/V_s characterization of heavy-oil reservoir: The Leading Edge, **24**, 1134-1136.
- Mageau, K.R., Leckie, D., and Maguire, R., 2001, The Bakken Formation of West-Central Saskatchewan and East-Central Alberta: A depositional History, Stratigraphy and Facies Distribution of Bakken Shelf Sand Ridges Using the Cactus Lake Field as a Working Model: 2001 CSPG Annual Meeting.
- Maini, B.B., 2004, Foamy oil flow in cold production of heavy oil: Distinguished lecture, Petroleum Society of CIM., April.
- Mavko, G., and Mukerji, T., 1995, Seismic pore space compressibility and Gassmann's relation: Geophysics, **60**, 1743-1749.
- Mavko, G., Chan, C., and Mukerji, T., 1995b, Fluid substitution: Estimating changes in V_p without knowing V_s : Geophysics, **60**, 1750-1755.
- Mavko, G., and Mukerji, T., 1998a, Bounds on low-frequency seismic velocities in partially saturated rocks: Geophysics, **63**, 918-924.
- Mavko, G., and Mukerji, T., 1998b, Comparison of the Kiref and critical porosity models for prediction of porosity and V_p/V_s : Geophysics, **63**, 925-927.
- Mayo, L., 1996, Seismic monitoring of foamy heavy oil, Lloydminster, Western Canada: 1996 SEG Expanded Abstracts **15**, 2091-2094.
- Metwally, M., and Solanki, S.C., 1995, Heavy oil reservoir mechanisms, Linbergh and Frog Lake Fields, Alberta, Part 1: Field observations and reservoir simulation: 46th annual technical meeting of the Petroleum Society of CIM, Banff, Alberta.
- Murphy, W., Reischer, A., and Hsu, K., 1993, Modulus decomposition of compressional and shear velocities in sand bodies: Geophysics, **58**, 227-239.
- Nur, A., Mavko, G., Dvorkin, J., and Galmudi, D., 1998, Critical porosity: A key to relating physical properties to porosity in rocks: The Leading Edge, **17**, 357-362.
- Ostrander, W.J., 1984, Plane-wave reflection coefficients for gas sands at nonnormal angles of incidence: Geophysics, **49**, 1637-1648.

- Prasad, M., 2002, Acoustic measurements in unconsolidated sands at low effective pressure and overpressure detection: *Geophysics*, **67**, 405-412.
- Ross, C.P., Effective AVO crossplot modeling: A tutorial: *Geophysics*, **65**, 700-711.
- Russell, B.H., Hedlin, K., Hilterman, F.J., and Lines, L.R., 2003, Fluid-property discrimination with AVO: A Biot-Gassmann perspective: *Geophysics*, **68**, 29-39.
- Rutherford, S. R., and Williams, R.H., 1989, Amplitude-versus-offset in gas sands: *Geophysics*, **54**, 680-688.
- Sawatzky, R.P., Lillico, D.A., London, M.J., Tremblay, B.R., and Coates, R.M., 2002, Tracking cold production footprints: 2002 CIPC conference, Calgary, Alberta.
- Shuey, R.T., 1985, A simplification of the Zoeppritz equations: *Geophysics*, **50**, 609-614.
- Smith, G.C., and Gidlow, P.M., 1987, Weighted stacking for rock property estimation and detection of gas: *Geophys. Prosp.*, **35**, 993-1014.
- Smith, G.C., and Sutherland, R.A., 1996, The fluid factor as an AVO indicator: *Geophysics*, **61**, 1425-1428.
- Smith, T.M., Sondergeld, C.H., and Rai, C.S., 2003, Gassmann fluid substitutions: A tutorial: *Geophysics*, **68**, 430-440.
- Tatham, R.H., and Stoffa, P.L., 1976, V_P/V_S -A potential hydrocarbon indicator: *Geophysics*, **41**, 837-849.
- Tatham, R.H., 1982, V_P/V_S and lithology: *Geophysics*, **47**, 336-344.
- Theune, U., Schmitt, D.R., and Rokosh, D., 2003, Feasibility study of time-lapse seismic monitoring for heavy oil reservoir development – The rock-physics basis: 2003 SEG Expanded Abstracts **22**, 1418-1421.
- Tremblay, B., Sedgwick, G., and Vu, D., 1999a, A review of cold production in heavy oil reservoirs: EAGE-10th European Symposium on Improved Oil Recovery, Brighton, UK.
- Tremblay, B., Sedgwick, G., and Vu, D., 1999b, CT Imaging of Wormhole Growth under Solution-Gas Drive: *SPE Reservoir Eval. & Eng.*, **2** (1), 37-45.

- Tremblay, B., and Oldakowski, K., 2002, Wormholes growth and interaction in a large sand pack: *Journal of Petroleum Science and Engineering*, **34**, 13-34.
- Verm, R., and Hilterman, F., 1995, Lithology color-coded seismic sections: The calibration of AVO crossplotting to rock properties: *The Leading Edge*, **14**, 847-853.
- Wang, Z., 2001, Fundamentals of seismic rock physics: *Geophysics*, **66**, 398-412.
- Watson, I.A., Lines, L.R., and Brittle, K.F., 2002, Heavy-oil reservoir characterization using elastic wave properties: *The Leading Edge*, **21**, 736-739.
- Yuan, J., Tremblay, B., and Babchin, A., 1999, A wormhole network model of cold production in heavy oil: SPE 54097.
- Zhang, D.A., and Lines, L.R., 2006, The robustness of V_P/V_S mapping: *The Leading Edge*, **25**, 758-763.
- Zimmer., M., Prasad, M., and Mavko, G., 2002, Pressure and porosity influences on V_P-V_S ratio in unconsolidated sands: *The Leading Edge*, **21**, 178-183.
- Zou, Y., Lines, L.R., Hall, K., and Embleton, J., 2004, Time-lapse seismic analysis of a heavy oil cold production field, Lloydminster, Western Canada: 2004 SEG Expanded Abstracts **23**, 1555-1558.